Optical Sources, Fibers and Photonic Subsystems

A. H. Johnston
Jet Propulsion Laboratory
California Institute of Technology

Optical Sources, Fibers and Photonic Subsystems

A. H. Johnston
Jet Propulsion Laboratory
California Institute of Technology

I. Introduction and Background

This section of the Short Course discusses radiation effects in photonic components, along with some examples of the radiation response of photonic subsystems. It begins with a review of some optical principles that are important in the discussions that follow.

A. Some Basic Principles of Optics

Wavelength and Energy

Light can behave either as a wave (classical optics) or particle. The energy of the photon associated with light of wavelength λ is given by the relationship below:

$$E = h c / \lambda \tag{1}$$

where E is the photon energy, h is Planck's constant (6.62×10^{-27} erg-s), c is the velocity of light, and λ is the wavelength. A practical way to apply this is to remember the simplified relationship for common units

$$\boxed{E = 1.24 / \lambda} \tag{2}$$

where E is in electron volts, and the wavelength λ is in μm.

Absorption

Absorption in optical materials is described by Beer's law,

$$I = I_o e^{-\alpha x} \tag{3}$$

where I is the light intensity after the light has traveled a distance x in the material, I_o is the light intensity at the surface (ignoring surface reflection), and α is the absorption coefficient in

---

The research in this chapter was carried out at the Jet Propulsion Laboratory, California Institute of Technology, under contract with the National Aeronautics and Space Administration (NASA).

reciprocal cm. A penetration depth can be defined by $1/\alpha$, corresponding to a drop in intensity by the factor 1/e. Equation 3 applies to a wide range of materials, including amorphous materials such as glass and many semiconductors. It will be used later in discussions of optical detectors, laser diodes, and optical fibers.

Absorption in amorphous materials decreases with increasing wavelength because of Rayleigh scattering. The functional dependence is quite strong, obeying a λ^{-4} power. Fig. 1 show how absorption in silica (silicon dioxide) depends on wavelength. This example is for typical core materials in optical fibers, so the units – dB/km – relate to long-distance optical fiber applications. The Rayleigh scattering region is apparent at shorter wavelengths. The presence of small amounts of water in the silica increase the absorption in the regions shown in the figure. The three "windows" at 850, 1300 and 1500 nm correspond to regions that are of practical interest for fiber communication because fiber losses are acceptably low at those wavelengths. Many optoelectronic components have been developed for those specific wavelengths because of the strong interest and demand for optical communication applications.

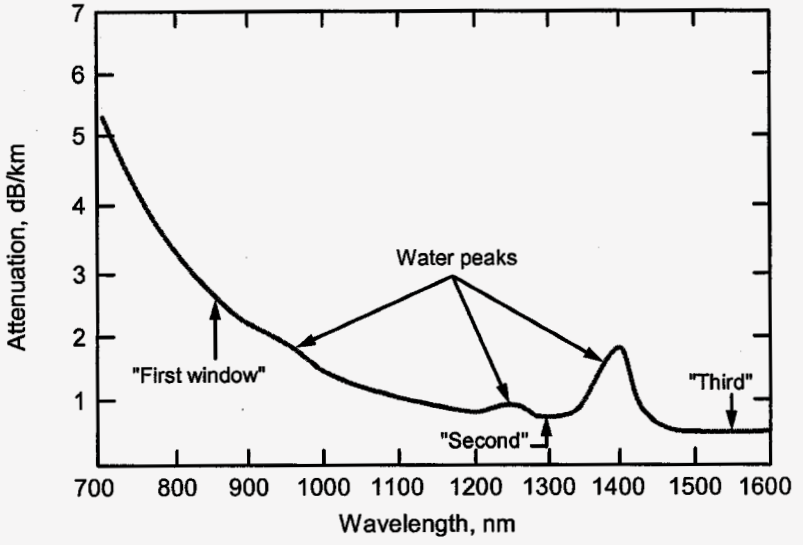

Fig. 1. Absorption dependence on wavelength for highly purified amorphous silicon dioxide with small amounts of water present.

Absorption in crystals depends on the bandgap and the nature of the material, decreasing near the band edge when the photon energy falls below the energy required to raise carriers from the valence to the conduction band. Fig. 2 shows how the absorption coefficient of three different semiconductors depends on wavelength. The bandgaps of the three materials are 1.08 μm (silicon), 0.86 μm (GaAs) and 1.65 μm (InGaAs). Because silicon has an indirect bandgap (*direct and indirect semiconductors are discussed in more detail in the next subsection*), the absorption coefficient of silicon changes gradually with increasing wavelength, compared to the more abrupt wavelength dependence of the other two materials that have direct bandgaps. Although not shown in the figure, germanium also has an indirect bandgap, with an absorption edge at about 1.8 μm. Germanium detectors are useful for longer wavelengths, but detectors with III-V semiconductors (such as InGaAs) have largely supplanted germanium in fiber optic receiver applications because they have lower dark current as well as a relatively constant absorption coefficient over a wide range of wavelengths.

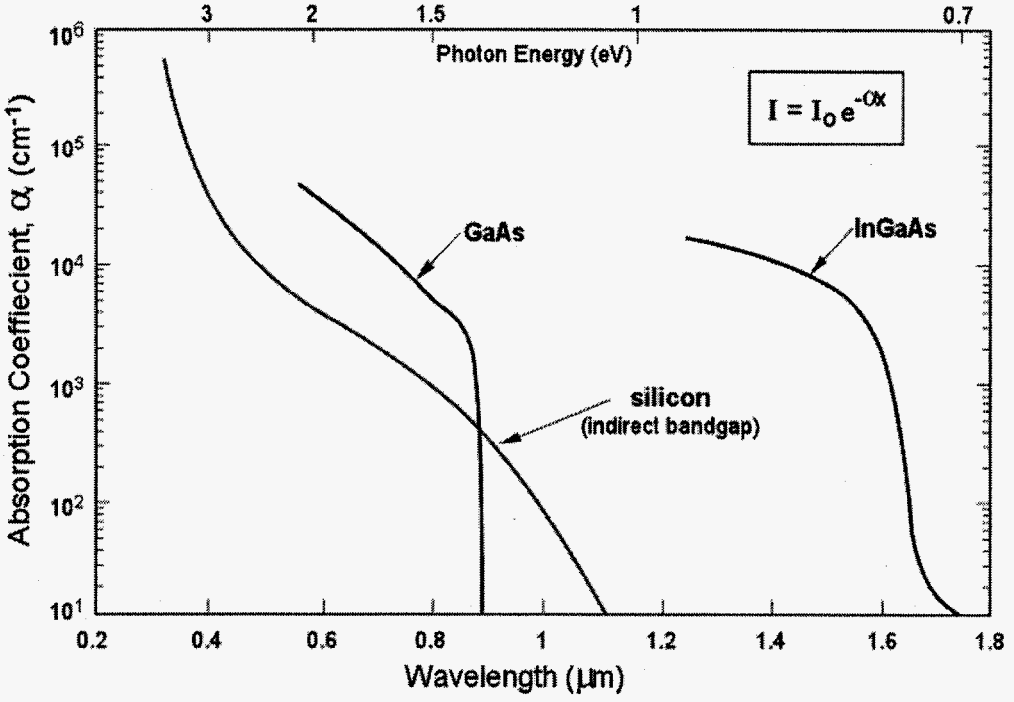

Fig. 2. Dependence of the absorption coefficient on wavelength for three different semiconductor materials.

Reflection and Refraction

Index of Refraction

Light travels more slowly in an optical medium compared to its velocity free space, by a factor n, where n is the index of refraction. The index of refraction is approximately equal to the square root of the dielectric constant of the material. The table below shows the index of refraction for several materials of interest. The index of refraction depends on wavelength, decreasing at shorter wavelengths. The values in Table 1 are approximate. For AlGaAs (a solid solution) the index of refraction depends on the mole fraction of aluminum, decreasing with increasing Al concentration.

Table 1
Index of Refraction for Several Materials of Interest

Material	**Index of Refraction**
amorphous silica (glass)	1.5
silicon	3.45
GaAs	3.62
$Al_{0.3}Ga_{0.7}As$	3.39
InP	3.54

Snell's Law

Refraction of light at an interface between two different materials obeys Snell's law,

$$n_1 \sin(\theta_1) = n_2 \sin(\theta_2) \quad (4)$$

where n_1 and n_2 are the refractive indices of the two materials, and θ_1 and θ_2 are the angle of incidence and the angle of refraction, as shown in the simple diagram of Fig. 3, below. In this case the ray approaches the interface from the medium with lower refractive index, and Eq. 4 is valid for all angles because the angle of refraction is always less than the angle of incidence.

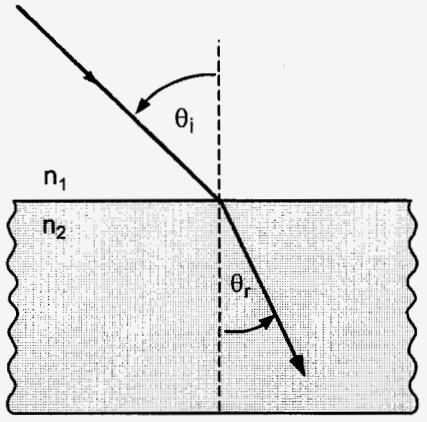

Fig. 3. Refraction of a light wave at the interface between two materials with indices of refraction n_1 and n_2.

For the case where the light ray approaches the interface from the region with higher refractive index, the situation is more complex because the angle of refraction is greater than the angle of incidence. Equation 4 has no real solution when the angle of refraction exceeds 90 °. For that angle (called the critical angle or Brewster angle) and all angles exceeding the Brewster angle, light is no longer transmitted from the first medium to the second, but is reflected. This is called total internal reflection. It is fundamental to an understanding of optical fibers, discussed in Section III, as well as in light extraction from LEDs.

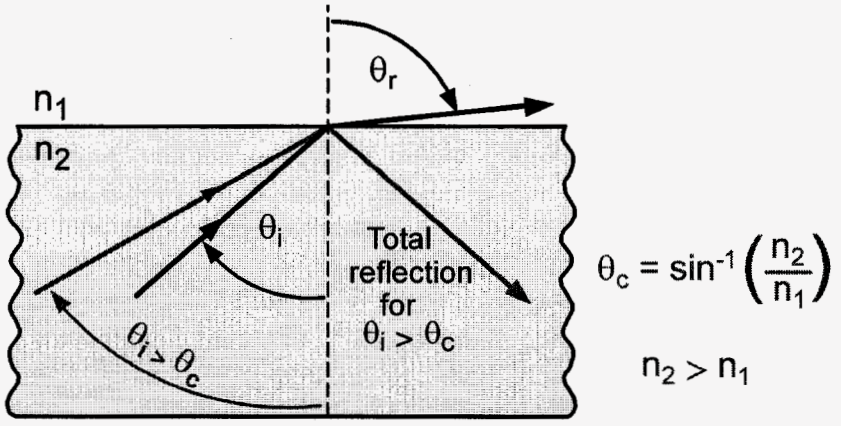

Fig. 4. Refraction when the light approaches the interface from the region with higher index of refraction, showing the critical or Brewster angle.

Even though the simplified diagram of Fig. 4 shows complete reflection at the interface when the angle of incidence exceeds the Brewster angle, the incident wave actually extends slightly beyond the interface region. This *evanescent wave* extends into the surface of the dielectric. The penetration distance of the evanescent wave into the material with lower dielectric constant is $\approx 0.1\ \lambda$. This will be important when we consider optical confinement in very thin layers of materials used in laser diodes, where the dimensions of different materials are much less than one wavelength.

Antireflection Coatings

It is possible to increase light transmission at an interface by depositing a thin film with a lower refractive index. The film properties are chosen so that the effective film thickness is equal to ¼ of the wavelength, resulting in constructive interference that eliminates the reflected component at the uncoated interface. The condition for normal incidence is given by

$$d = \frac{\lambda}{4n} \qquad (5)$$

where d is the thickness of the coating, λ is the wavelength, and n is the refractive index of the coating material. Most optical components incorporate some form of antireflective film to increase light transmission because of the large Fresnel reflection losses that occur for materials with large refractive index. In practice, multiple films are used for more effective antireflection properties when the light strikes the interface at more oblique angles.

B. Some Important Semiconductor Properties

Bandgap

The bandgap of a semiconductor corresponds to the energy difference between bound electrons in the valence band and mobile electrons in the conduction band. Recall from the band theory of solids that the motion of carriers in a crystal is described by a wave function, $\psi_k = u(r)e^{ik\cdot r}$, where u(r) is a modulating function, and k and r are momentum (wavenumber) and distance variables within the lattice. The energy E of the carriers is expressed by the equation

$$E = \hbar^2k^2/2m \qquad (6)$$

where $\hbar$ is Plancks' constant divided by 2π, k is the wave number, and m is the effective mass of the carriers within the semiconductor lattice. This is illustrated in the simple diagram of Fig. 5a for an ideal material with quadratic dependence of the wavenumber k on energy. Real materials are much more complex, with energy bands that depend on the crystal orientation.

Direct and indirect semiconductors

The selection rules of quantum mechanics apply to transitions between the valence and electron bands of a solid. For the case where the maximum energy in the valence band corresponds to the same value of k as the lowest energy in the conduction band, it is possible for a carrier to move between the two regions with a direct transition, corresponding to absorption or emission of a photon. Semiconductors with this alignment of the minimum and maximum of the two band regions are *direct bandgap* semiconductors, and they are the class of semiconductors

that are the most important for optoelectronic emitters because they can absorb or emit photons with high efficiency.

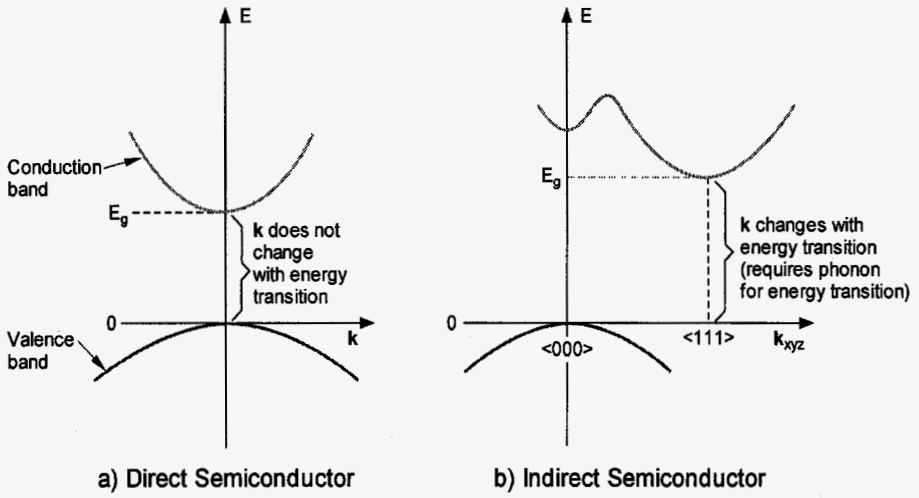

Fig. 5. Simplified diagram showing the alignment of valence and conduction bands in direct and indirect semiconductors.

For many semiconductors (particularly silicon), the minimum in the conduction band does not correspond to the same wavenumber as the maximum in the valence band. In this case, transitions between the two bands require absorption (or emission) of a phonon in addition to a phonon in order to change the wavenumber, k. Consequently, photon absorption and emission have relatively low probabilities, and are usually not the dominant process in these classes of materials. Although indirect semiconductors are useful as detectors, they are not capable of efficient light emission because of the requirement for phonons as part of the transition process. Interband recombination is proportional to the product of the n- and p-carrier densities,

$$R = B n p \tag{7}$$

Values of the proportionality constant, B, are shown in Table 2 for several different semiconductors. For semiconductors with direct bandgap the band-to-band recombination probability is 5 to 6 order of magnitude greater than for semiconductors with indirect bandgap.

Table 2. Rate Constant for Band-to-Band Recombination for Various Semiconductors

Semiconductor	Bandgap	Rate Constant, B (cm^3/s)
silicon	indirect	1.79×10^{-27}
germanium	indirect	5.25×10^{-26}
GaP	indirect	5.37×10^{-26}
GaAs	direct	7.21×10^{-22}
InP	direct	1.26×10^{-21}

Band Tailing

Real semiconductors have many possible states, distributed with slightly different energies along the conduction and valence band boundaries. Transitions are possible between different states, leading to a distribution of photon energies for optical transitions.

The bandgap energy also depends on doping concentration. For doping levels > 10^{17} cm^{-3} the presence of a large number of easily ionized dopant atoms distorts the band structure, causing states with high occupation to spill into the normally forbidden region that exists when the semiconductor is lightly doped. This effect is called band tailing [Pank76], as shown in Fig. 6. It is important for laser diodes as well as for light emitting diodes with compensated doping. There are several important consequences. First, the photon energy is reduced somewhat compared to lightly doped material because electrons in the conduction band can make a transition to the highly populated "tail" region in the valence band, which extends into the forbidden region of the bandgap. Second, the wavelength is slightly longer (corresponding to lower energy transitions), reducing absorption losses in the material. That characteristic is particularly important for compensated semiconductors.

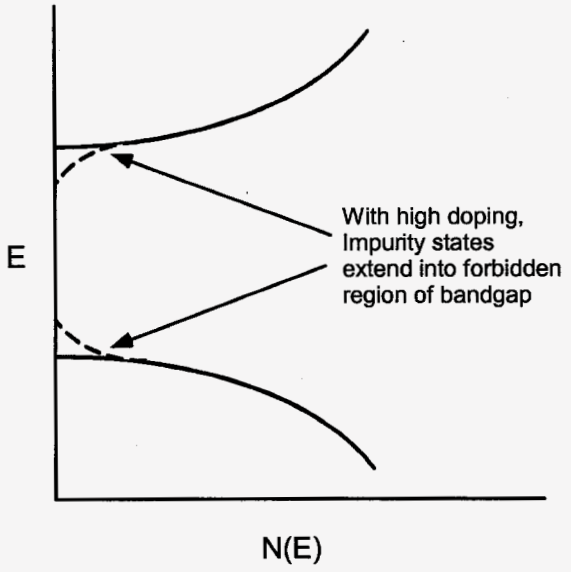

Fig. 6. Distortion of band edges at high doping levels. The extension of impurity bands into the forbidden region of the bandgap allows transitions between lightly populated states in the valence band and the heavily populated region in the valence band, reducing the energy of photons that are emitted during the transition.

Absorption and Recombination Mechanisms

For direct bandgap semiconductors, there are several processes that involve absorption or emission of photons:

- Spontaneous emission of a photon, moving an electron from the conduction band to the valence band
- Absorption of a photon, elevating an electron to the conduction band and simultaneously creating a hole in the valence band, and
- Stimulated emission, where the presence of photons within the semiconductor "triggers" emission of additional photons. *An important property of stimulated emission is that photons produced by this process have the same direction and frequency of the initiating photon.*

Those three processes are illustrated in Fig. 7. The first process, spontaneous emission, is responsible for light emission in light-emitting diodes. The last process, stimulated emission, is the mechanism involved in semiconductor lasers. The probability of stimulated emission is very low under low injection condition, but it becomes the dominant recombination process when the density of carriers is sufficiently high. The fact that the photons that are emitted by that process have the same direction and frequency as the initiating photon is critically important for semiconductor laser operation.

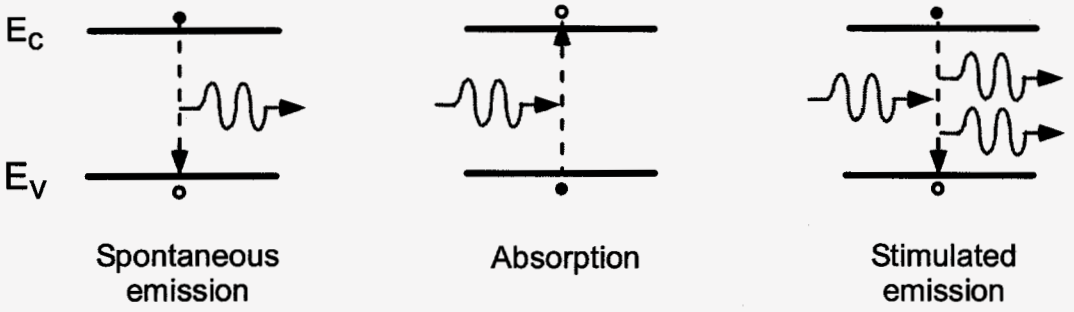

Fig. 7. Absorption and emission processes that are accompanied by photon emission or absorption.

It is also possible for carriers to recombine through non-radiative processes (loss mechanisms). Two important processes are illustrated in Fig. 8. Non-radiative recombination through traps is shown at the left. We will see later that one of the important effects of radiation is to increase non-radiative recombination losses through deep level recombination centers, which are introduced by displacement damage.

Another loss mechanism is Auger recombination [Vurg97, Fehs02], shown at the right. In this example, two electrons interact, releasing energy to one of the electrons involved in the initial interaction. The electron with the higher energy is released from the lattice, eventually releasing the excess energy in the form of heat. The other electron loses energy in the initial interaction, falling to the valence band *without releasing a photon* (the lost energy was gained by the "hot" electron in the original interaction). Auger recombination can be considered the inverse of the impact ionization process. High carrier densities are required; the probability for Auger recombination depends on the third power of the carrier density, as well as on basic material properties.

A third loss mechanism, surface recombination, must also be considered. However, surface recombination from radiation damage is less significant for most III-V semiconductors compared to silicon, partly because it is not possible to form insulators with the same high quality as silicon dioxide in III-V semiconductors.

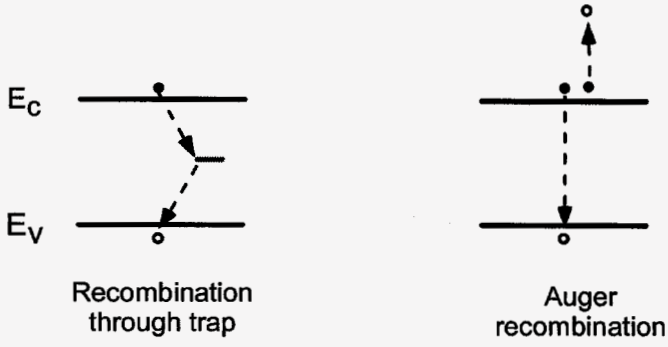

Fig. 8. Two important non-radiative recombination mechanisms for direct-bandgap semiconductors.

Quantum Efficiency

The term quantum efficiency is often used to describe the effectiveness of radiative processes. The internal quantum efficiency, which ignores loss mechanisms in light extraction, is related to the lifetime of non-radiative and radiative processes by the equation

$$\text{Q.E.} = \left(1 + \frac{\tau_r}{\tau_{nr}}\right)^{-1} \qquad (8)$$

where Q.E. is the internal quantum efficiency, τ_r is the radiative recombination lifetime, and τ_{nr} is the non-radiative lifetime.

Conventional p-n Junctions (Homojunctions)

Highly purified semiconductors have very low conductivity at room temperature. Their properties are highly sensitive to certain types of impurities that are deliberately added as dopants during fabrication. The dopant atoms replace silicon atoms in the lattice structure. For a material such as silicon with a valence of 4, dopant atoms with a valence of five (As or P) will act as *donors*, giving up their extra electrons in the silicon lattice to the conduction band. Materials with a valence of three act as *acceptors*, taking an electron from the (filled) valence band, producing a hole. The dopant impurity atoms have energy levels near the edge of the bandgap, and are readily ionized (except at very low temperature). The effect of the impurity atoms is to shift the equilibrium potential within the semiconductor towards the conduction band (donors) or the valence band (acceptors).

A p-n junction is formed by placing p- and n-type semiconductors in close proximity (in practice, this is usually done by deliberately adding impurities to modify the doping). The difference in equilibrium potential between the two doped regions creates a retarding potential, as shown in the diagram of Fig. 9. The potential changes near the boundary between the n- and p-regions, creating narrow regions of "uncovered" charge from the dopant atoms. Donor atoms are left with a positive charge, having given up one electron, while acceptor atoms have a negative charge. This boundary extends over regions of approximately 1 to 100 μm, depending on the doping density (it is larger for lightly doped material). The width of the boundary also depends on external bias conditions. Although the example shown is for silicon, the same principle applies to GaAs or other III-V materials. The important point is that unless the doping level is extremely high, the transition region will extend over distances of several microns or more. Such dimensions correspond to more than an optical wavelength for the wavelengths that we are considering in this section of the short course. This establishes the lower dimensional limit for semiconductors fabricated with homojunctions.

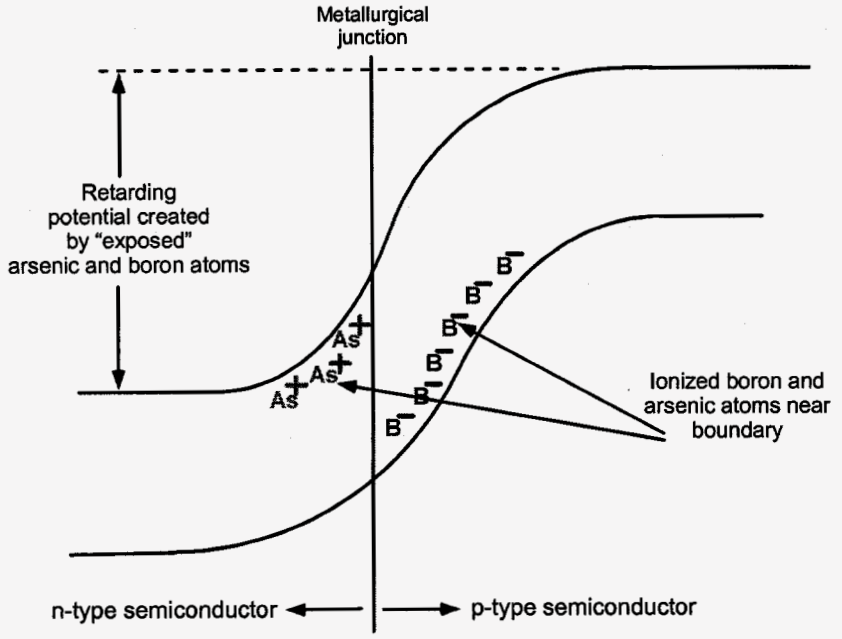

Fig. 9. Diagram showing the retarding potential created when two regions of the same semiconductor type (silicon in this example) with different doping levels are placed in close proximity.

Heterostructures

It is also possible to create a p-n junction by placing two different ***types*** of semiconductors together, forming a heterojunction. Note the distinction from homojunctions where the doping levels differ but the same basic type of semiconductor is present on each side of the junction. For a heterojunction the barrier for holes and electrons is affected by the difference in bandgap between the two semiconductor types as well as the concentration of dopant atoms. The bandgap discontinuity adds to the potential barrier in the junction, increasing carrier injection efficiency [Pani76]. In order to form a heterostructure that is useful for optoelectronic applications, the lattice spacing of the two semiconductor materials must be closely matched in order to maintain the structure of the lattice. Otherwise defects in the crystalline structure will occur that reduce the mobility and affect the reliability of the device.

Figure 10 shows an example of the potential discontinuity formed by a GaAs/AlGaAs heterojunction with no external potential applied [Chua95]. The bandgaps of the two materials differ by 0.40 eV. Note that the band offset is greater in the conduction band compared to the valence band. The band offset ratio is typically about 2:1, and is an important heterostructure property. For the example in Fig. 10 the lateral dimension required by the heterostructure for equilibrium is about 0.1 μm, about a factor of 30 less than the lateral dimension of a GaAs homojunction with comparable doping levels.

This example shows a p-N heterostructure (the upper case symbol is used to designate the material with higher gandgap). It is analogous to a conventional p-n junction, except for the increased potential difference that is introduced by the bandgap discontinuity. Note that the energy difference is about twice as large in the valence band compared to the conduction band for this heterostructure. If an external potential is applied it will function in the same way as a conventional p-n junction, but carrier injection will be aided by the bandgap discontinuity, increasing injection efficiency.

It is also possible to form p-P or n-N heterostructures (*isoheterostructures*) because of the energy difference between the two materials. Such heterostructures are frequently used in the

multiple layers used to form modern optoelectronic components. The bandgap discontinuity can be sufficient to confine carriers even though no junction exists.

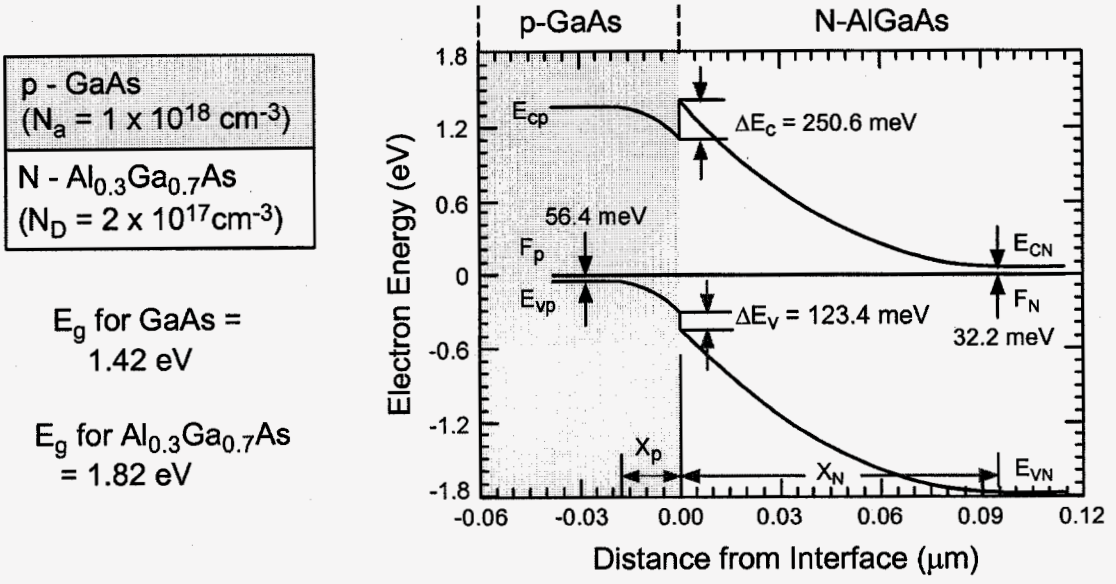

Figure 10. Electron energy vs. distance from the interface for a step junction formed by GaAs and AlGaAs. The bandgap of the two materials differs by 0.4eV.

Ternary and Quaternary Materials for Optical Heterostructures

Requirements

Several III-V elements can be combined in various proportions to form solid solutions, either as ternary or quaternary materials. This is called bandgap engineering because it allows the bandgap to be adjusted over a wide range by suitable selection of materials. This allows devices to be tailored over a wide range of wavelengths. The important requirements for the use of III-V solid solutions in heterostructures are as follows:

- The lattice spacing must be closely matched to that of the underlying host material in order to maintain orderly crystal structure and avoid introducing defects. Typically this requires a lattice spacing that is matched within approximately 0.2%.
- The solid solution must also have a direct bandgap.
- The index of refraction of the solid solution is an important property in optoelectronic devices because of the need to confine photons as well as charge carriers in the overall device structure.

For these systems it is important to distinguish between the substrate material and the material combinations used for other layers. This can be very confusing, particularly for quaternary materials. We will use parentheses and italics for the substrate material in the discussions that follow.

Ternary Systems Using AlGaAs (*GaAs*)

The most widely studied material system is aluminum gallium arsenide, used for the pioneering work in developing LEDs and laser diodes in the 1970s [Raze00]. Unlike many other material combinations, AlGaAs remains closely lattice matched to GaAs over its entire range of composition, a major advantage. Fig. 11 shows how the bandgap of solid solutions of AlGaAs

change as the mole fraction, X, of aluminum is increased. For X = 0.45, the material changes from direct to indirect bandgap, limiting the usefulness for most optoelectronic devices to mole fractions below 0.45. Nevertheless, this material system allows the bandgap to be varied over a range than provides wavelengths from approximately 630 to 870 nm.

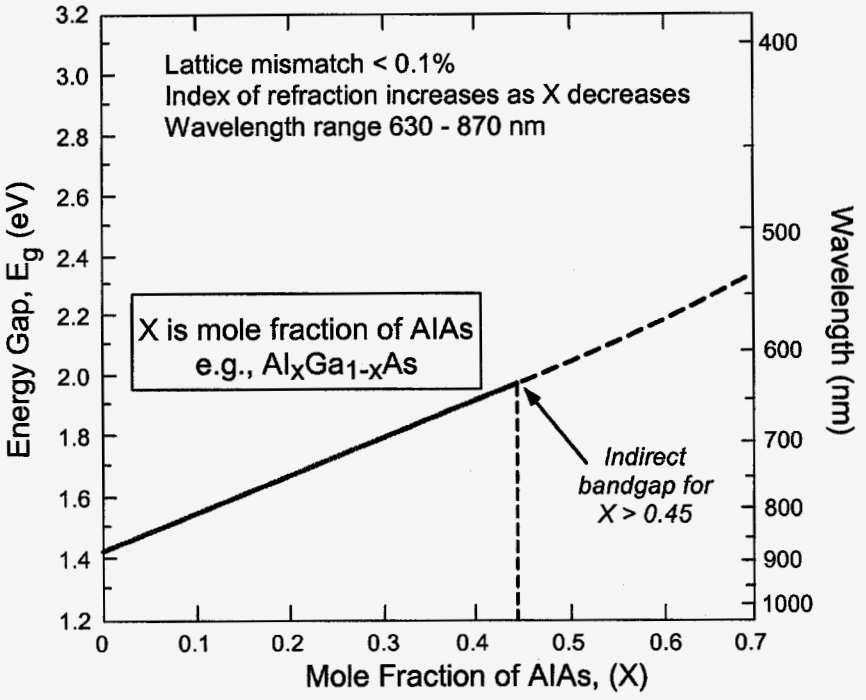

Fig. 11. Variation of the energy gap of solid solutions of AlGaAs as the mole fraction of aluminum is increased from 0 (pure GaAs) to 0.45, where the material no longer has a direct bandgap. This corresponds to a wavelength range of 630 to 870 nm.

Quaternary Systems Using InGaAsP (*InP*)

The fortuitous close lattice matching of AlGaAs is one of the reasons that initial work on heterostructures for optoelectronics concentrated on that material system. Fig. 12 shows lattice matching for AlGaAs, as well as more complex quaternary systems using various combinations of InAs, InP, and GaAs. Note the very poor lattice matching for the GaAs/InAs system.

A quaternary system based on InGaAsP provides lattice matching over an extended range of energy gaps from about 0.8 to 1.45 eV, as shown in the figure. That material system has been used to develop LEDs and lasers with wavelengths between 1100 and 1600 nm. Lattice matching considerations restrict the fractional makeup of the constituents. Quaternary compounds have many degrees of freedom. For InGaAsP, the mole fractions of In and Ga are usually interrelated [by (1-X) and X, respectively], with a similar relation between the mole fractions of P and As [(1-Y) and Y] because those combinations maintain close lattice matching.

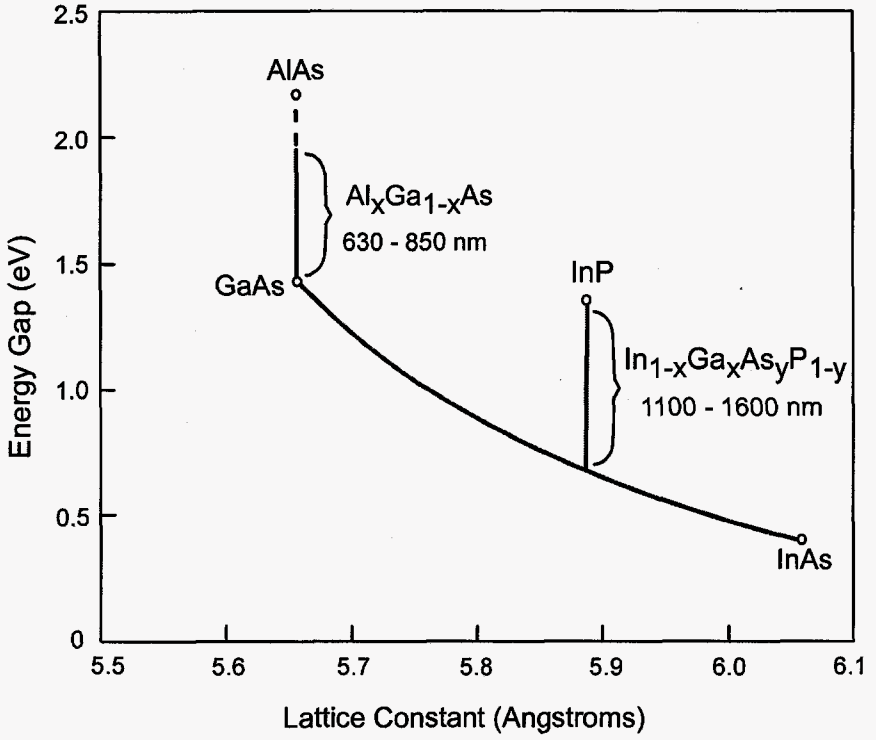

Fig. 12. Lattice constant for various material combinations used in optoelectronic devices.

Strained Lattices

Although we have stressed the importance of close lattice matching for heterojunctions, it is possible to grow regions with lattice mismatch up to 2% with low defect density provided that the thickness of the transition region between the two materials is less than about 100 angstroms. One advantage of strained lattices is that it allows new material combinations to be used, such as the use of strained InGaAs for lasers and LEDs with wavelengths between 900 and 1100 nm, where there are no suitable materials with close lattice matching.

Another advantage of strained layer technology is that it changes the hole mobility. This can be used to improve the performance of optical emitters, deliberately introducing strain into the lattice. If done properly, this can be used to reduce the threshold current density of laser diodes [Cole00]. Many advanced lasers take advantage of this property. Despite the lattice mismatch, it is possible to fabricated highly reliable devices with strained layers as long as the thickness of the strained region is sufficiently low [Selm01].

II. Optical Emitters

A. Light-Emitting Diodes

For direct bandgap semiconductors, the dominant recombination mechanism under moderate forward bias involves band-to-band emission of a photon. Light-emitting diodes use this property to generate light, with an intensity that is approximately proportional to the forward current through the p-n junction. There is a very important difference between conventional diodes and LEDs. For conventional diodes the purpose is to produce a p-n junction with low internal loss mechanisms and efficient rectification. For an LED, the purpose is to *maximize* internal losses that result in efficient photon emission, taking advantage of the high radiative loss efficiency. One way to accomplish this is to use a material with very low doping in the active

region. LEDs are analogous to p-i-n diodes, using direct bandgap materials with high probability of band-to-band recombination in the i-region [Pani76].

Fig. 13 shows the light output of an LED along with the forward current through the LED as a function of forward voltage. At low current, non-radiative recombination processes dominate, with negligible light output. When the forward voltage reaches about 1.05 V the injected current is sufficient to overcome non-radiative recombination losses, and there is an increase in the slope of the I-V characteristic (the slope approximately doubles) that is accompanied by an increase in optical power output. Above that value the optical power is approximately proportional to forward current, eventually flattening out because of internal resistance. The region between the change in slope and the saturation point defines the useful range of operating currents for an LED.

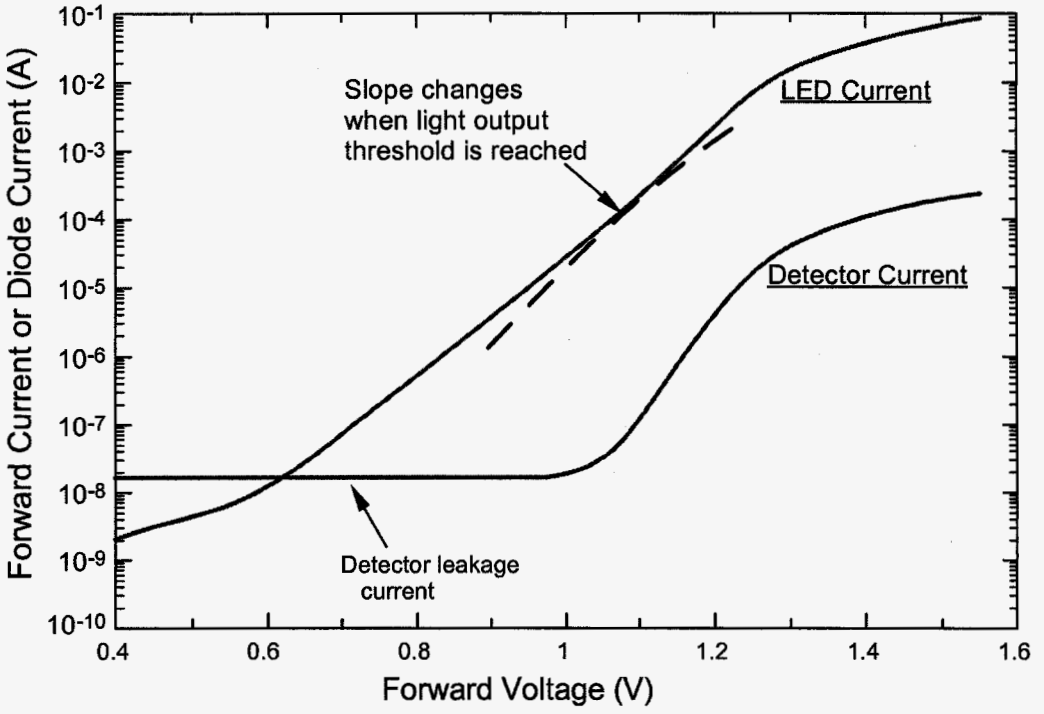

Fig. 13. Dependence of optical power and forward current on forward voltage for an LED showing the increase in slope when the forward current is sufficient to overcome non-radiative recombination losses.

Although the conversion process from current to light is very efficient, extraction of light is limited by Snell's law because of the high index of refraction of typical III-V materials, nominally 3.5. As a result, the Brewster angle is about 17 degrees (assuming an air interface), and any photons striking the interface at angles greater than 17 ° will be reflected back, as shown in the simple diagram of Fig. 14. The photons that are formed by spontaneous recombination have arbitrary directions. As a result, the extracted optical power is about 2% of the electrical power through the LED unless special designs are used. Methods of improving light extraction include the use of an integral lens, as well as special cavity designs that reduce the number of photon striking the surface at large angles [Vand97].

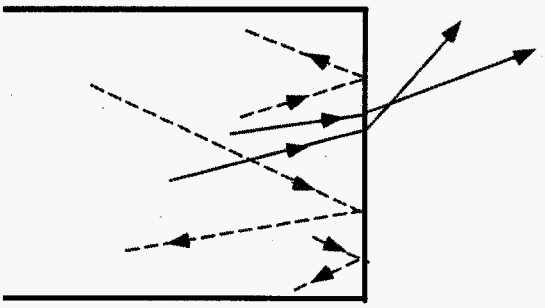

Fig. 14. Photons from an LED striking the interface between the III-V material and an interface with n =1. Spontaneous recombination produces photons with arbitrary direction, most of which strike the interface at oblique angles where they are reflected back into the bulk region and eventually recombine.

Homojunction LEDs

An older process that is still used for some types of LEDs relies on doping GaAs with an amphoteric impurity; i.e. an impurity than can function either as an acceptor or donor, depending on conditions within the semiconductor. Early LEDs used zinc as an amphoteric impurity, but since the mid-1970's silicon (as an amphoteric dopant) has been preferred because it provides higher optical efficiency compared to Zn. The growth process relies on a special property of silicon in GaAs (or AlGaAs). When a GaAs crystal is grown in a sample that is heavily doped with silicon, the silicon is a donor at high temperatures. However, it becomes an acceptor if the growth is done at lower temperature [Rupp66]. Thus, if we gradually reduce the temperature during the growth process the initial part of the GaAs will be p-type, while GaAs formed in later stages at lower temperatures will be n-type. The transition temperature is approximately 850 °C. With this technique, a junction can be formed without introducing special dopants simply by changing the temperature during the growth process.

Fig. 15 shows a diagram of an amphoterically doped AlGaAs LED. Note the relatively broad transition region between the n- and p-regions. One reason that this type of LED has high efficiency is that the silicon doping level is so high that the material is compensated. This causes the energy gap to "soften" (band-tailing), reducing non-radiative absorption within the structure. The energy of the photons is slightly below the bandgap energy because of a complex associated with acceptor states. This eliminates band-to-band absorption losses due to shallow impurity states.

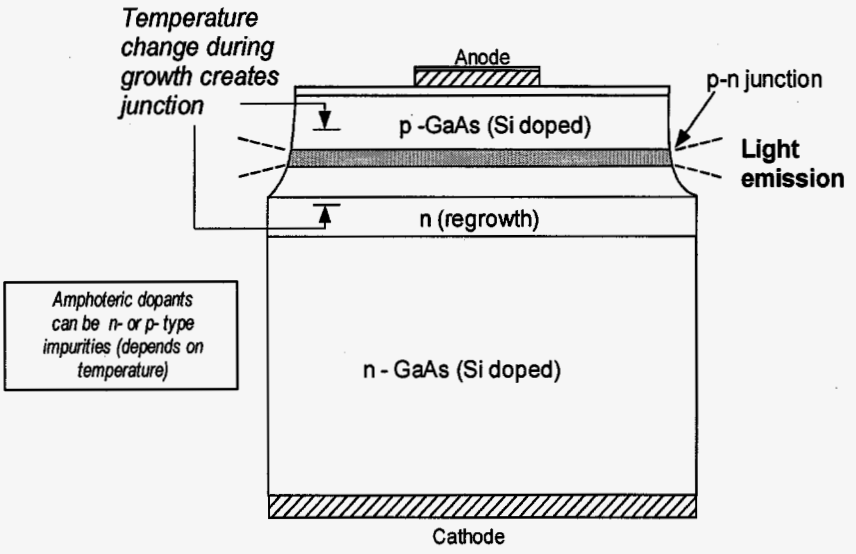

Fig. 15 Diagram of a homojunction LED produced by altering the growth temperature with an amphoteric impurity.

The transition region from p- to n-type material occurs over a relatively wide region because of the somewhat cumbersome mechanical configuration used to grow the crystal, along with the requirement to make this process slow enough to allow the growth temperature to gradually change by about 40 ° C. As a consequence, this type of LED requires a high lifetime – several microseconds or more –to function because if the lifetime is too short, the diffusion length will be reduced, and non-radiative recombination will occur before the carriers reach the other side of the extended width of the p-n junction.

Heterostructure LEDs

Heterostructure LEDs have a far more complicated structure. LEDs with single heterojunctions can be formed by growing AlGaAs on GaAs, using an additional surface diffusion to drive the active junction below the surface. This results in an LED with a much shallower structure and faster response time compared to the amphoterically LED described earlier. That structure has been used for surface-emitting LEDs, matching the circular pattern of the diffusion to the diameter of an optical fiber.

More advanced LEDs use double heterojunctions, with light emission from the edge. Figure 16 shows a structure that is typical of the LED technologies used for general purpose and telecommunication applications. The structure has several different layers with different purposes. The active layer is undoped GaAs, with a typical thickness of 0.2 to 0.3 μm. Light produced within that region is confined by the two AlGaAs guiding regions that have lower refractive index than GaAs. The p- and n-doped AlGaAs layers form heterojunctions for carrier injection.

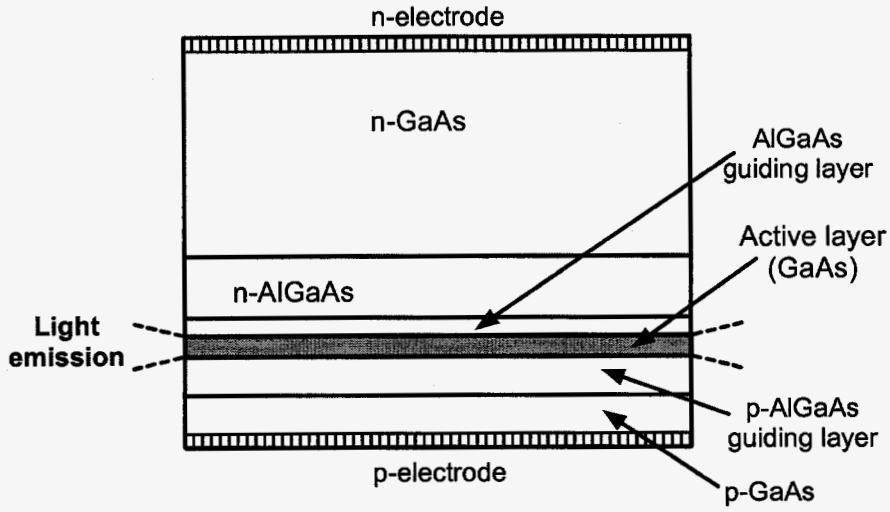

Fig. 16. Diagram of a double-heterojunction edge-emitting LED.

This type of LED can be fabricated with many different material systems, with wavelengths from 650 nm (using AlGaAs) to 1550 nm (InGaAsP). Longer wavelength LEDs intended for fiber optic applications are often designed for very fast response times, requiring thin active layers.

Many recent advances have been made in LED technology, including special designs with transparent substrate to eliminate absorption within the substrate [Vand97], and the use of special microcavity LED designs to improve overall coupling efficiency [Choi04]. Those techniques are particularly important for LEDs in the visible region, increasing light extraction efficiency. In the near infrared, there is more interest in using laser diodes because of the ease of efficient light extraction, as discussed in the next subsection, as well as the requirement for narrow exit beam patterns for fiber optic applications.

B. Laser Diodes

Laser diodes are similar in concept to light-emitting diodes, but rely on the principle of stimulated emission to provide far higher light generating efficiency than is possible with LEDs. Stimulated emission was shown earlier at the right of Fig. 6. In order for stimulated emission to occur, the carrier density within the semiconductor must be high enough so that photons traveling in the preferred direction have a high probability of creating additional photons within the guided region by spontaneous emission. In an edge-emitting laser the preferred direction is established by cleaving two surfaces to form a Fabry-Perot resonant optical cavity, coating one facet with metal. In order for the device to function as a laser, carrier injection must be high enough to provide an overall optical gain that is greater than one.

Before discussing the details of laser operation, it is useful to examine the history and evolution of semiconductor lasers. The first lasers, produced in 1962, were homojunction lasers with threshold current densities above 10^5 A/cm^2 [Pani76]. They could only operate at low temperature (77 K), and were only capable of operating for a few hours. Since that time a great deal of effort has been spent in improving laser efficiency and developing new material technologies to expand the range of available wavelengths. Fig. 17 shows how various changes and breakthroughs in device technology have reduced the threshold current [Lede00]. The first major change was the introduction of heterostructures, which reduced the threshold current by several orders of magnitude, expanded the range of wavelengths and materials, and allowed reliable operation at room temperature. Quantum-well lasers, made possible by advanced

fabrication techniques that allowed reproducible fabrication of very thin layers of III-V materials, allowed further reductions in threshold current. During the last 8 years, quantum dot lasers have been developed, reducing the threshold current density to about 20 A/cm^2.

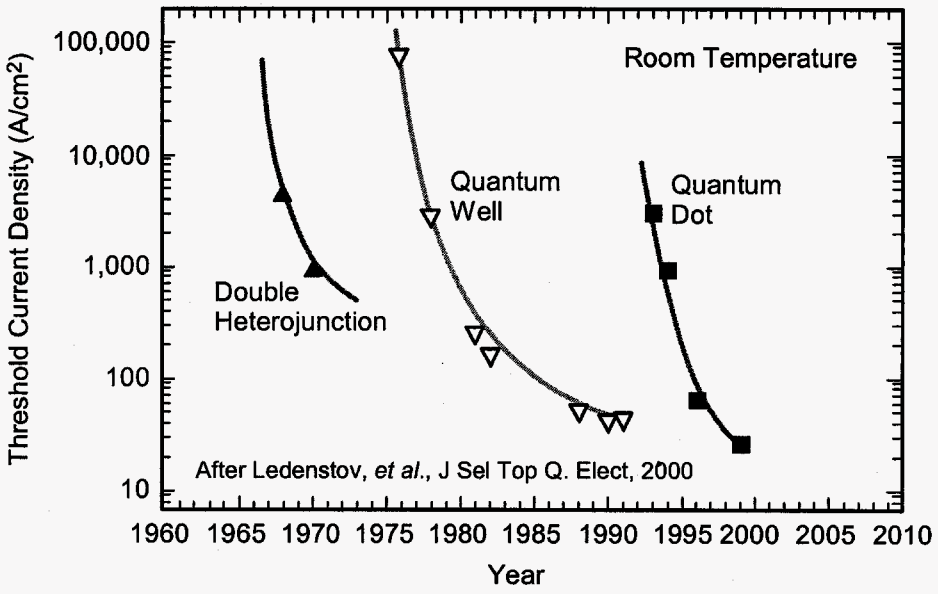

Fig. 17. Trends in threshold current since the first semiconductor lasers were developed in the early 1960s.

Gain is established by the properties of the cavity and the probability of stimulated emission. Figure 18 shows a simplied diagram of a laser diode. Although it appears to be very similar to the previous figure of a heterojunction LED, there are important differences. For a laser, the front and back facets must be parallel in order for photons that are reflected from either facet to have the same direction as other photons that are produced within the active region. Although nearly all of the light within the active region is parallel to the main axis of the laser, some of the light will "spill over" beyond the thin active region, but is confined between the two guiding regions. Light emitted from the active region is diffracted, causing the beam to diverge once it leaves the cavity. Key properties of the laser include the reflectivity from the two parallel facets, non-radiative loss within the cavity (including absorption of some of the photons), and the gain of the semiconductor material.

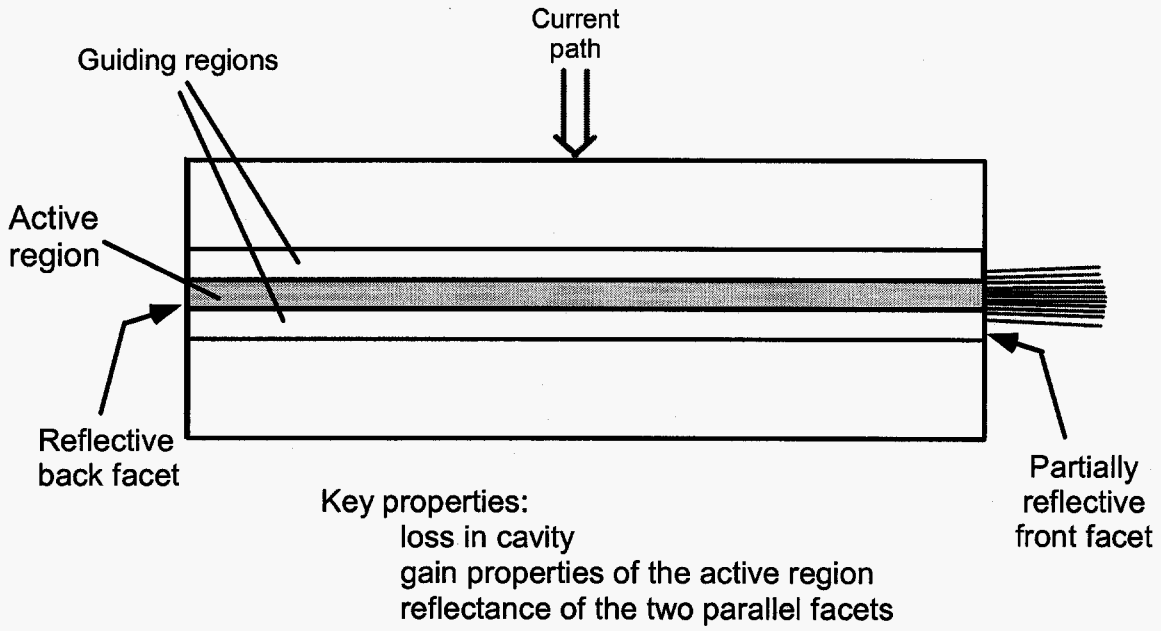

Fig. 18. Basic diagram of a semiconductor laser diode.

The gain depends on current density, as shown in Fig. 19. Three different materials are shown, bulk GaAs; a quantum-well structure in the AlGaAs/GaAs system, and a strained quantum well system using InGaAs. The current density is about three times lower for the InGaAs system compared to bulk GaAs, resulting in lower threshold current. Current densities on the order of 10^2 to 10^3 A/cm^2 are required for laser operation at room temperature. This corresponds to carrier densities ~ 10^{18} cm^{-3}.

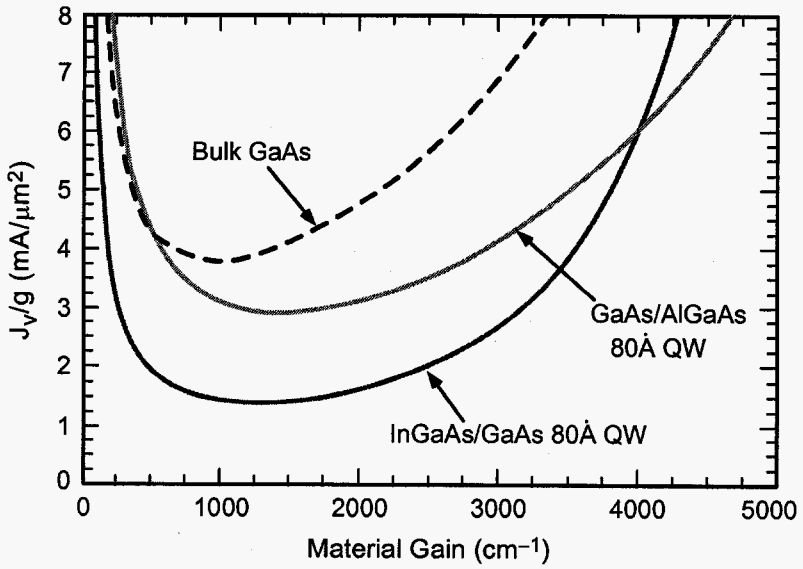

Fig. 19. Material gain vs. current density for three different systems used for semiconductor lasers.

For laser operation we have to consider the balance between various recombination and generation mechanisms. From Fig. 19, gain depends on the cavity length. In order to achieve positive gain, the effect of internal gain from spontaneous emission must balance loss mechanisms from optical absorption, recombination, and reflection. Equating these terms is equivalent to the condition

$$\Re\, e^{[(G_{th}-\alpha)L]} = 1 \tag{9}$$

where $\Re$ is the reflectivity at the back reflecting surface, G_{th} is the threshold gain, α is the absorption coefficient (including recombination terms, which for simplicity are lumped into α), and L is the cavity length. We can consider these terms more explicitly as follows:

$$\frac{\eta I_{th}}{qV} = (R_{non-rad} + R_{spont} + R_{stim}) \tag{10}$$

The recombination terms can be related to carrier density, N. Non-radiative recombination from bulk recombination centers is proportional to N, while Auger recombination is proportional to N^3. The spontaneous recombination term is proportional to N^2. When the carrier density is increased to the point that the spontaneous recombination term overcomes losses due to recombination and optical absorption, then the probability of stimulated emission increases. This defines the threshold carrier density for the laser. As shown in Fig.19, this typically requires a carrier density of 2-4 x 10^{18} cm^{-3}.

A cross section of an edge-emitting laser with five layers is shown in Fig. 20. Current flows vertically from the top contact to the substrate. The current is confined horizontally to a narrow stripe by a combination of oxide isolation under the top metal contact and the use of an n-AlGaAs region at the edge of the two p-regions. That AlGaAs layer has a different bandgap compared to the AlGaAs region immediately below the active GaAs region. This type of construction is referred to as *etched mesa*, because of the way that the active region is formed. Other fabrication methods include *ridge lasers*, where the active region is formed within a physical ridge structure on the top surface, and *buried crescent* lasers, which contain a buried crescent-shaped active region. As discussed earlier, the typical thickness of the active region is 0.2 to 0.3 μm in these types of broad-area lasers.

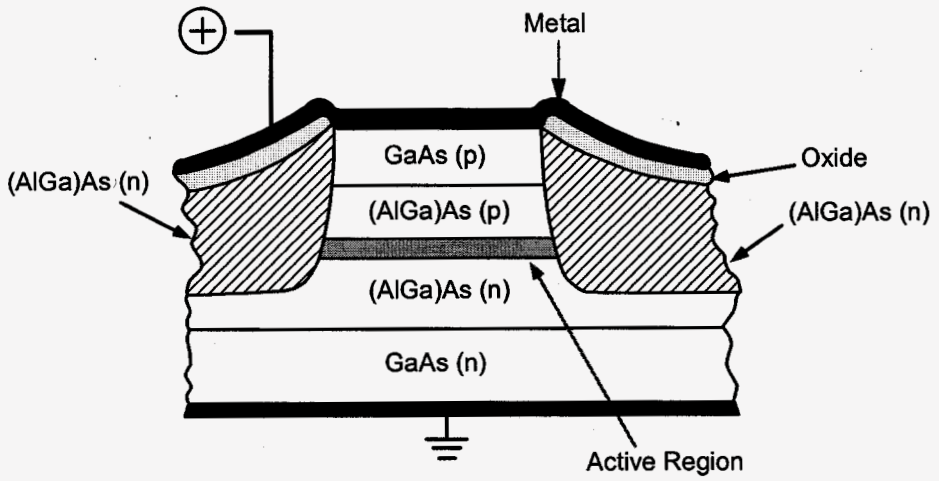

Fig. 20. Diagram of a GaAs laser diode formed with five separate layers.

A more advanced edge-emitting laser is shown in Fig. 21, using AlGaAsP. This laser contains four quantum wells that provide more efficient carrier confinement compared to lasers with larger active layers. Strained-layer technology is used to reduce the threshold current. The quantum wells have dimensions of about 10 nm. Carriers are confined within the quantum well region, and this is the region where photons are produced by stimulated emission. However, the quantum regions are too thin for optical confinement; the evanescent wave will extend beyond them. Cladding layers are placed above and below the active layer for photon confinement.

The n-GaAs layers at the top confine current to the central part of the structure. Additional layers are used to increase efficiency and provide transition regions between materials with different lattice constants (buffer layers). This illustrates the extreme complexity of state-of-the-art semiconductor lasers. Modern fabrication techniques allow the sequence of layers with different composition to be grown with high accuracy.

It is relatively easy to get high power extraction from lasers because the photon direction is essentially normal to the partially reflecting surface. However, diffraction will cause the beam to diverge after it leaves the laser cavity. Lenses can be incorporated into the laser package to reduce beam dispersion from diffraction. Antireflection coatings are nearly always used to increase light extraction efficiency.

Key properties of laser diodes are (a) threshold current, and (b) the linearity of the light output for current above the threshold current (slope efficiency). The threshold current and light output of a laser depend on temperature. There are two ways to deal with this: place the laser in a precisely controlled thermal environment; or monitor the light output from the laser, using feedback to maintain a constant light output when the temperature changes. Many lasers use internal photodiodes – usually discrete photodiodes that are placed within the package- for monitoring purposes, measuring a small amount of light from the back facet. The photodiode signal is then used as part of a feedback circuit to stabilize light output from the laser. However, in some cases degradation of the internal monitor diodes from radiation can be more severe than degradation of the laser.

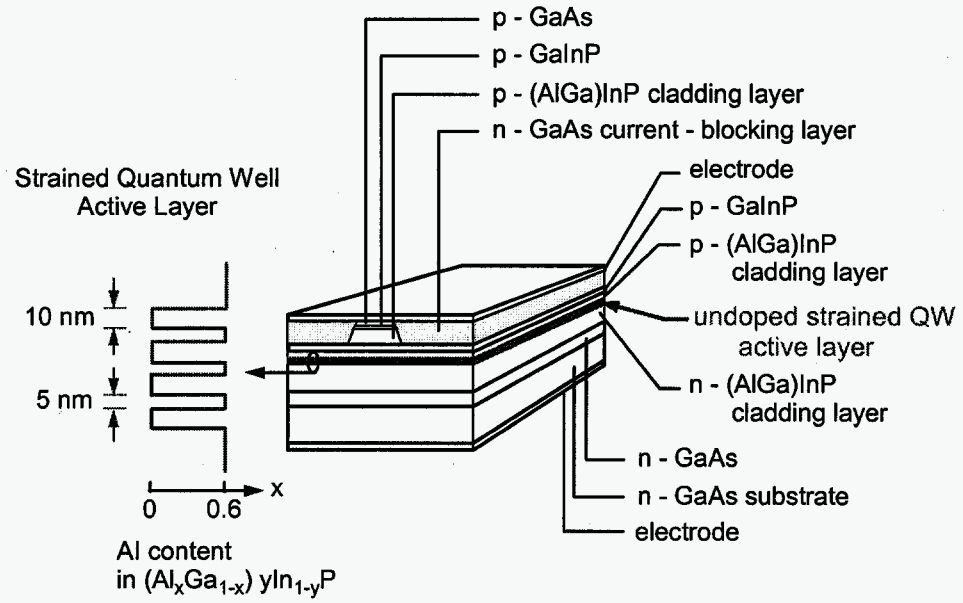

Fig. 21. Diagram of an advanced quantum-well laser using InGaAsP.

Vertical Cavity Surface-Emitting Lasers

Although edge-emitting lasers are very efficient, the geometry is not ideal for coupling to optical fibers, particularly single-mode fibers that have dimensions below 10 μm. Vertical cavity surface-emitting lasers (VCSELs) are lasers with a vertical rather than horizontal structure, using a distributed Bragg reflector at the lower region of the laser for reflection. They were first developed in 1977 using GaInAsP (InP) at 1300 nm [Iga00]. Further details on VCSEL technology are provided in the review paper by Choquette, *et al.* [Choq97].

A physical diagram of a VCSEL structure is shown in Fig. 22 The optical cavity is vertical, using Bragg reflectors at the top and bottom of the cavity with as many as 70 layers. The layers are designed to reflect a specific wavelength. The top layer is partially reflecting to allow a fraction of the light within the cavity to escape from the surface. The active layer is located at the center. It is very thin, on the order of 0.1 to 0.5 μm. Light produced in that thin region is reflected between the Bragg reflectors at the top and bottom of the optical cavity. Selective oxidation is used to limit current flow to a circular region. Although the diagram shows an overall rectangular geometry, some VCSELs are fabricated with cylindrical geometry.

The narrow active region in a VCSEL is buried under many different layers. This limits the ability to extract heat from the laser. Self-heating affects the characteristics of VCSELs, reducing efficiency at higher forward current conditions. Thus, VCSELs are not the best choice for applications involving high power output or linear operation over an extended range of operating currents. However, they can be fabricated with small geometries and very low threshold current, and are particularly useful for fiber optic applications. For example, VCSELs have been produced with threshold current below 1 mA [Iga00].

For VCSELs with small volumes (a necessary condition for very low threshold current), reflection from the cavity causes highly nonlinear behavior with peaks and valleys in the optical power output. This is shown in Fig. 23for 1520 nm VCSELs with two different apertures, 16 and 36 square microns [Sun03]. The oscillatory nature of the L-I characteristics is less evident in

VCSELs with larger cavities, but all VCSELs exhibit this sort of "structure" in the output characteristics because of the presence of so many layers in the Bragg reflector.

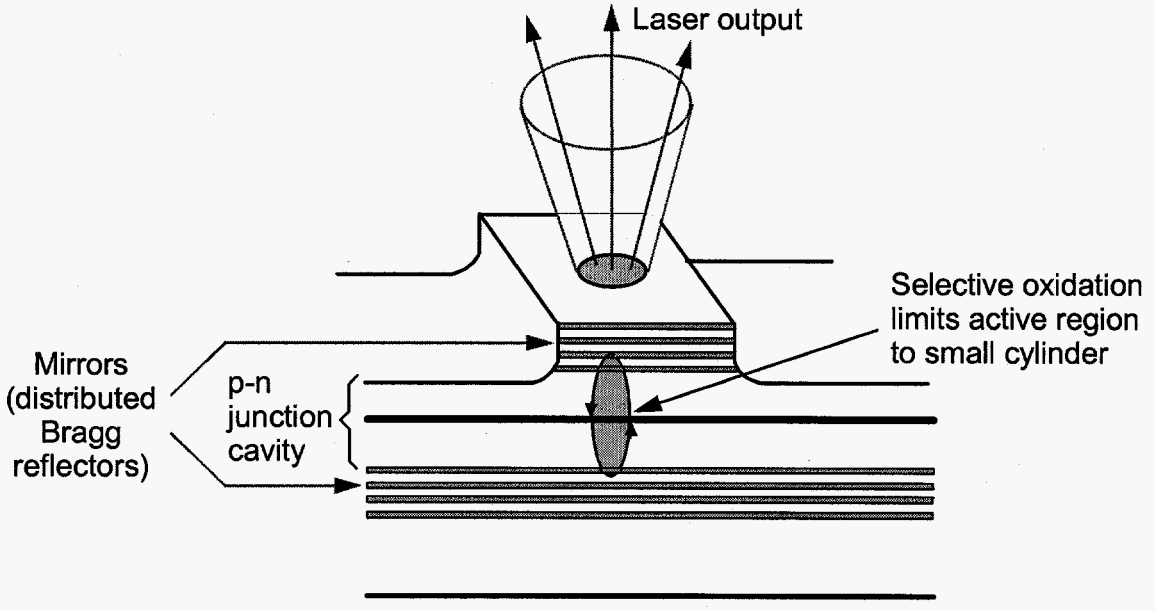

Fig. 22 Diagram of a vertical cavity surface-emitting laser. A circular geometry can be used, providing a small emission area that is easily coupled to small-diameter optical fibers.

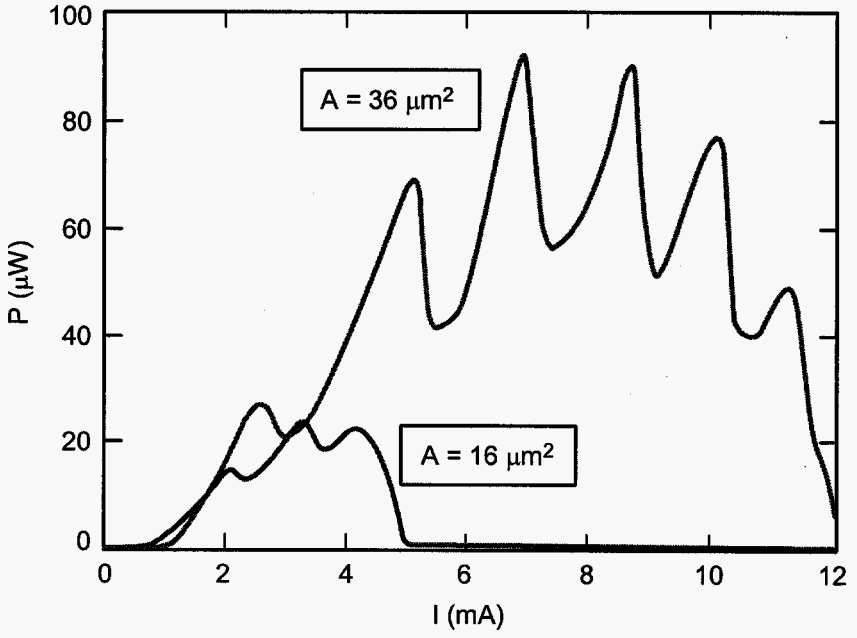

Fig. 23. Optical power vs. forward current for very small VCSELs with threshold current below 1 mA. The nonlinearities in the optical power are caused by the properties of the Bragg reflector [Sun03].

Quantum-Dot Lasers

Quantum dots are fabricated with dimensions that are small enough to cause quantum-mechanical confinement of carriers in both the x- and y-directions, compared to quantum

confinement in a single direction that is done for typical edge-emitting lasers. They have much higher carrier density near the band edges, increasing the optical gain in the material, and reducing the effect of temperature on operating characteristics [Lede00].

Although quantum dot lasers are still in their infancy, the predicted threshold current density is ~ 5 A/cm^2. Arrays of quantum dots can be placed in a laminar region, resulting in higher efficiency and lower threshold current [Park00] compared to an equivalent continuous region with a conventional laser.

Glass-Based Lasers

Conventional glass-based lasers use an amorphous host material doped with an impurity. Because of the amorphous structure, each atom can be considered independently compared to a semiconductor laser that is actually a complex system with many different quantum states. The independent property of glass-based lasers results in much narrower spectral width. Glass-based lasers are pumped with an external light source, typically a flashlamp or an array of semiconductor lasers. They are typically used in special applications requiring high power or narrow wavelengths. The typical cavity length is much greater than the cavity length of a semiconductor laser. We will not discuss radiation damage in these types of lasers. However, the results of one study show the effects of radiation-induced absorption in the host material is an important degradation mechanism [Rose95].

III. Radiation Environments and Radiation Damage

This section of the course provides a very brief review of radiation environments and the interactions of the particles in space with semiconductors. More thorough treatments are given in Section II of the 1997 NSREC Short Course by J. L. Barth [Bart97], and Section II of the 2002 NSREC Short Course by J. E. Mazur [Mazu02], as well as the recent review article by Barth, Dyer and Stassinopoulos [Bart03].

A. Space Environments

The natural space environment consists of particles in trapped radiation belts, as well as high-energy protons and heavy ions from galactic cosmic rays and solar flares. The interaction of heavy charged particles is usually described by means of linear energy transfer (LET), which is a measure of how much energy is lost when an energetic beam travels through a thin slab of material. The units of LET are MeV-cm^2/mg. An equivalent (and more intuitive) way to describe this is in the charge deposited in a material within a unit path length, (LET*). The units of LET* are pC/μm. Although more intuitive for semiconductor device analysis, LET* depends on the density of the target material, while LET does not. For silicon, LET* ~ 0.01 LET; i.e. an LET of 10 MeV-cm^2/mg is equivalent to depositing 0.1 pC/μm. For GaAs, LET* is ~ 0.018 LET, and a particle with LET = 10 MeV-cm^2/mg deposits 0.18 pC/μm.

The distribution of galactic cosmic rays is shown in Fig. 24. Particles emitted by the sun during periods of high solar activity lower the galactic cosmic ray flux by about a factor of 4 compared to the value shown in Fig. 24, which represent the flux during solar minimum conditions (or at extreme distances from the sun). This is referred to as solar modulation.

Once the energetic particles reach the earth, the earth's magnetic field deflects many of the energetic particles, modifying the GCR flux for orbits around the earth. For orbits with high inclination, the GCR flux is relatively unaffected by geomagnetic shielding near the poles, and during the period when the spacecraft is near the poles it will be exposed to nearly the same GCR flux as in free space. For a 705 km high-inclination orbit, the net effect is to reduce the average flux by a factor of about 5 compared to free space. For lower inclination orbits, only particles

with lower atomic number can get through the geomagnetic shielding, as shown in the lower curve in the figure.

Note the very strong decrease in particle flux for LETs above approximately 30 MeV-cm^2/mg. This is called the "iron threshold" because it corresponds to the LET of energetic iron nuclei in the GCR environment. There are relatively few particles with LETs above that value, which is often used as a benchmark for characterizing components. Note however that a particle that traverses a material at an angle will deposit more charge in a given thickness simply because the path length increases by $1/\cos(\theta)$, where θ is the angle of incidence. Thus, the effective LET for particles with LET = 30 MeV-cm^2/mg at normal incidence is 60-75 MeV- cm^2/mg, depending on assumptions about how charge deposited laterally is collected by the active node.

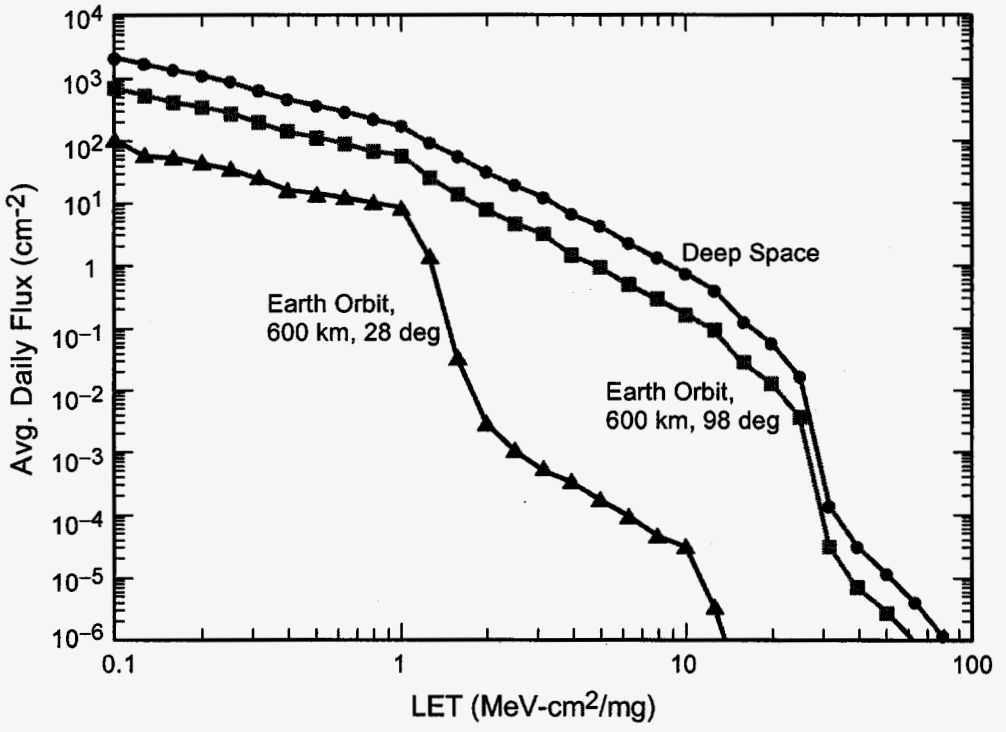

Fig. 24. Distribution of galactic cosmic rays vs. LET for deep space as well as for two different earth orbits during solar minimum. Particles emitted from the sun during solar maximum reduce the average daily flux by about a factor of four near the earth (solar modulation is less significant near the outer planets).

Earth Radiation Belts

The earth's trapped radiation belts consist of an inner proton radiation belt as well as inner and outer radiation belts of energetic electrons (we will ignore the inner electron belt in this abbreviated treatment). The proton belts begin at an altitude of about 700 km, extending to approximately 20,000 km (the altitude also depends on longitude). Proton energies in the trapped belts extend to several hundred MeV. See Barth, *et al.* for more details.

There is a distortion in the belt structure near South America due to slight misalignment between the earth's axis of rotation and the central axis of the magnetic field. This causes the proton belt to "dip". Low-inclination spacecraft will be exposed to that distorted region of the proton belt when their orbits pass through the South Atlantic anomaly.

The outer electron belt starts at about 15,000 km, extending to much higher altitudes. The distance of the outer electron belt to the earth's surface depends on latitude. Electron energies extend to about 20 MeV, with a peak in the energy distribution of approximately 3 MeV.

Radiation Belts Near Jupiter

Jupiter has a strong magnetic fields, which can trap highly energetic particles. Information on the Jovian radiation belts was obtained from interplanetary missions, but is obviously less complete than information on trapped belts near the earth. The trapped belts near Jupiter contain electrons, protons, and other charged particles [Devi83]. Proton intensities in the Jovian belts are several thousand times greater than the intensities in the earth's radiation belts, but have lower energies compared to trapped protons near the earth. On the other hand, the electron energies in the Jovian trapped belts extend to several hundred MeV, much higher than electron energies in the earth's radiation belts. In order to deal with these intense radiation fields, spacecraft that operate near Jupiter have to be designed to meet higher radiation levels. Their orbits are carefully chosen to avoid the peak regions of the radiation belts.

Representative radiation levels for typical spacecraft are shown in Table 3, assuming that a 100-mil aluminum shield surrounds the spacecraft electronics. The amount of shielding is very important, particularly for shielding thicknesses that are less than 100 mils (equivalent) of aluminum. Even thin shields remove most of the low energy particles from the environment.

Nominal radiation requirements are usually established for a spherical shield with a thickness that approximates the thickness of enclosures around electronics. In most applications far more shielding is actually present on the spacecraft. Most systems take advantage of the inherent shielding provided in the structure and electronic boxes to further reduce the total dose. The values in Table 3 are only approximate, and usually assume that one or more severe solar flares will be encountered during the mission.

Table 3
Total Dose Requirements for Representative Space Missions

Description	Orbit	Operating Time (years)	Total Dose rad (SiO_2)
Space Station	500 km 54 degree	10	5×10^3
High-inclination earth orbiter	705 km 98 degree	5	2×10^4
Geostationary	36,000 km	5	5×10^4
Mars Surface Exploration	NA	3	5×10^3
Mission near Jupiter	NA	9	1.5×10^5 – 2×10^6

Requirements for single-event effects are much more difficult to define because of distribution of ion types and energies in space, as well as changes in solar activity. Proton single-event upset is also influenced by the South Atlantic anomaly in the earth's trapped radiation belts (see the 1997 and 2002 Short Course references for more details).

The error rate for memory cells or registers is often used as a benchmark for single-event upset, although there are other effects (including latchup) that can be even more important. A more complete discussion of single-event upset effects can be found in the review articles by Dodd and Massengill [Dodd03] and Sexton [Sext03]. Commercial silicon-based devices have

error rates on the order of 10^{-6} to 10^{-8} errors per bit day in a deep space or geostationary environment. It is often possible to use error-detection-and-correction or other system-level approaches to deal with these types of upset effects. The alternative is to use special hardened circuits. As discussed in Section VII, logic circuits that use compound semiconductors are somewhat more sensitive to single-event upset than comparable silicon technologies [Weat04]. However, compound semiconductor structures are not sensitive to single-event latchup.

Basic Effects in Semiconductors from Protons and Electrons

Ionization effects from heavy particles were discussed earlier in this section. Because there are so few particles, permanent damage effects from galactic cosmic rays can usually be ignored. The brief discussion below compares ionization and displacement damage effects from high-energy electrons and protons.

Space environments can generally be divided into (a) permanent damage effects from high-energy electrons and protons that produce *uniform* damage within a semiconductor device, and (b) *highly localized* ionization or displacement effects from the single interaction of a cosmic ray or proton. Although total dose is the dominant damage mechanism for many types of semiconductors, displacement damage is usually more important than ionization damage for optoelectronic devices, and nearly always has to be considered when evaluating optoelectronics for space applications.

B. Special Environments: Nuclear Reactors and Particle Accelerators

For nuclear reactors, the primary concern is displacement damage from neutrons and decay products from activated material, and ionization damage. Very high radiation levels – in the multi-Megarad region – may be required, particular for worst-case operational scenarios. Many compound semiconductor devices are highly resistant to ionization and displacement damage, making them good candidates for use at nuclear reactor facilities. We will not discuss these environments, but it is important to realize that there are important applications of photonic components that have much higher equivalent radiation levels than typical space environments.

High radiation requirements may also occur for electronics associated with particle accelerators. For example, the Large Hadron Collider at CERN has very high radiation requirements, involving particles with far higher energies than those encountered in space.

C. Fundamental Interactions

Five types of particles are usually considered in radiation environments: gamma rays, electrons, protons, neutrons, and energetic nuclei from space or from nuclear fission.

Gamma rays and electrons are often lumped together because the primary way in which they lose energy is through ionization. Ionization produces electron-hole pairs within semiconductors and insulators. This can cause charge to be trapped at interfaces between semiconductors and insulators. Although that mechanism is extremely important for silicon devices, it is much less important for compound semiconductors because insulating materials do not exist in compound devices with the high quality and low interface state density that is present in silicon dioxide. Consequently, most compound semiconductors are relatively immune to ionization radiation damage at levels below 1 Mrad(GaAs) [Srou88].

Protons also produce ionization, and proton ionization is a significant part of the total dose for most space missions. In addition, protons interact with lattice atoms, where they can impart sufficient energy to move atoms from their normal lattice position to a resting point that can be quite distant from the original lattice site. These displacement effects introduce a great deal of

damage in the lattice, and are a major concern for most optoelectronic components. Neutrons produce similar displacement effects. Displacement damage has three important effects: Minority carrier lifetime is reduced; carrier mobility is reduced; and the effective doping level can be altered because of carrier removal.

High-energy nuclear particles also produce displacement damage and ionization. However, for those particles the most important consideration is usually single-event upset, not permanent damage effects. Single-event upset is a circuit effect that occurs because the interaction of a single charged particle produces a small but significant amount of charge that can be collected at sensitive circuit nodes, causing stored information in a memory or flip-flop to be altered. Integrated circuits manufactured with compound semiconductors can be very sensitive to single-event upset effects.

D. Energy Dependence of Displacement Damage

The energy dependence of displacement damage effects is very important because the space environment consists of a spectrum of electrons and protons with a wide range of energies. We need to understand the dependence of fundamental interactions on energy in order to relate experimental results at one or more energies to the actual space environment. Early work in the 1980's developed the concept of non-ionizing energy loss (NIEL) for this purpose. The initial work started with theoretical calculations that partitioned energy loss into ionizing and non-ionizing components [Summ87]. For silicon, experimental work was in reasonable agreement with theory, as summarized in Fig. 25 [after Summ93]. Electron damage increases with energy, with a minimum energy of approximately 150 keV to transfer enough energy to displace a silicon atom. Protons have a much stronger energy dependence, which increases at low energy because the interaction is electromagnetic. Slow protons spend more time in the vicinity of lattice atoms when they travel at lower velocity, increasing the amount of energy that is transferred to the nucleus. A recent review of displacement damage effects in silicon can be found in the paper by Srour, C. Marshall and J. Marshall [Srou03].

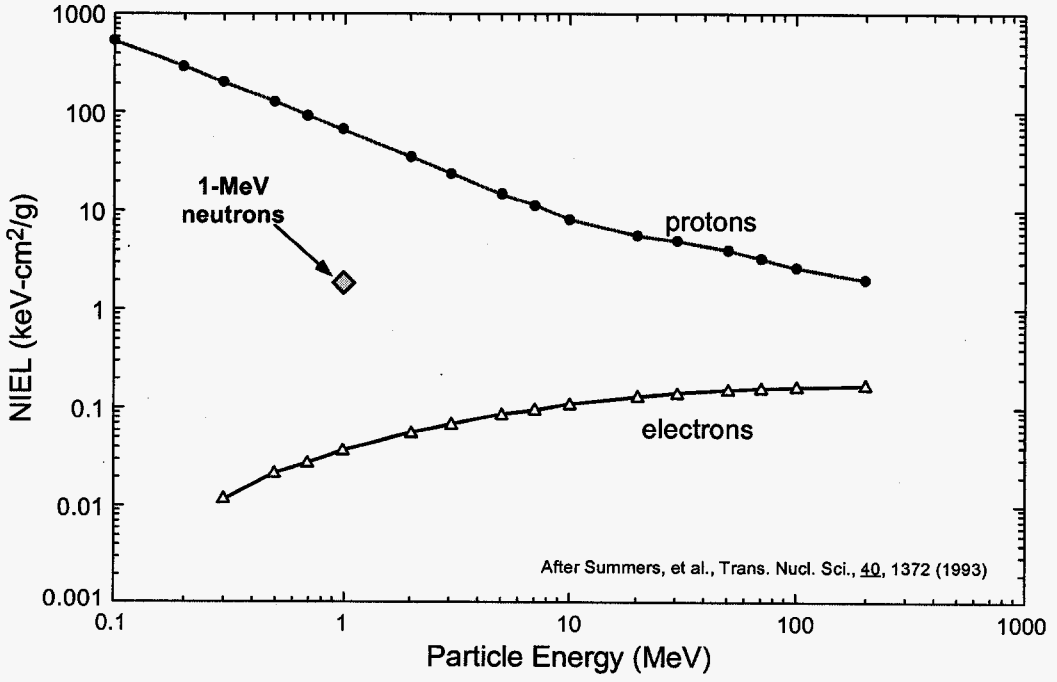

Fig.25. Dependence of non-ionizing energy loss in silicon for electrons, protons and 1-MeV neutrons on the energy of the incident particle.

The energy dependence of proton damage in GaAs is shown in Fig. 26, taken from the work of Barry, *et al.* [Barr95]. Unlike silicon, for GaAs there is considerable disagreement between the theoretical calculations and experimental results, particularly for protons with energy above 50 MeV. Differences as high as a factor of 6 have been reported between theoretical calculations of NIEL (with secondary corrections to improve accuracy) and experimental results for light-emitting diodes [Barr95], as shown by the open circles in Fig. 26. The underlying reasons for these differences are still not understood, and are the subject of current research [Reed00, Walt01].

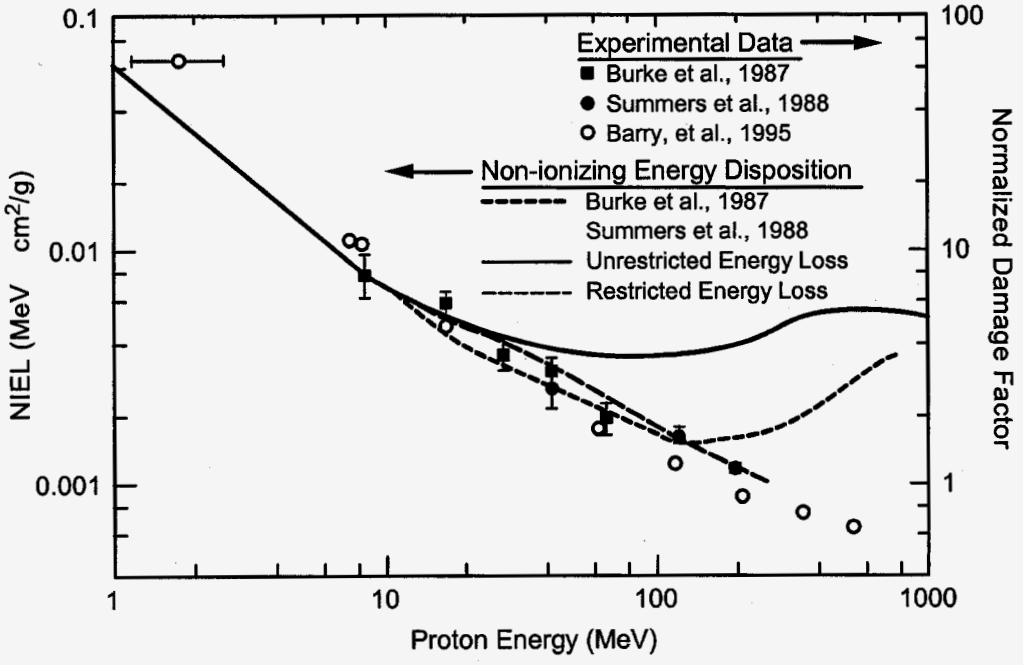

Fig. 26. Calculations of the energy dependence of NIEL for protons in GaAs, showing discrepancy between theory and measurements of energy dependence in GaAs LEDs for energies above approximately 30 MeV [Barr95].

The uncertainty in energy dependence has important consequences, particularly if radiation tests are done at high energies, for example 200 MeV protons, which are readily available at some facilities. The difficulty is that the actual proton environment of many space systems consists of a spectrum of energies, with mean energies between approximately 25 and 50 MeV. For example, Fig. 27 shows the distribution of proton energies for a high-inclination 705 km earth orbit. Although adding shielding shifts the peak in the energy spectrum to higher energies, the peak energy for this spectrum remains below 50 MeV. Consequently, most of the damage will be caused by protons with energies below 50 MeV, taking into account the increase in NIEL at low proton energies.

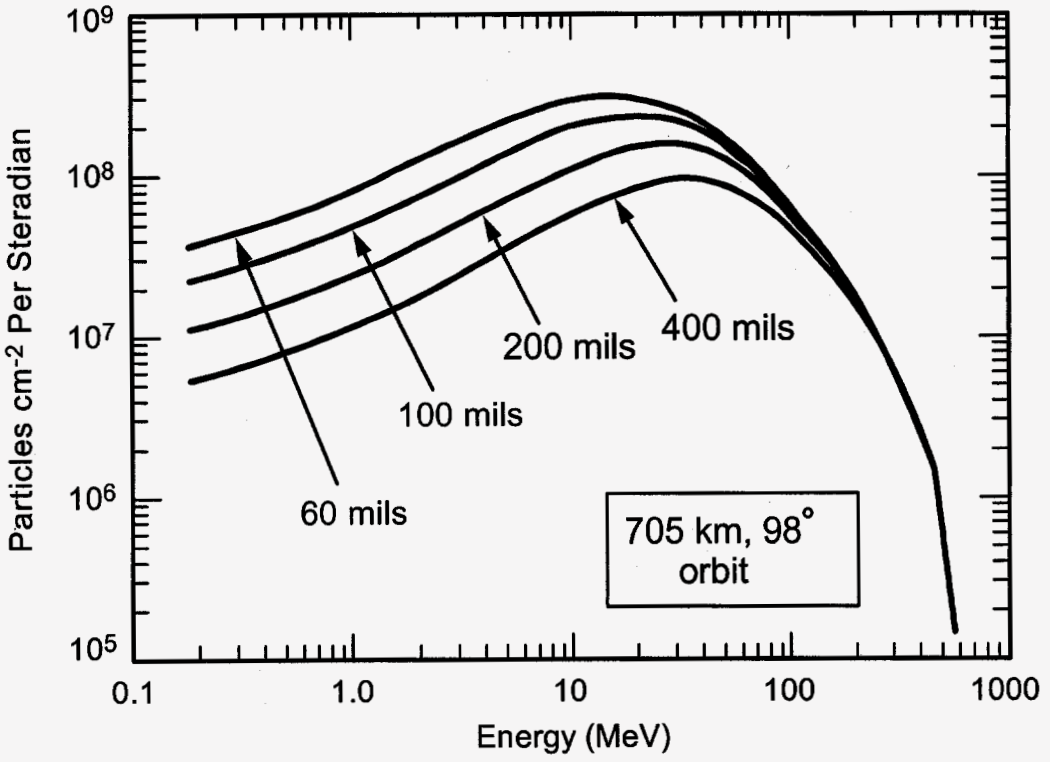

Fig. 27. Proton energy spectrum for a 705 km, 98 ° orbit with various aluminum spherical shield thicknesses.

If the NIEL energy dependence continues to decrease at high energy, tests at 200 MeV will cause less damage, leading to serious under-estimation of the effect of the actual proton spectrum on the device. For this reason, tests at lower energies – 50 MeV - are recommended for III-V devices. That energy is near the peak energy in typical proton spectra, and is in a region where there is good agreement between NIEL calculations and experimental results. The 50-MeV protons have a range of more than 400 mils in aluminum, which provides sufficient range to penetrate the "dead" regions and packaging of most devices without significantly degrading the proton energy when it reaches the active region of the structure. We will base most of the discussion of device responses in this chapter of the short course on equivalent damage with 50-MeV protons.

D. Radiation Testing with Protons

There are some unique problems that have to be dealt with when radiation tests are done with protons. The strong dependence of NIEL on proton energy for energies below 50-MeV can introduce errors in experimental interpretation because part of the proton energy will be lost when the proton beam goes through packaging or optical windows, reducing the energy of protons that strike the active region. In many cases the active region of an optical device is located beneath several layers of semiconductor, or beneath clear optical compounds that are used for index matching to improve optical coupling efficiency.

The range of protons (in aluminum) with various energies is listed in Table 4. Corrections must be made for different types of materials, multiplying by the density of the material. For energies above 50 MeV the range is usually large enough so that corrections for energy loss in the structure are unnecessary, provided the irradiation is done with the beam at normal incidence. However, the range is very limited for lower energies.

Another potential interference effect is darkening of optical windows, lenses, or index matching materials. These effects are not always important, but there are cases where the ionization damage associated with proton tests can produce substantial absorption within such materials, altering the test results. One way to check for this is to irradiate some samples with gamma rays, comparing the results with proton tests at equivalent total dose levels. It is often possible to directly test such materials by disassembling one or more devices, and evaluating absorption on the intervening material separately.

Table 4. Range in Aluminum for Protons with Various Energies

Proton Energy (MeV)	Range in Aluminum (mils)	Range in Aluminum (μm)
10	5.89	150
15	22.4	569
20	81.6	2,040
50	420	10,670
100	950	24,200

IV. Radiation Damage in Optical Emitters

Optical emitters are relatively unaffected by ionization damage because compound semiconductors do not have high quality insulators, and already have high densities of surface states. In many cases special buffer layers are used that isolate the buried active region from the surface, further reducing the importance of additional recombination at surfaces. The dominant radiation damage mechanism in most optical devices is displacement damage. The relatively slight degradation that occurs in LEDs and laser diodes from irradiation with cobalt-60 sources is actually caused by displacement damage from the Compton electrons produced by the gamma rays, not ionization damage. Despite this general sensitivity, many optical emitters are relatively immune to displacement damage effects because they use thin active regions, with relatively high doping levels.

A. Light-Emitting Diodes

The sensitivity of light-emitting diodes to displacement damage effects varies by more than four orders of magnitude, depending on the specific design of the LED. Amphoterically doped LEDs are among the most sensitive components, degrading significantly at a nominal fluence of 10^{10} p/cm^2 (50 MeV). This corresponds to about 1.6 krad in a space environment dominated by protons, a very low radiation level. Optical couplers using this type of LED have failed in space applications [Swif03].

The most straightforward way to evaluate LED degradation is to compare the light output after irradiation with pre-irradiation light output. This is shown in Fig. 28 for two types of LEDs made by one manufacturer for high-reliability space applications. The first type of LED is amphoterically doped; the second uses a more complex process with double-heterojunctions. It is clear from this figure that the amphoterically doped LED is far more sensitive compared to the double-heterojunction counterpart. However, this extreme sensitivity is partially offset by the much higher efficiency of the amphoterically doped LED.

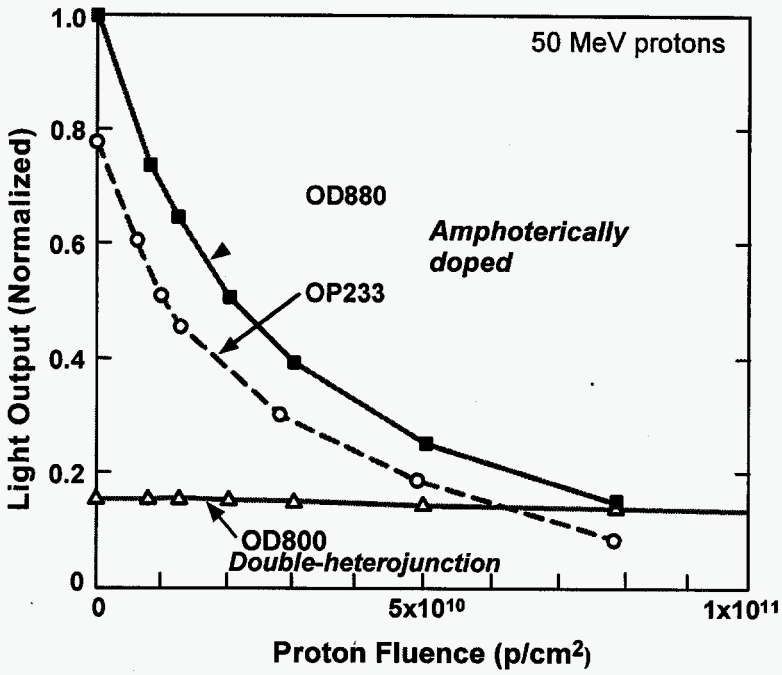

Fig. 28. Fractional light output after proton irradiation for two types of LEDs, normalized to the higher optical output power of the amphoterically doped LED.

When LED damage is evaluated at constant injection conditions (fixed current) the damage is actually *superlinear* with fluence provided that the recombination centers introduced by the radiation are uniformly distributed within the bandgap. A more sophisticated way to deal with the degradation is to fit the damage to a power law, using the equation below [Rose82]

$$[\,(I_o/I)^n \; - \; 1\,] = \quad (K\,\tau)\;\Phi \tag{11}$$

where I_o is the pre-irradiation intensity, I is the light intensity after irradiation, **n** is an exponent between 0.3 and 1, $(K\tau)$ is a damage constant that includes the minority carrier lifetime, and Φ is the particle fluence. For LEDs that are dominated by lifetime damage, the quantity at the left side of the equation is linearly related to fluence when n = 2/3. Fig. 29 compares degradation data for n = 1 and n =2/3; note the nearly linear behavior for n = 2/3.

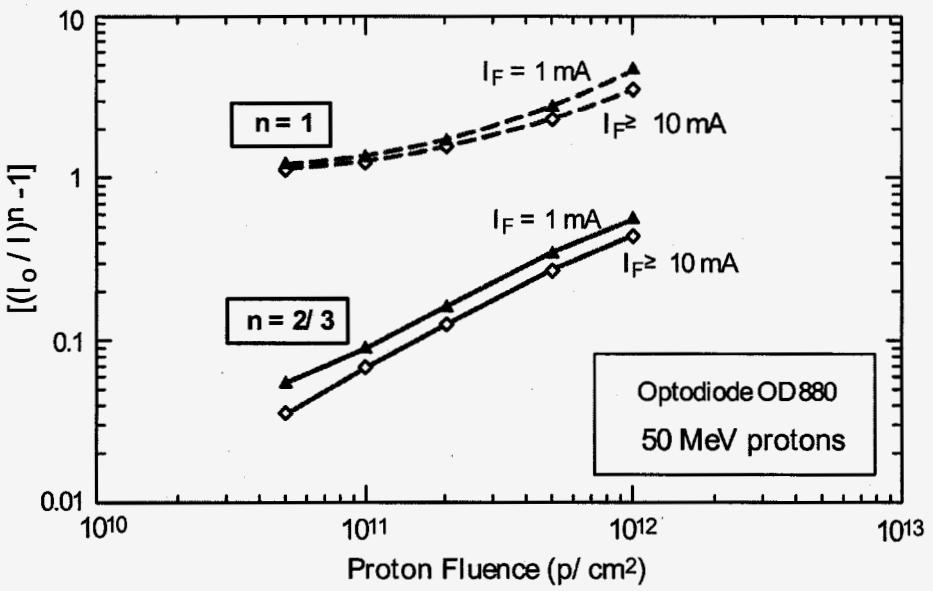

Fig. 29. Superlinear damage in an amphoterically doped LED that can be linearized by using an exponent of 2/3 in the expression at the left side of Eq. 11.

Although this is a valid way to examine LED damage, the 2/3 power relationship usually does not linearize damage in heterojunction LEDs. For those types of LEDs, the damage (as described by Eq. 11) is linear for values of n that are very close to unity. Thus, the main advantage of Eq.11 is to linearize the superlinear damage amphoterically doped LEDs. However, the equation can still be used for heterojunction devices with n = 1, providing a linear metric for degradation.

A more straightforward way to examine LED damage is to show the fractional remaining optical power output as a function of fluence. This is shown in Fig. 30 for double-heterojunction LEDs with several different wavelengths. The 660 nm LED is fabricated with GaAsP, while the others use AlGaAs. The dashed line shows the degradation of an amphoterically doped LED for comparison. This figure does not take unit-to-unit variability of damage into account, which is typically a factor of two for most types of LEDs.

LEDs are also available at longer wavelength that are optimized for high-speed operation in fiber-optic data buses. Those LEDs degrade even less than the heterojunction LEDs in Fig.30, but operate above the cutoff wavelength for silicon detectors.

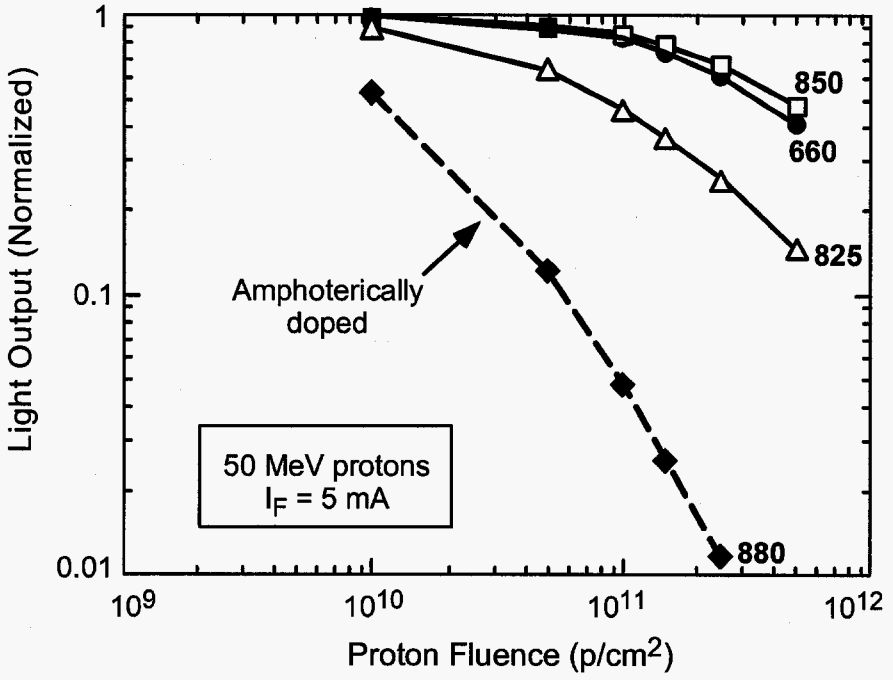

Fig. 30. Fractional change in light output after irradiation with 50-MeV protons for several different types of LEDs.

Optical power degradation in Fig. 30 was evaluated at a forward current of 5 mA, about 5% of the maximum forward current. Less damage occurs when LEDs are measured at high forward current, and it is usually advisable to characterize LED degradation at several different forward current conditions that overlap various use conditions. Note however that most applications use forward current well below the maximum rated value because of reliability concerns.

LEDs are subject to gradual degradation (wearout) during operation, and the rate of degradation is much greater at high forward currents [Witt96]. Radiation damage in LEDs that have been operated over extended periods (with up to 20% wearout degradation) is very similar to degradation in LEDs that have not been subjected to wearout [John00], and thus reliability and radiation degradation can be considered independently.

Annealing

Displacement damage in LEDs anneals after irradiation. Although annealing in non-operating LEDs can be instigated by heating, temperatures above 200 °C are required [Loo81], which is well above the maximum allowable operating temperature of typical LEDs. The most important factor in LED annealing is forward current injection, which causes damage to anneal even at room temperature. Irradiated LEDs can be stored *without forward current injection* for six months or more without appreciable change in the degraded characteristics. However, as soon as a forward current is applied, the damage begins to recover. It is possible to take advantage of annealing to reduce the effects of radiation damage. This was done recently in the Galileo space system after proton damage caused circuit failure in an LED application [Swif03].

Although annealing can be used to advantage, the sensitivity of some types of LEDs to injection-enhanced annealing introduces possible errors and inconsistencies in evaluation of radiation degradation. For example, if irradiations are done using samples that are under forward bias, the forward injection will significantly change the amount of degradation that is observed. If the devices are left in this condition after irradiation (as well as before each irradiation if a series of stepped irradiations are done), this will also affect the results. Thus,

injection-enhanced annealing can be a serious interference effect during testing. It is far more straightforward to test devices in an unbiased condition, and evaluate the effects of injection on damage recovery afterwards.

Measurements have to be carefully planned to avoid interference from annealing, using pulsed measurements and limiting the current that flows through the device when devices are evaluated after irradiation. Although this is relatively easy for optical power measurements, it may be impossible to measure spectral characteristics without inadvertently annealing the damage because most spectrometers take several minutes to sweep the grating within the light source.

An example of injection-enhanced annealing in an amphoterically doped LED is shown in Fig. 31. Two curves are shown, corresponding to two different proton energies. The optical power immediately after irradiation was reduced to about 10% of the initial value, and the damage is calculated using the 2/3 power relationship shown in Eq. 11. The forward current during the extensive annealing time was 10 mA. Initially there is little effect. The damage begins to recover after 10 seconds, and continues to recover for several decades. Saturation in the recovery characteristics is evident at about 3 x 10^5 seconds (4 days). More of the damage recovers for the device irradiated with 25 MeV protons compared to the device irradiated at higher energy. The maximum amount of damage that can be recovered through annealing is 30 – 40%.

Annealing proceeds faster when higher forward currents are used. Fig. 32 compares results for three different currents – 5, 10 and 50 mA – for an amphoterically doped LED with a maximum rated current of 100 mA [John00]. The abscissa shows the total charge that has passed through the LED during annealing for the three different currents. The amount of annealing that has occurred is approximately the same for the three conditions. This provides a way to apply annealing results for one set of conditions to a different end-use condition.

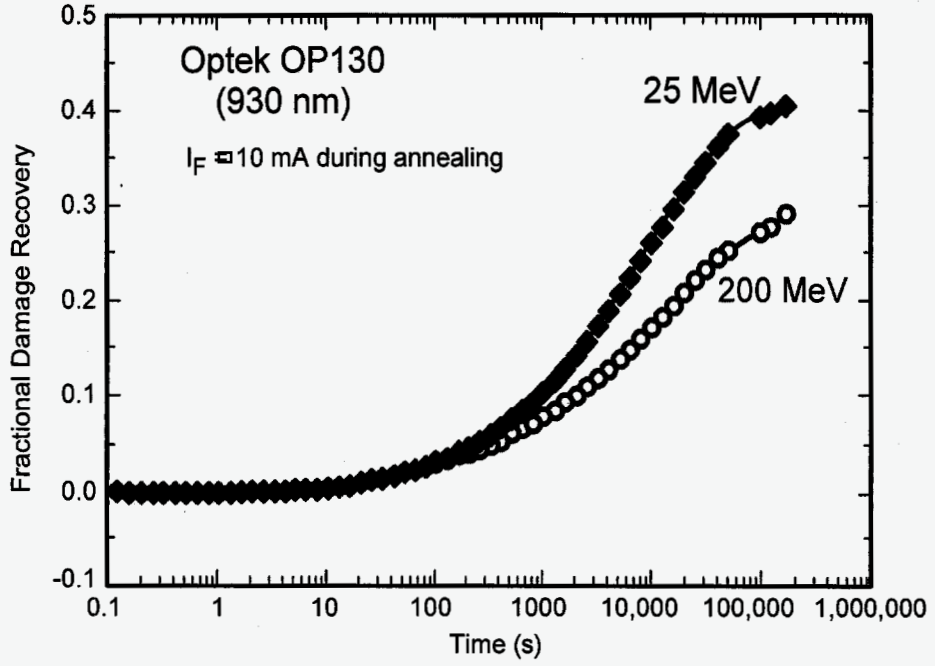

Fig. 31. Annealing of an amphoterically doped GaAs LED when a forward current of 10 mA is applied after irradiation. The recovery is faster for devices that are irradiated with lower energy.

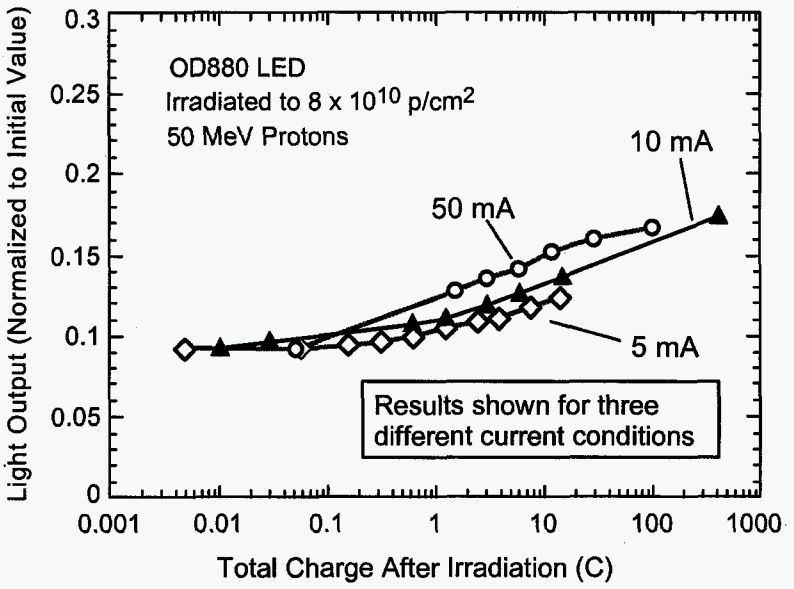

Fig. 32. Comparison of annealing in a AlGaAs LED for three different forward currents. The annealing is about the same for all three conditions when total charge is used to normalize the results.

Amphoterically doped LEDs, which require long minority carrier lifetime for efficient photon emission, are highly sensitive to annealing. In contrast, most double-heterojunction LEDs exhibit very little annealing, 10% or less. This is likely related to the shorter lifetime and the influence of mechanisms other than minority carrier lifetime in degradation of DH LEDs. However, we will see in the next section that damage in laser diodes made with double-heterojunctions can be highly sensitive to injection-enhanced annealing.

B. Laser Diodes

For laser diodes the parameter that is most affected by displacement damage is threshold current. Fig. 33 shows the results of an older study of proton damage in a strained-layer laser diode using InGaAs [Evan93]. They used 5.5 MeV protons in the study, which are about 8.5 times more damaging compared to 50-MeV protons.

The first-order effect of the radiation damage is to increase the threshold current; the change in threshold current is proportional to fluence. Note that the slope of the optical power output – slope efficiency – is essentially unchanged for this particular device, except after the highest fluence where it decreases slightly. Measurements were made at constant temperature, using a heat sink. The maximum current was limited to about 70 mA to avoid excessive heating.

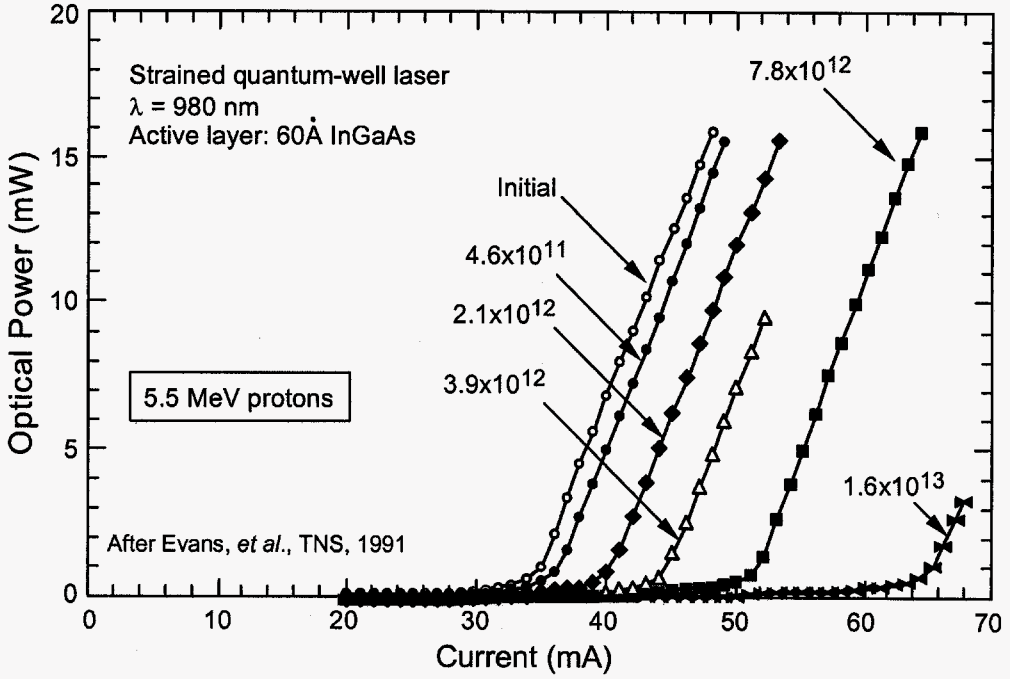

Fig. 33. Degradation of strained quantum-well laser after irradiation with 5.5 MeV protons [Evan93]

A similar set of results is shown in Fig. 34 for a 650 nm laser. The results are generally similar to the results for the 980-nm laser above, but in this case the slope efficiency changes at moderate fluences. The laser temperature was controlled with a thermoelectric cooler, using pulsed measurements to eliminate self heating at higher currents.

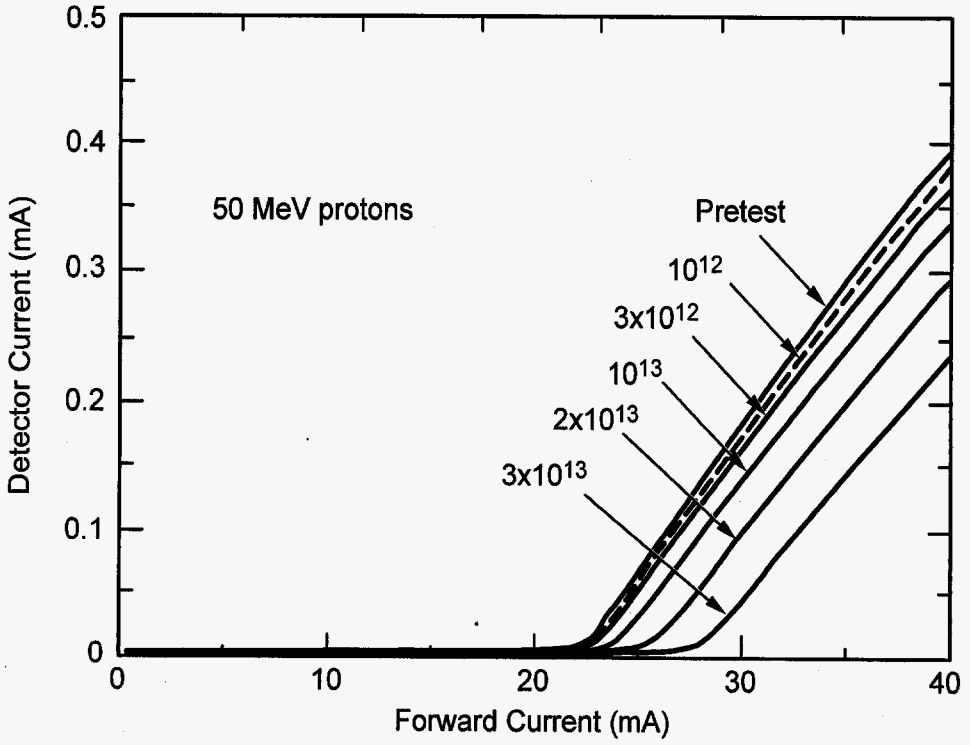

Fig. 34. Degradation of a 650-nm laser after irradiation with 50-MeV protons. Note the decrease in slope efficiency compared to the previous figure.

Although threshold current and slope efficiency are important parameters for laser applications, it is possible to learn more about the internal degradation mechanisms by extending the measurements to low light levels, and plotting the results on a semi-logarthmic plot. The data in Fig. 34 is plotted in this way in Fig. 35. Far more degradation occurs at low currents, below the laser threshold region. The degradation in that region is a better current measure of non-radiative recombination centers than changes in threshold current.

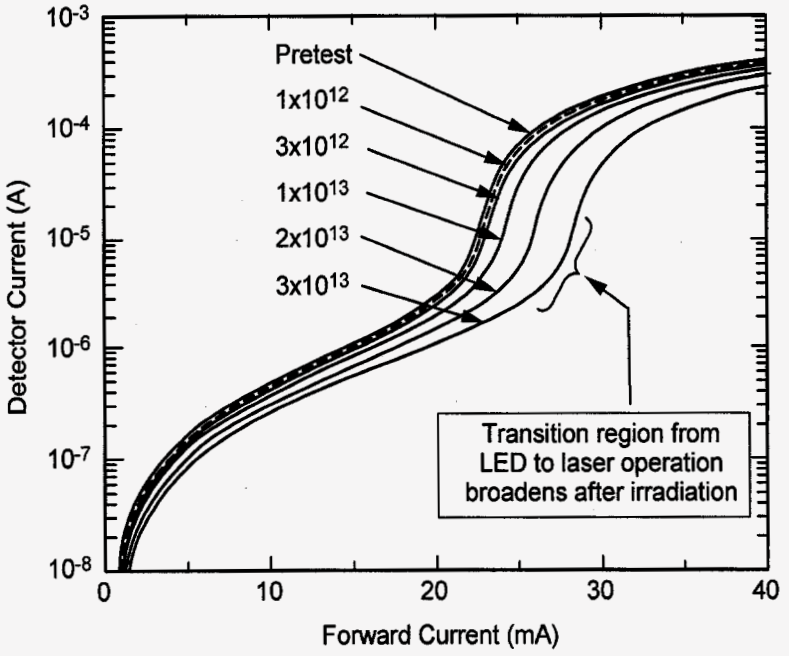

Fig. 35. Results of Fig. 34 plotted semi-logarithmically to show the optical power at low current, where the device functions as an LED.

Another way to examine laser degradation is to plot the derivative of the optical power vs. forward current. That measurement technique provides more detailed information about the behavior of the device in the lasing mode. Fig. 36 shows the derivative of the detector current (optical power) with respect to forward current as a function of forward current. A large increase in the derivative occurs at the threshold current, and the slope of the derivative near the threshold region is only slightly affected by radiation damage. As the current increases above the threshold current, the slope decreases slightly because of internal losses and efficiencies. The slope in that region changes slightly after irradiation because of increased losses within the cavity that cause the transparency density to change. High-quality lasers have slopes that are nearly horizontal over an extended range of current. Although this technique is useful, it requires accurate, stable measurements. The value of the derivative is highly sensitive to noise or measurement instability.

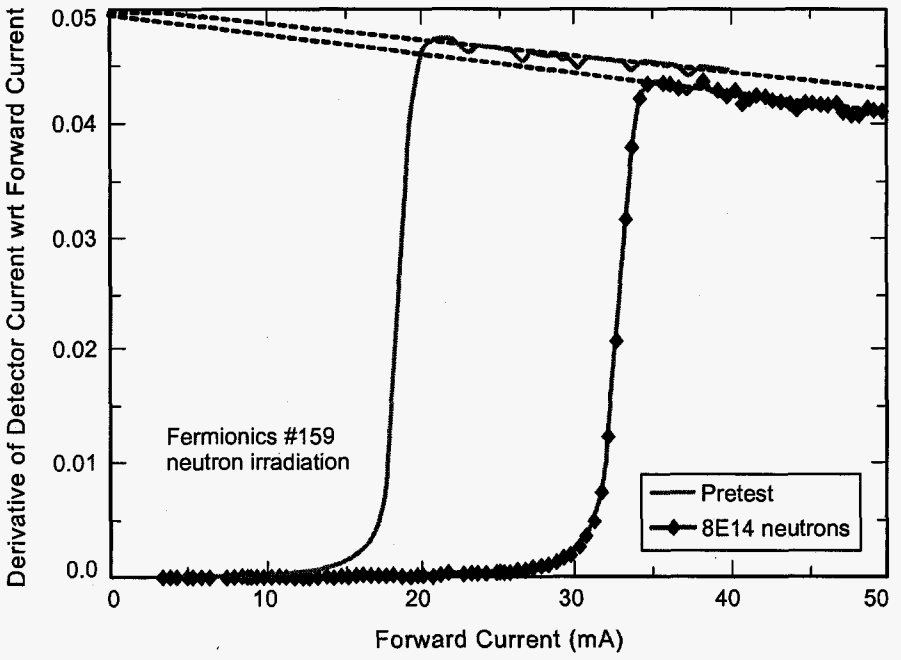

Fig.36. Derivative of optical power for a 1300 nm laser diode before and after irradiation.

VCSELs

Although the operating principles of VCSELs are essentially the same as that of edge-emitting lasers, slight differences in the layer thickness of the Bragg reflector and self-heating are very evident during radiation degradation studies of VCESLs. Self-heating restricts the range of currents over which the device can be operated. Unlike conventional laser diodes, the optical power output has "bumps and wiggles" that correspond to different modes within the complex Bragg reflector. Some VCSELs have significant discontinuities in the optical power curve that can change after irradiation. Fig. 37 shows how optical power in a VCSEL is affected by radiation damage. VCSELs typically have highly nonlinear output characteristics, and nearly always show a decrease in slope efficiency after irradiation.

Many VCSELs have a more gradual transition at the threshold current than shown in the example of Fig. 37 due to the complex nature of the Bragg reflector [Scho97]. This causes some ambiguity in defining threshold current. One way to deal with this is to fit the optical power to a linear relationship near the threshold current, extrapolating the slope to define the threshold condition. It is also possible to use the derivative analysis discussed in the previous subsection. However, the discontinuities in VCSEL output characteristics make this technique less useful compared to edge-emitting lasers.

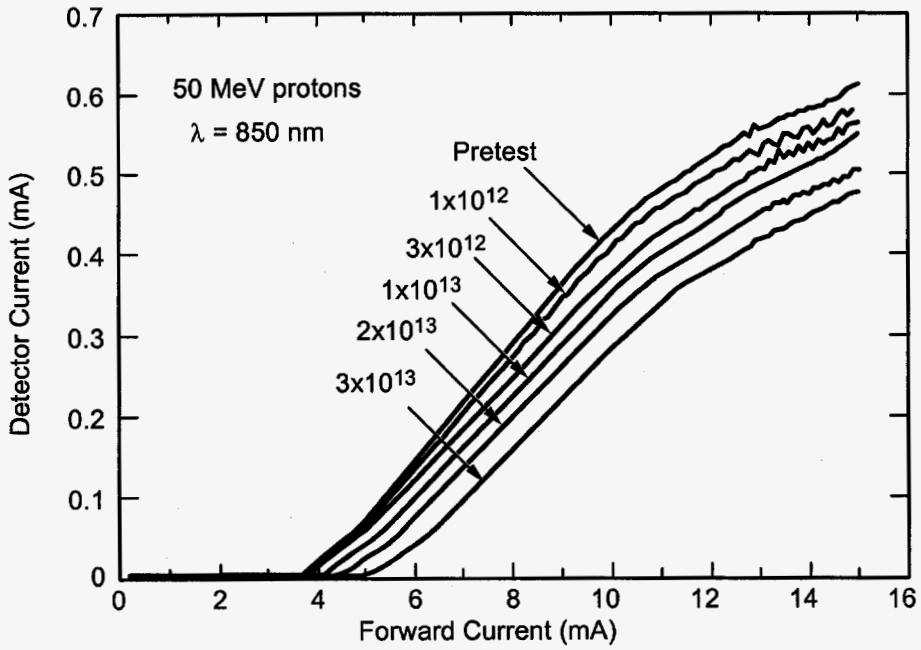

Fig. 37. Degradation of a VCSEL after irradiation with 50-MeV protons. Note the substructure and the decrease in slope efficiency at high operating currents.

Degradation of Various Types of Lasers

From the earlier discussion of lasers in Section III, one would expect that different types of lasers would respond quite differently to radiation damage because different material systems are used in their fabrication. However, that is not the case for lasers that have been evaluated in recent years. The effect of proton irradiation on threshold current is shown in Fig. 38 for several different types of lasers, showing the percent increase in threshold current. All of the tests were done using 50-MeV protons. Even though these lasers have different wavelengths, using different materials, the results are remarkably similar. The slopes of the threshold current vs. fluence are nearly identical for several of the lasers, and the fluence at which the threshold current first begins to change is remarkably close, except for the VCSEL.

We can explain this by re-examining the conditions for lasing in a semiconductor, along with loss mechanisms. In order for lasing to occur, the carrier density must be large enough to "saturate" the bimolecular recombination coefficient, B and obtain a carrier density that is sufficiently high to increase the probability of stimulated emission. However, it turns out that B is nearly the same for the three material systems that we are considering, within about 50%. The other important factor is the gain of the material and laser cavity. The gain curves for the three materials require carrier densities on the order of 1.5-4 x 10^{18} cm^{-3}. The first-order effect of radiation-induced defects is to increase the number of non-radiative recombination centers. As the number of defects increase, we have to compensate non-radiative losses by increasing the carrier density (i.e., current) to the point where the material gain is higher, which causes the threshold current to increase. Approximations for the gain of these three materials have been developed by Coldren and Corzine, showing that the logarithmic dependence of gain on carrier density can be approximated by a linear relationship for small changes [Cold95]. This explains the observed linear dependence of threshold current on proton fluence over the range of changes shown in Fig. 38. Departures from linearity will occur at higher fluences.

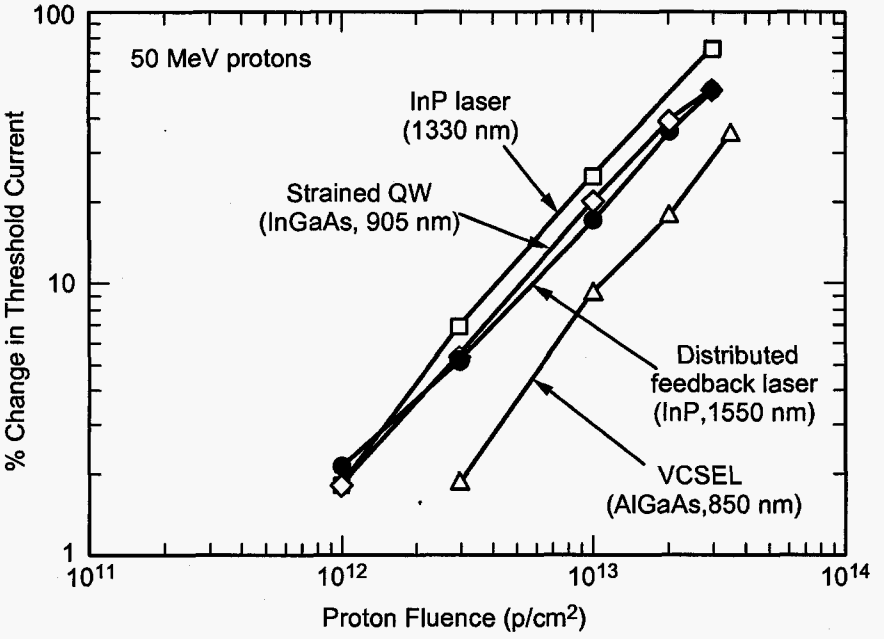

Fig. 38. Threshold current degradation of several different lasers. Note the remarkable similarity in results despite the different materials and wavelengths.

Annealing of Displacement Damage in Lasers

As discussed previously, LEDs that are fabricated with narrow heterojunctions are relatively insensitive to current-enhanced annealing. Thus it is somewhat surprising that lasers, fabricated with similar structures, are highly sensitive to annealing. Annealing was observed in the first radiation studies of laser diodes, but these earlier devices had extremely high threshold current and would only work reliably at liquid nitrogen temperature [Comp67].

Fig. 39 shows annealing results for a contemporary 1300-nm quantum-well laser. The threshold current is approximately 7 mA. First, note that the device that was not operated under forward bias changes very little, even 3 days after irradiation. The device that continually operated at 5 mA, below the lasing threshold, gradually recovers, with a threshold current shift of about 2/3 as great after 3 days of continuous operation. Two of the devices were operated at currents above the lasing threshold, and their recovery is clearly much faster than the device that operated below threshold, in the LED mode.

The current densities are not very different for the device operated below the laser threshold, but the annealing clearly proceeds at a lower rate. This implies that the much higher photon density when the device enters the lasing mode also affects the annealing process. Similar results have been obtained for VCSELs, with even more pronounced recovery for devices where annealing is done above the lasing threshold [John01].

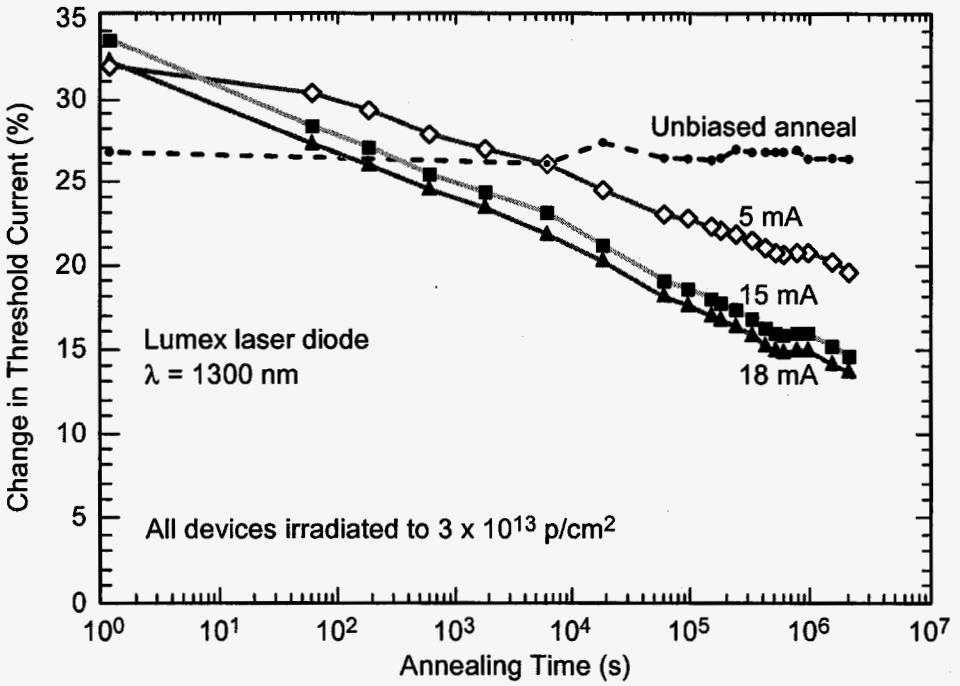

Fig. 39. Annealing of 1300 nm quantum-well lasers under different bias conditions. All four devices were irradiated to a fluence of 3×10^{13} p/cm^2.

Annealing in lasers is still an active research area. Annealing progresses more rapidly after irradiation with protons of moderate energy, e.g. ~ 25 MeV, compared to the annealing rate under similar conditions for lasers irradiated with protons of higher energy [John02]. This is probably related to the microscopic nature of the defects produced by the radiation. Low-energy protons produce large numbers of vacancy-interstitial pairs (Frenkel defects) with relatively few cascade damage regions. The Frenkel pairs are in relatively close proximity compared to cascade damage regions, and can recombine more easily. Compared to protons, neutrons produce large numbers of cascade damage regions. Fig. 40 compares annealing results for 1300 nm laser diodes that were irradiated with 50-MeV protons and fission neutrons (normalized to 1-MeV equivalent fluence). Proton damage not only proceeds more rapidly, but a larger fraction of the damage recovers. Data for extremely energetic protons- 24-GeV – are also shown in the figure (from [Gill00]), but are for laser diodes from a different manufacturer.

Although proton damage is usually stable for devices that are not operated after irradiation, results for neutron irradiation show significant recovery even in unbiased devices [Gill00]. The reason for this difference in stability without applied bias has yet to be explained. It is evident that more work needs to be done on annealing in laser diodes in order to determine how injection, optical power, particle type and energy influence annealing. The device structure and specific semiconductor material may also play important roles in annealing.

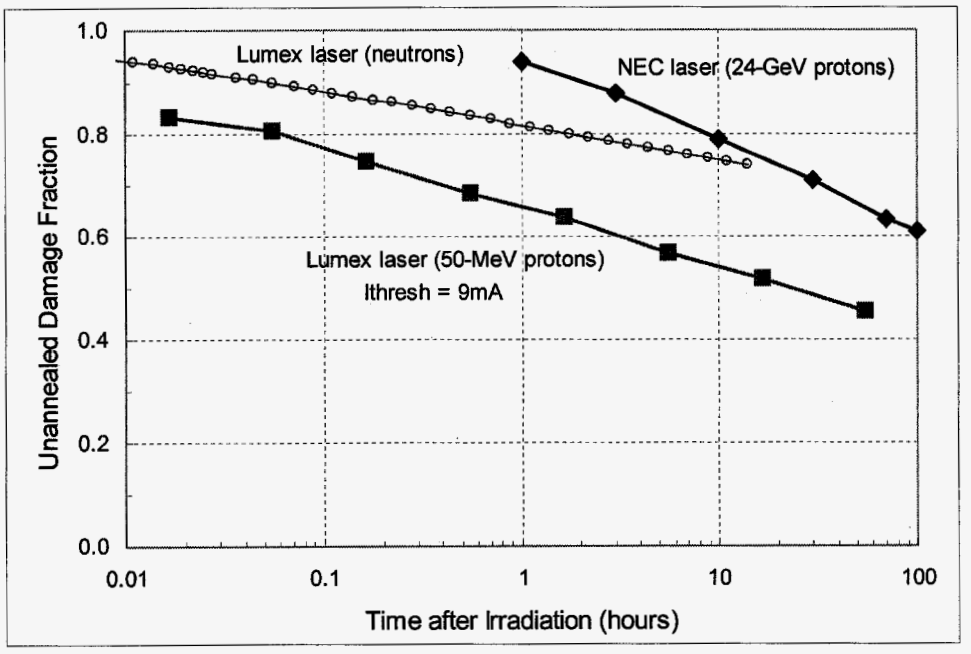

Fig.40. Annealing of laser diodes after irradiation with neutrons and protons. The annealing proceeds more rapidly after irradiation with 50-MeVprotons. Results for a different laser of the same basic type irradiated with 24-GeV protons are also shown in the figure.

V. An Introduction to Optical Detectors

A. Detector Principles

In this section of the short course we will consider detectors formed by conventional p-n or p-i-n regions that respond to light by absorbing a photon, creating electron-hole pairs. Other types of detectors, including highly doped extrinsic detectors, are discussed in another section of the NSREC-04 short course.

Silicon is widely used as a detector for wavelengths between 0.4 and 1 μm. The responsivity of a silicon detector is shown in Fig. 41. At short wavelengths the responsivity is low because nearly all of the light is absorbed near the surface, and the energy of the photons is much greater than the bandgap energy. The excess energy when each photon is absorbed is dissipated as heat, not photocurrent. As the wavelength increases, the photon energy is closer to the bandgap energy, increasing the overall efficiency for electron-hole generation. The responsivity at long wavelengths falls to zero when the photon energy falls below the bandgap energy. The thickness of the detector must be greater than the absorption depth. IR-enhanced detectors have increased thickness to maintain responsivity at longer wavelengths, as shown in the figure.

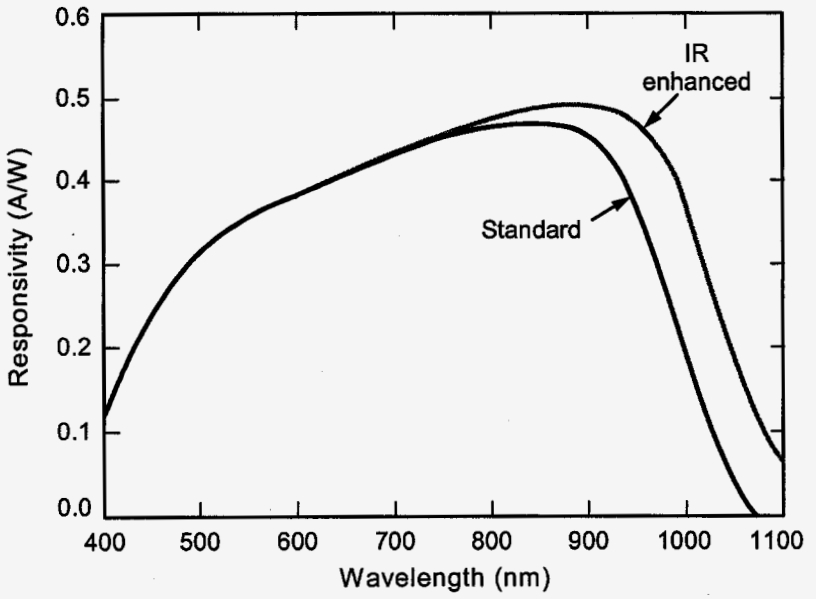

Fig. 41. Responsivity of a conventional silicon detector, optimized for responsivity at approximately 850 nm, and a detector with extended thickness that has a higher responsivity at longer wavelengths.

Conventional detectors consist of a p-n junction that can detect the excess carriers produced by optical absorption. Detectors can be designed to operate in various ways. The two most common are photovoltaic and photoconductive.

Photovoltaic. When the photodetector is unbiased, the excess carriers produce a voltage across the region. This self-generated voltage can provide current to a low-resistance load. This is the process that takes place in solar cells. Because the structure is unbiased, much of the current is collected by diffusion, resulting in relatively long collection times.

Photoconductive. The photoconductive mode is widely used, biasing the detector to provide an extended depletion width. Photo-generated carriers that are created within the depletion width are rapidly collected. Carriers that are generated beyond the depletion width boundary are collected by diffusion, a much slower process. The diffusion length, L, is related to minority carrier lifetime by the equation

$$L = \sqrt{D\tau} \tag{12}$$

where D is the diffusion constant, and τ is the minority carrier lifetime.

A diagram of a p-n photodiode is shown in Fig. 42. It is similar to a conventional diode, but is designed so that that the depth for charge collection is consistent with absorption within the material over the wavelength range. This is typically about twice the "1/e" absorption depth (see Fig. 2). Thus, a photodiode that is designed to absorb light up to wavelengths as long as 900 nm will require an overall depth of about 60 μm. It is possible to extend the wavelength to about 1000 nm (near the silicon band edge) by designing a photodiode with a very deep collection depth, 200 μm or more.

Guard rings (p+) surround the top surface of the photodiode in order to avoid surface leakage. Although not shown on the figure, most photodiodes have an antireflection surface coating that reduces reflection losses at a specified wavelength.

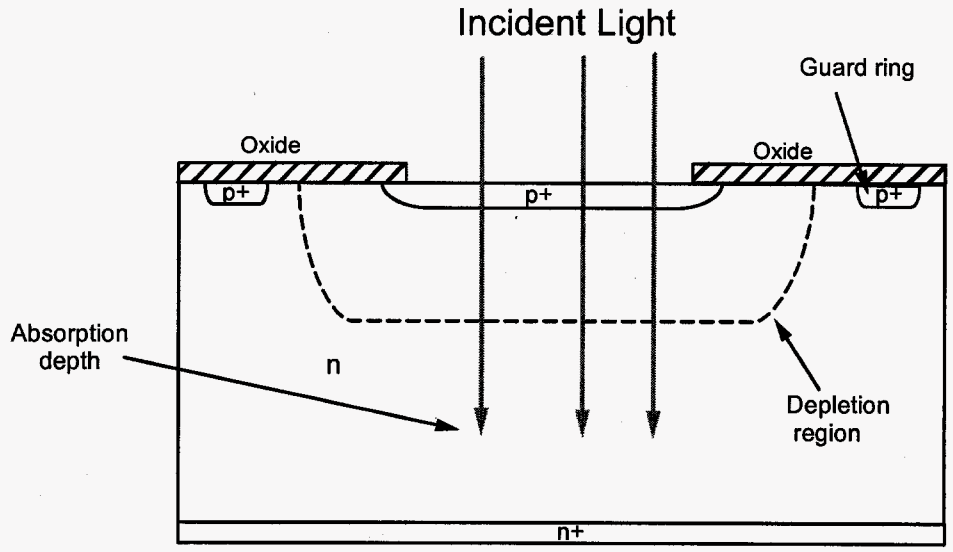

Fig. 42. Diagram of a typical photodiode.

p-i-n Photodiodes

By reducing the doping level, it is possible to fabricate a photodiode with much the same structure as a basic photodiode operating in the photoconductive mode, but with much faster response time. The lightly doped region allows the depletion width to extend completely through the lightly doped region to the underlying n+ contact, provided that the applied reverse voltage is sufficiently high. This extends the depletion region, allowing all of the carriers to be collected by drift, eliminating the slow diffusion component from the carrier collection process. This type of detector can be made from compound semiconductors, as well as silicon.

A diagram of an InGaAs p-i-n detector is shown Fig. 43. It is sensitive to wavelengths between 0.9 and 1.6 μm because of the narrower bandgap. In this example, light is collected from the back instead of the top surface. The detector is fabricated on an InP substrate, which is transparent to light in the wavelength range of interest. Light is absorbed in the InGaAs layer, which can be made quite thin [Liu92] – on the order of 3 μm – because the absorption coefficient is much higher and relatively flat over this range of wavelengths compared to an indirect semiconductor (see Fig. 2). A p-i-n detector fabricated in silicon would typically have a much thicker light-absorbing layer because the absorption coefficient is smaller, and varies much more with wavelength (and would only be useful out to a maximum wavelength of 1100 nm). The construction of a silicon p-i-n detector is similar to that of the conventional silicon detector in Fig.42, but with lower doping in the depletion region.

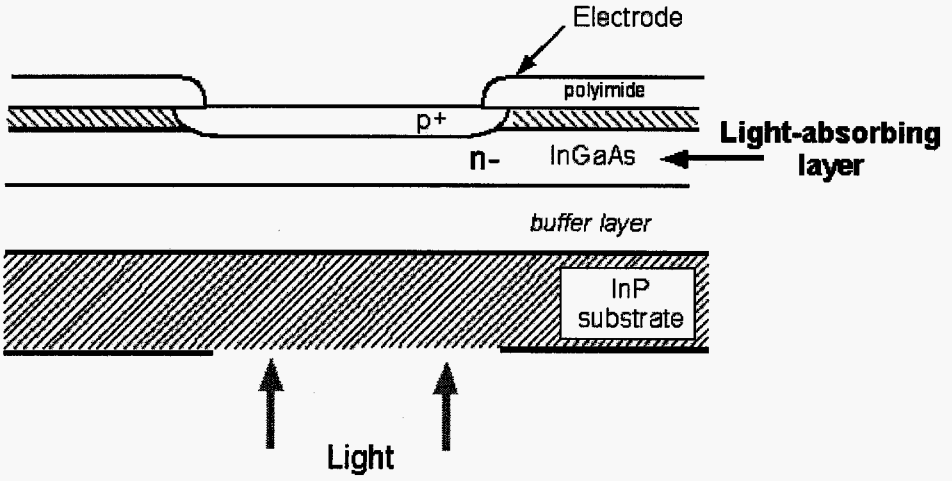

Fig. 43. Diagram of an InGaAs p-i-n photodiode intended for wavelengths between 0.9 and 1.6 μm.

One drawback of p-i-n diodes is that they have much higher dark current compared to conventional photodiodes. However, InGaAs devices have relatively thin layers, reducing the dark current compared to silicon or germanium detectors. The dark current has two components, one from surface recombination, and the other from generation-recombination centers in the bulk region where the device is fully depleted. Dark current depends on temperature, doubling approximately every 10 °C.

Avalanche Photodiodes

Avalanche photodiodes (APDs) rely on avalanche multiplication to increase the number of electron hole pairs produced by the interaction of a single photon within the structure. Fig. 44 shows a diagram of a silicon avalanche photodiode that is intended for applications with wavelengths up to 900 nm (the absorption depth is about 8 μm at that wavelength). The APD has two distinct regions: a lightly doped drift region which collects carriers from the incident photons where the electric field is relatively low, and a high-field avalanche region below the surface. The basic concept is that minority carriers (in this case electrons, because the multiplication factor for electrons is much higher for electrons) produced by photons in the drift region will be collected in the avalanche region where the high field will cause additional carriers to be produced. The device is biased so that the lightly doped region is depleted, causing the depletion region to extend to the boundary of the avalanche region. Avalanche photodiodes typically have very lightly doped drift regions, as shown in the figure. The avalanche process is temperature sensitive, usually requiring local temperature control of the APD. The APD in Fig. 40 is only intended for wavelengths below 900 nm because the drift region only extends 25 μm below the top surface. Special "IR-enhanced" ADPs are available where the drift region extends to 200 μm. However, those devices have larger dark current because the total volume of the diode is so much higher.

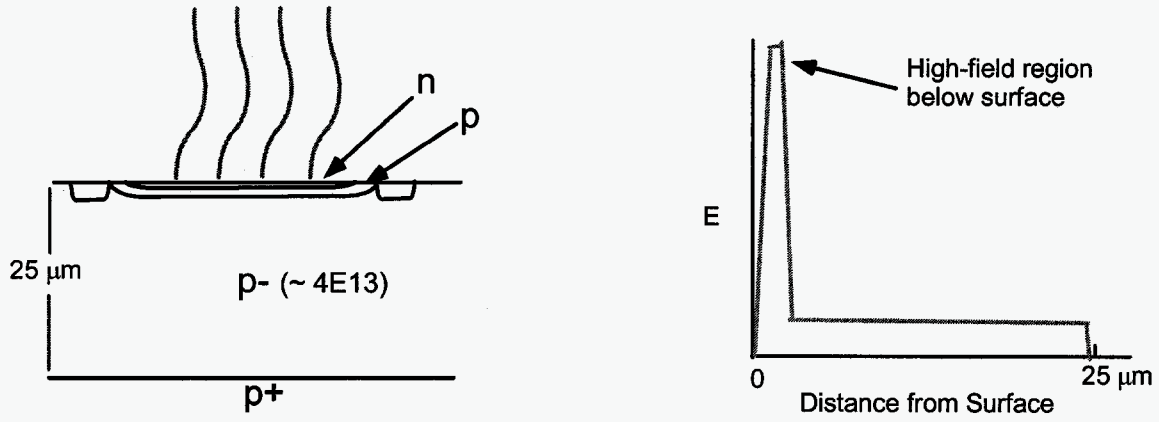

Fig.44. Diagram of a silicon avalanche photodetector.

B. Radiation Damage

Radiation affects detectors in several ways, as listed below.

- Ionizing radiation may increase surface recombination because of traps that occur at the interface between the detector surface and the passivation region. Guard rings are usually used at the edge of the detector, which decrease sensitivity to surface recombination
- Minority carrier lifetime will decrease, reducing the diffusion length for photo-generated carriers within the detector.
- Bulk damage will increase dark current. This mechanism is particularly important for avalanche photodiodes because the dark current from bulk recombination centers will be multiplied by the avalanche multiplication factor of the APD.
- Bulk and surface damage will increase noise in the detector. Although noise is only important for detectors used to detect low light levels, it is an important degradation mechanism.

Fig. 45 shows how the photoresponse of a conventional silicon detector is affected by high-energy protons. Light at shorter wavelengths almost entirely absorbed within the drift region, where it is only slightly affected by lifetime damage. This is the reason that only slight changes occur in the responsivity at 650 nm. However, most of the light at longer wavelengths is absorbed beyond the drift region and relies on diffusion in order to be collected. This causes the photoresponse to degrade more severely at longer wavelengths. A p-i n detector would show nearly the same degradation at all wavelengths, because all of the charge is collected through drift, not diffusion. However, dark current in a p-i-n detector would increase by several orders of magnitude at the maximum fluence levels shown in the figure.

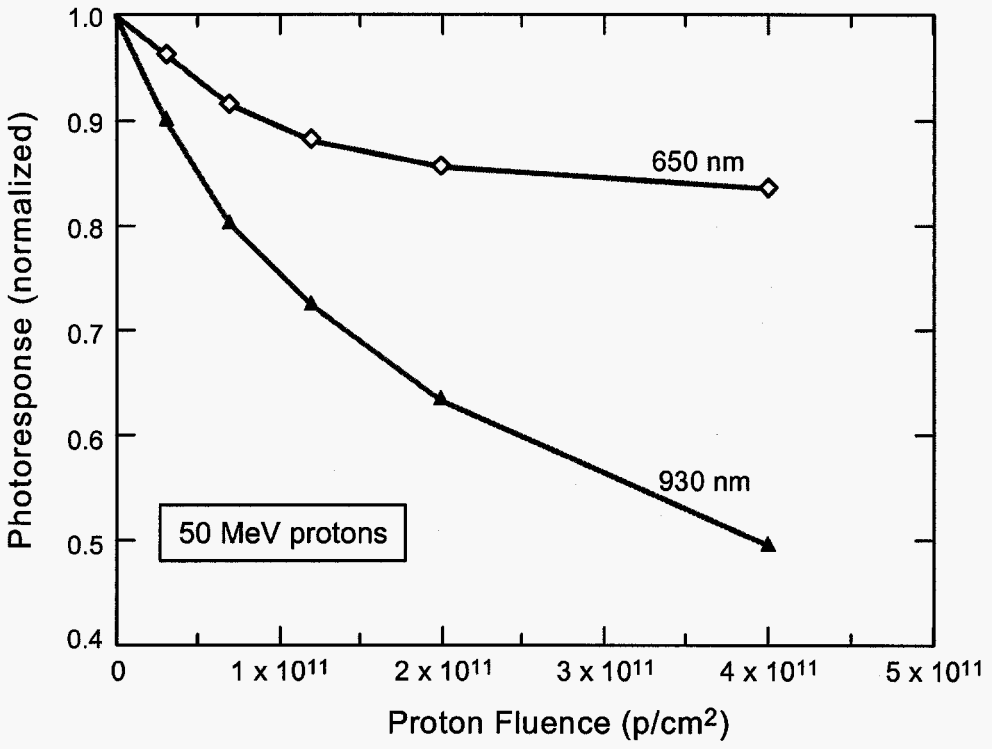

Fig. 45. Degradation of a conventional photodiode at two different wavelengths.

Radiation damage in avalanche photodiodes is more complicated because the avalanche gain amplifies radiation-induced dark current from the bulk region, but has no effect on surface current [Swan87]. Figure 46 shows how dark current in a silicon avalanche photodiode is affected by gamma and proton irradiation [Beck03]. Although we often assume that ionization damage is the dominant mechanism for this type of component, displacement damage is actually the dominant process (except at high radiation levels). In this case damage at total dose levels below 20 krad(Si) when the device is irradiated with gamma rays is actually due to displacement damage. The Compton electrons that are produced by the cobalt-60 gamma rays have an average energy of about 500 keV, which are about 250 times less effective in producing displacement damage than the 51-MeV protons, but nevertheless still introduce displacement effects.

At higher total dose levels some of the APDs became sensitive to ionization damage, resulting in strongly nonlinear behavior for some of the samples. The total dose where this occurred was about the same for both protons and gamma rays. Thus, damage in these detectors appears to be a superposition of displacement damage and ionization damage.

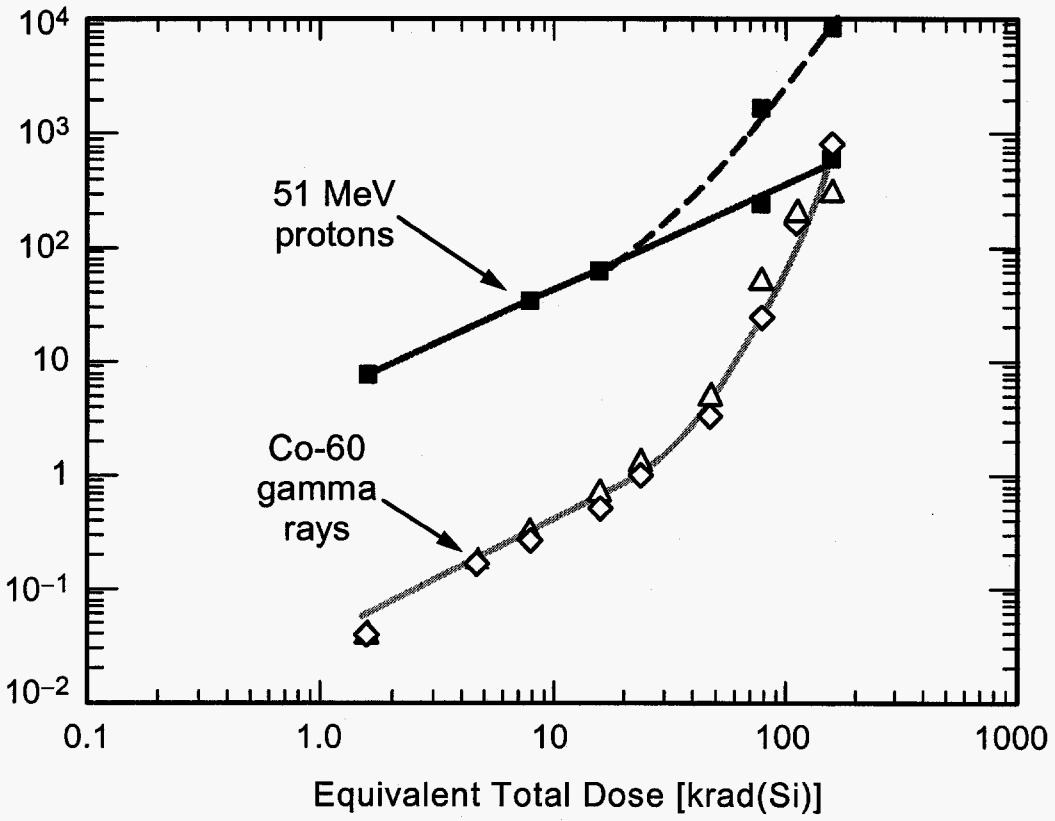

Fig. 46. Degradation of a silicon avalanche photodiode after irradiation with protons or cobalt-60 gamma rays (equivalent total dose values are shown). Some samples exhibited large increases at higher levels, consistent with surface damage.

Degradation of Internal Monitor Diodes Used in Laser Diodes

Another important class of diodes are the monitor diodes that are frequently incorporated within laser diode assemblies. These are usually discrete diodes, but it is also possible to fabricate integrated monitor diodes [Diec01]. Fig. 47 shows a typical diode assembly where the monitor photodiode measures light irradiated from the back facet.

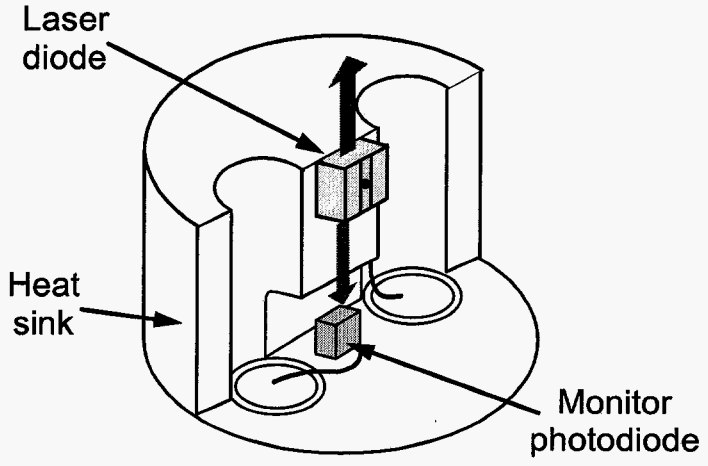

Fig. 47. Mechanical configuration of a monitor diode that measures light from the back facet of an edge-emitting laser.

Fig. 48 compares degradation in the photoresponse of monitor diodes from two different types of laser diodes with the photoresponse degradation of a silicon detector [John01]. In both cases there is much less degradation in the monitor diodes compared to silicon. However, the monitor diodes degrade more rapidly than the threshold current of the laser diodes that they are measuring, and may be the limiting factor in applying these laser diodes in system applications. Thus, it is essential to evaluate monitor diodes when radiation tests of laser diodes are done. Note that little or no annealing will take place in the photodiodes, unlike the threshold current of laser diodes, which anneals rapidly during extended operation, increasing the importance of monitor diode degradation in most applications.

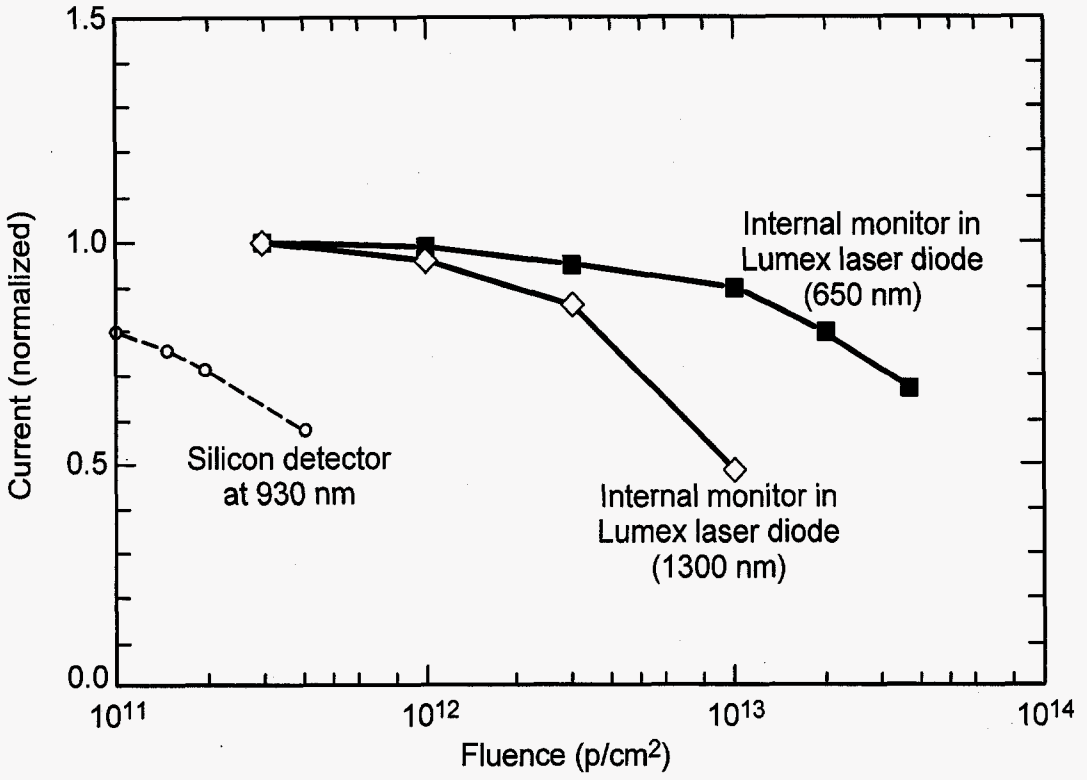

Fig. 48. Degradation of internal monitor diodes within laser diode assemblies. They are compared with the degradation of a silicon detector.

VI. Optical Fibers

A. Propagation

Optical fibers are designed to confine light within a central region of a fiber. A basic optical fiber consists of a core (which may be uniform or doped with impurities) surrounded by a cladding layer with lower refractive index than the core. The difference in the refractive indices of the core and cladding are key parameters, along with the diameter of the core. Figure 49 shows a diagram of a basic optical fiber.

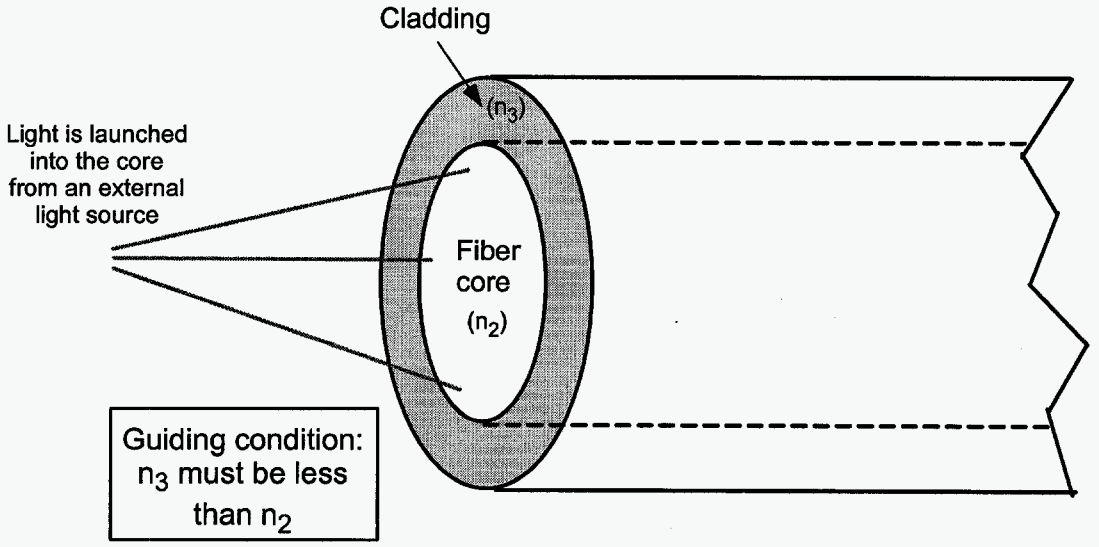

Fig. 49. Basic diagram of a step-index optical fiber with index of refraction n_2 in the fiber core, n_3 in the cladding, and n_1 in the medium between the light source and the fiber front surface.

Light that is incident on the fiber will enter the core. Light that enters the core at an angle will be refracted, eventually reaching the cladding. Light that strikes the cladding at angles greater than the Brewster angle will undergo total internal reflection, with very low loss. However, if the angle between the light ray and the cladding is less than the Brewster angle it will enter the cladding, and cannot propagate down the fiber. Thus, light that enters the fiber beyond a critical acceptance angle will be lost in the cladding. The numerical aperture (N.A.) determines the maximum acceptance angle of the fiber. It depends on the refractive index of the fiber as well as on the refractive index of the medium between the optical source and fiber, as described by the equation:

$$\text{N.A.} = \sin\theta_i = \sqrt{n_2^2 - n_3^2} \qquad (13)$$

The N.A. defines the maximum acceptance angle, θ_i, for light incident at the core of the fiber, assuming that the medium between the fiber core and the light source has an index of refraction of one.

Although it is possible to use simple ray diagrams to understand the principles of optical fibers, light actually propagates through the fiber as an electromagnetic wave with various modes. Fibers with a relatively large core diameter (50 to 100 μm) will allow many different

electromagnetic modes to propagate down the fiber. By reducing the diameter, it is possible to fabricate fibers that can only support a single internal mode. A cutoff wavelength can be defined for single-mode fibers, defined by the equation

$$\lambda_c = \frac{2\pi(\text{N.A.})\,r}{J_1(0)} \tag{14}$$

where λ_c is the cutoff wavelength, r is the radius of the fiber, and $J_1(0)$ is the value of the Bessel function J_1 with argument equal to zero (numerically ≈ 2.405). If the wavelength λ is $> \lambda_c$ then the fiber will be in single mode, whereas if λ is $< \lambda_c$ then the fiber will be capable of multimode propagation. We can estimate the fiber diameter for an example where the refractive indices are 1.46 and 1.45. The numerical aperture is then 0.171. Using the previous equation, the diameter of the fiber must be less than $2.405\,\lambda/(2\pi\,0.17)$ or 4.5 μm for a wavelength of 1.3 μm, a very small diameter compared to the diameter of multimode fibers.

It is possible to increase the fiber diameter for single-mode operation by reducing the difference between the refractive indices of the core and cladding, but the difference must be high enough to avoid difficulties with nonuniformity of either the cladding or core. Single-mode fibers typically have core diameters between 4 and 10 μm.

Dispersion

Two different mechanisms cause pulse-width broadening when an optical pulse is transmitted through an optical fiber. The first mechanism is caused by *chromatic dispersion* within the fiber material because the index of refraction depends on wavelength. It is important because of the finite spectral width of typical light sources (~ 7% for LEDs, and 0.5 to 2% for semiconductor lasers). Chromatic dispersion causes light at different wavelengths to travel at slightly different angles within the fiber, increasing the path length for light at longer wavelength. This will cause the pulse with to broaden. Chromatic dispersion is more important when an LED source is used because of the relatively broad bandwidth. It is possible to eliminate that contribution by using a wavelength near 1.3 nm, where chromatic dispersion in the fiber is nearly zero (a fortuitous property of silica). Fig. 50 shows how chromatic dispersion depends on wavelength for pure silica. Minimum dispersion occurs at about 1300 nm, the "second" optical fiber window.

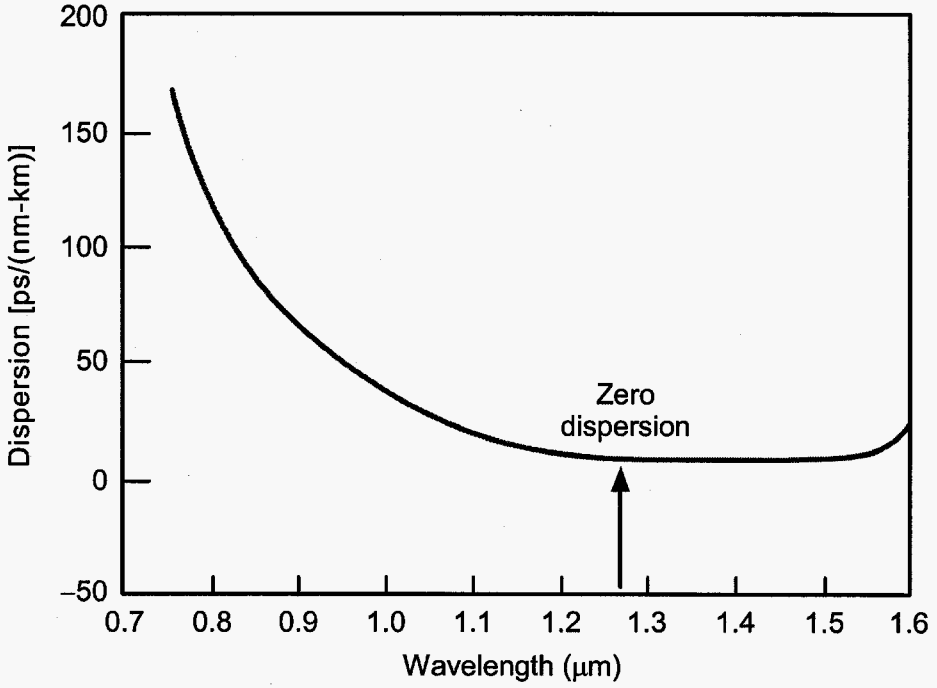

Fig. 50. Chromatic dispersion in pure silica. The dispersion is nearly zero for wavelengths near 1300 nm.

The other mechanism is *modal dispersion*. Fig. 51 shows why this occurs in a step-index fiber that supports several different modes. The optical path length is greater for light that enters the fiber at more extreme angles, delaying the arrival compared to light that enters at steeper incident angles. This causes the optical pulse to be stretched out, as shown in the diagram.

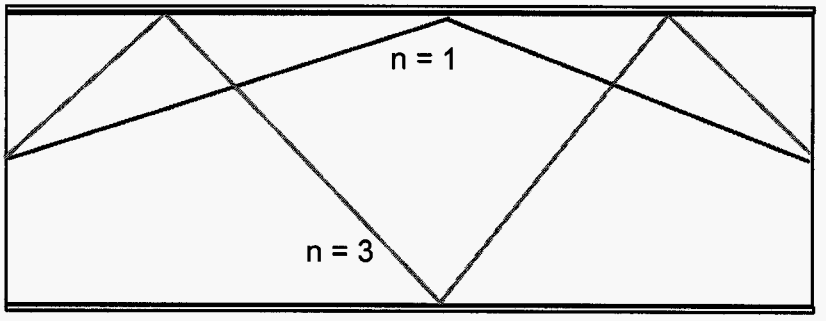

Fig. 51. Modal dispersion in a step-index optical fiber. More time is required for higher-order modes to be transmitted through the fiber.

A brief summary of several different types of optical fibers is given below:

1. Step-index fibers, which have a large diameter, uniformly doped core region, surrounded by a cladding with lower refractive index than the core. The core is usually pure silica. Those fibers can transmit several different modes, and have higher dispersion than other types of fibers. Typical fiber core diameters are 50 to 125 μm.

2. Graded-index fibers, which use graded doping to confine photons to the central region of the fiber. The graded doping decreases the index of refraction away from the center, decreasing modal dispersion because the propagation velocity depends on 1/n (n is the index of refraction). Typical core diameter is 50 μm. Germanium is commonly used to dope silica fiber cores in this type of fiber.

3. Single-mode fibers, which use very small fiber diameters. The small fiber diameter limits propagation to a single internal mode, eliminating modal dispersion. Single-mode fibers usually have core diameters between 5 and 10 μm (see Eq. 13). This increases the difficulty of coupling the fiber to the optical power source and detector.

4. Special-purpose fibers. One example is a *polarization-preserving* fiber. This type of fiber uses an asymmetric doping profile (for example an elliptical core) which has the property of retaining the polarization states of the initial light pattern, even over very long distances. Special fibers can also be made with special core materials for wavelengths > 1600 nm, where intrinsic losses from the bonds within silicon dioxide prevent the use of silica as a core material.

Other important properties of optical fibers include (a) losses from bending, which can alter the propagation properties of fibers that are wound in tight spirals; (b) the possibility of launching unstable modes either within the fiber core or within the cladding unless special *mode scramblers* are used that provide a launch pattern that is equivalent to the optical modes in a long fiber; (c) alteration of fiber properties through stress, which may require careful treatment and winding of fibers on spools; and (d) the practical difficulties of providing stable, known optical power levels, taking Fresnel reflection and mechanical stability into account. Mechanical instability may affect light coupling at either the entrance or exit of a length of optical fiber during radiation testing. All of those factors are important when optical fibers are subjected to radiation testing, as discussed in the next section.

B. Radiation Damage in Optical Fibers

The primary mechanism involved in radiation damage in optical fibers is formation of color centers within the core (typically silica, although other core materials can be used, including plastic). The presence of impurities increases the rate of color center formation. For pure silica cores, the induced absorption is relatively low, and is strongly temperature dependent.

Fibers doped with germanium have relatively low absorption when they are irradiated at low dose rate, but exhibit high absorption losses when they are exposed at high dose rate. The induced loss anneals relatively quickly. Fibers with undoped silica cores do not exhibit this effect.

Radiation testing of optical fibers is typically done by exposing a coil of fiber within a radiation source, which can be steady-state (typically a cobalt-60 isotope source), or pulsed (a flash X-ray). There are a number of important details. Stress in the fiber or microbending losses (from short radius coils) can affect the results. A mode scrambler must be used at the input of the fiber. This eliminates "cladding modes" which allow some of the light to travel in the cladding region if the mode scrambler is not used. The optical power launched into the fiber must be accurately known, and low enough to avoid distorting the results because of photobleaching. The diagram in Fig. 52 shows a typical example of an optical fiber test. A lock-in amplifier, synchronized to the pulse generator that drives the LED, is used to measure the optical output from the detector and low-noise amplifier. It is usually assumed that the attenuation depends on fiber length. This is generally valid, but the induced absorption will begin to saturate at high total dose levels. Many experimental details are important, particularly the method used to launch light to the fiber and optical power level. Fiber losses are usually reported in units of dB/km. Losses in most fibers are relatively low, requiring fiber lengths of 50 m or more in order to characterize radiation-induced loss with sufficient accuracy.

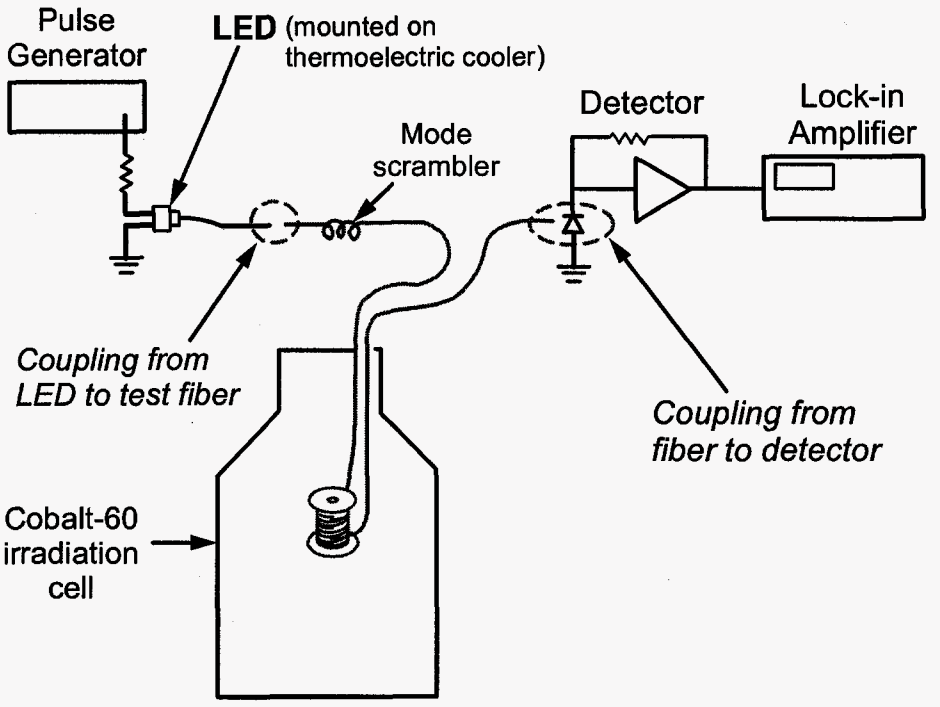

Fig. 52. Diagram of a radiation test of an optical fiber. A spool of the test fiber is placed within the radiation source and monitored with external equipment.

An example of the results of a radiation test of an optical fiber is shown in Fig. 53. In this example the tests were done using an LED with a wavelength of 850 nm. The LED was mounted on a temperature-controlled plate to maintain optical power stability (recall that the output of an LED is very sensitive to temperature). It was driven by a pulse generator, which was synchronized with a lock-in amplifier at the detector. The fiber, a multimode step index fiber with a pure silica core, was cooled within the irradiation cell to a temperature of –55 ° C because of concern about fiber degradation at low temperature. Note that the induced absorption would be much lower if the tests were done at room temperature.

Several different curves are shown. In each case the fiber was irradiated to a total dose of 10 krad(Si). However, the optical power coupled to the fiber was different for each case. A new section of fiber was used each time that the experiment was repeated. At high optical power levels the absorption increased to approximately 30 dB/km during the irradiation, saturating at about 3 krad(Si). The fiber gradually recovered after irradiation, with nearly complete recovery several hours after the irradiation was stopped.

When the optical power level was reduced to low levels, the induced absorption in the fiber was about one order of magnitude greater than the results for the fiber sections that was tested with high optical power levels. At low optical power, the damage does not show any sign of saturation, unlike the results when the tests were done with high optical power. The reason for the lower absorption loss with high power is that when tests are done at high optical power the high density of photons causes some of the color centers within the fiber to anneal. This is called *photobleaching*.

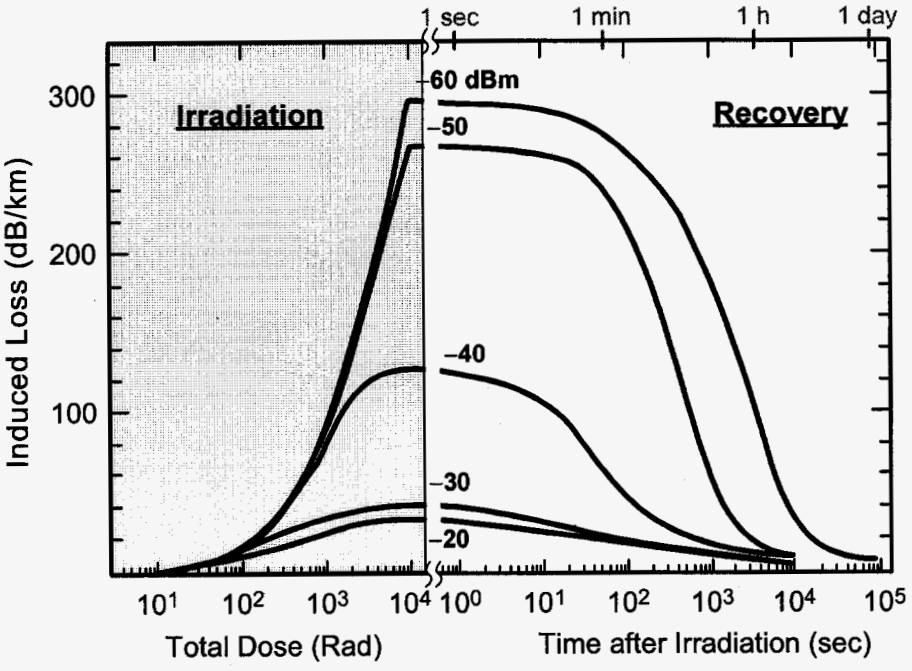

Fig. 53. Absorption and recovery of an optical fiber, irradiated at –55 ° C in a cobalt-60 radiation source.

Substantial work has been done to compare test results from various laboratories under a NATO-sponsored committee [Frieb88, Tay901, Tay902]. Important results from the series of tests done by that committee include an investigation of the different variables that affect fiber radiation response, as well as the development of standard radiation test methods to improve the validity of test results by different laboratories. The study used three types of fibers: (1) silica-core multimode fibers; (2) silica-core single-mode fibers; and (3) germanium-doped graded-index fibers. Two different wavelengths were used, 850 and 1300 nm. The first attempt at inter-laboratory comparison revealed several experimental problems that caused substantial differences in the results.

The following steps were taken to improve results in the second experimental study:

- The input optical power was standardized at 1 μW
- A mode-scrambler was used in tests of the multi-mode fibers
- Mode-stripping was used to eliminate higher-order modes within the cladding
- Fibers from a single perform were distributed to the participating laboratories

Table 5 summarizes some results from the second study. Several points should be noted. First, the results were reasonably consistent, even though each laboratory had the freedom to implement the tests with their own equipment and procedures. The coefficient of variation (*the coefficient of variation is the standard deviation divided by the mean value*) was between 0.12 and 0.21 when we compare results from the different laboratories ***for all of the fiber types***. Second, the induced loss in the single-mode fiber was extremely high at a wavelength of 850 nm, but in line with the results from the other types of fibers when it was measured at 1300 nm. The reason for this difference is transient absorption, a characteristic of germanium-doped fibers that causes far more absorption to occur at short times after a pulse of radiation. Fibers with pure silica cores do not exhibit this effect.

Table 5. Steady-State Results for Optical Fibers from the NATO Study

Fiber Manufacturer	Type	Wavelength [nm]	Number of Participating Laboratories	Loss [dB /km]	Coeff. of Variation of Loss
A	Multimode silica core	850	4	4.34	0.12
C	Ge-doped graded index core	1300	4	2.76	0.20
G	Single-mode silica core	850	3	**17.5**	0.16
H	Single-mode silica core	1300	4	2.7	0.13

An additional series of tests was done to evaluate absorption and recovery at short times for Fiber G, a germanium-doped single-mode fiber. This type of fiber has high transient absorption losses that recover rapidly after irradiation. The results of those tests are shown in Fig. 54 [Tay901]. Four different laboratories compared test results for samples of fiber that were obtained from the same preform. The dose rate used for testing was restricted within a narrow range. There is reasonable agreement, although one laboratory measured significantly higher losses, even after the annealing period following the pulsed irradiation. However, pulsed measurements are far more difficult than the steady-state results shown in the previous figure.

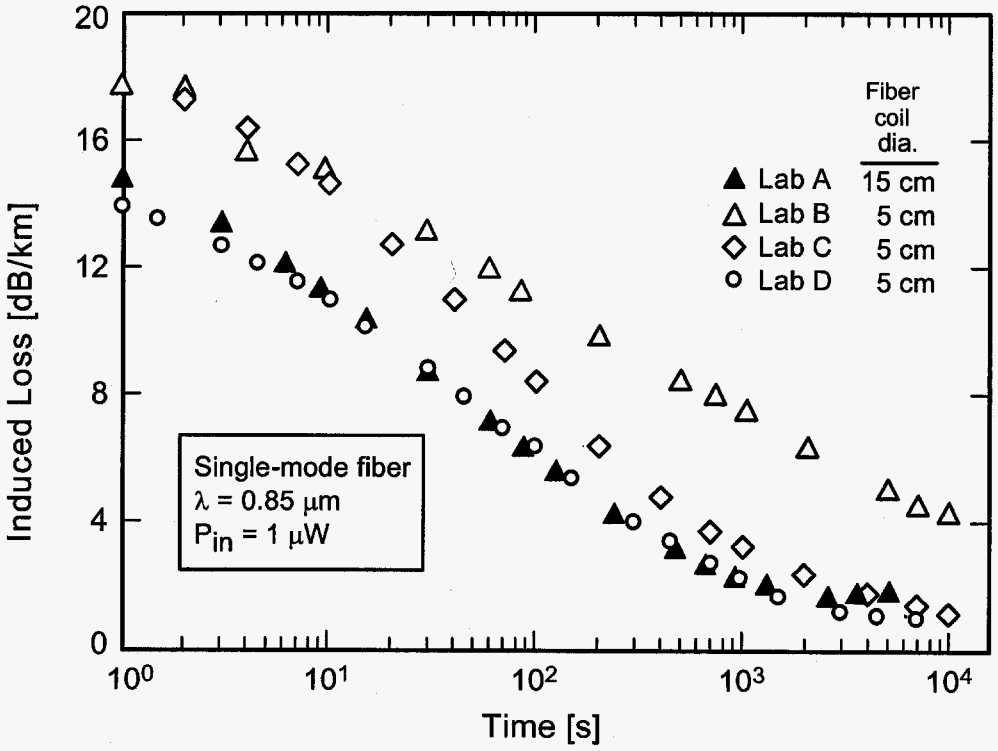

Fig. 54. Comparisons of short-time tests of absorption in a single-mode fiber by four different laboratories.

Recent work on radiation effects in optical fibers has included tests of special types of optical fibers, such as polarization-maintaining optical fibers. The core of those fibers are doped with germanium, along with asymmetrical distributions of co-dopants (phosphorus and boron) that produce internal stress within the fiber. Polarization-preserving fibers exhibit far higher losses compared to more conventional types of fibers, as shown in recent test results in Fig. 55 [Gira03]. This figure compares two different types of polarization-preserving fibers along with single-mode fibers made with the same dopant. The polarization-preserving fibers have a strong asymmetry in the doping concentration. The results show very similar transient absorption and recovery for single-mode and polarization-preserving fibers. Although not shown in the figure, the study also examined the polarization properties of the fibers before and after irradiation. There was little change, showing that these fibers can be used in radiation environments while maintaining their polarization properties.

The ordinate shows the optical attenuation per krad, assuming a linear dependence. The damage is linear with prompt dose up to approximately 50 krad(SiO_2), but becomes sublinear at higher doses.

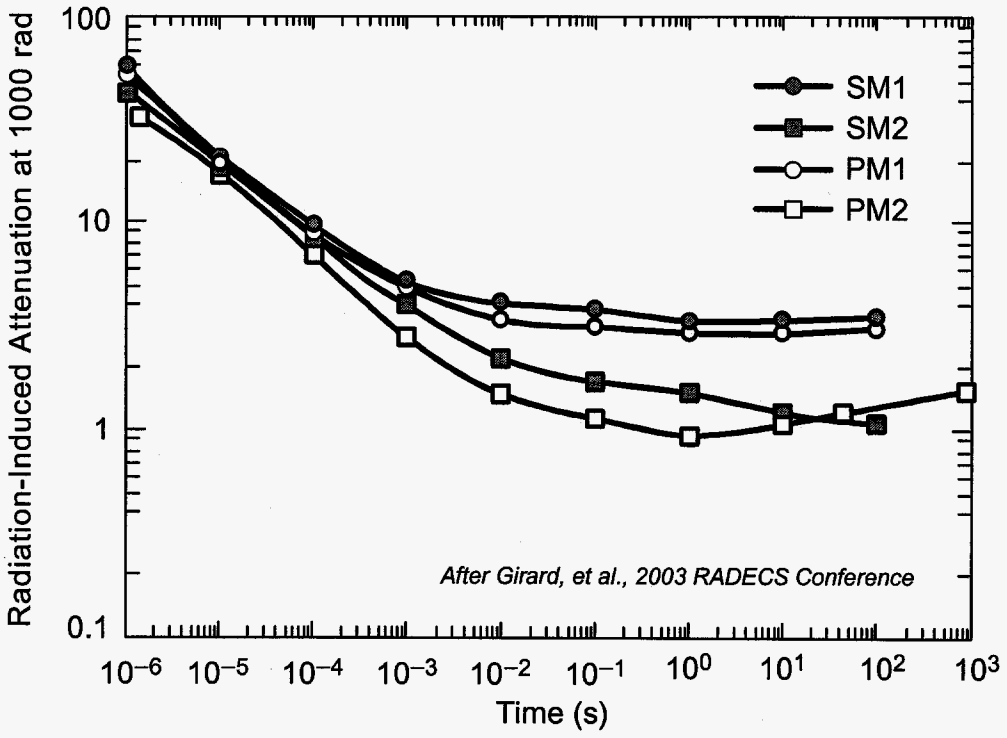

Fig. 55. Induced loss in a polarization-preserving fiber.

VII. Optical Subsystems

A. Digital Optocouplers

1. Operating Principles

Optocouplers are an example of a fundamental type of optical system where we do not have the sophistication of an advanced encoding scheme and special low-noise receiver. An example of a basic single-transistor optocoupler is shown in Fig. 56. An external signal is applied to the LED, and light from the LED is transmitted to the collector of the phototransistor. Light from the LED is absorbed in the collector region, producing a photocurrent in the transistor that can then be used to generate active signals in a separate path that is electrically isolated from the electrical path used to activate the LED.

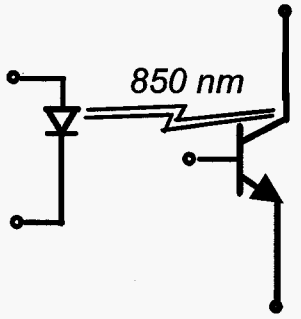

Fig. 56. Diagram of a basic optocoupler with a single phototransistor.

The energy efficiency for this process of first converting electrical energy to light, and then back to electrical energy is typically less than 1% mainly because of the difficulties of extracting light from the LED. (The quantum efficiency for conversion within the LED is approximately 60%, but typically only a small fraction of the LED output can be coupled to the phototransistor). Optocouplers with single transistors like that shown in Fig. 57 have limited bandwidth – typically $\approx$ 1 MHz - because the optical collection process within the phototransistor involves diffusion, along with the practical difficulty of using a single transistor in a circuit with high bandwidth.

The fundamental parameter used to characterize optocouplers is the current transfer ratio (CTR), which is the ratio of the collector current of the phototransistor to the forward current of the LED. It is analogous to transistor gain, but is much lower - typically 1 to 10 – because of the low energy transfer efficiency. There is a nearly linear relationship between LED current and output current for this type of optocoupler that depends on the transistor gain as well as the LED efficiency.

Higher bandwidth can be achieved by using a high-gain amplifier circuit in place of the simple phototransistor, with a digital output stage. The designs of these circuits are proprietary, and often include a Schmidt trigger to provide hysteresis. Optocouplers with internal amplifiers may have bandwidths of 50 MHz or more. A double-heterojunction LED is required in order to acheive such high speeds because of the long response time of amphoterically doped LEDs.

Unlike basic optocouplers, optocouplers with internal amplifiers have highly nonlinear transfer characteristics, as shown in Fig. 57. These types of optocouplers generally do not specify current transfer ratio because of the nonlinear relationship between LED current and output current. The electrical specifications usually define a guaranteed saturation value at the

output (V_{OL}) that is defined for a specific value of forward current in the LED. However, it is possible to make special measurements of the input current near the transition point for the amplifier, providing better information about the internal operating margin of this type of part. Those measurements are evident in the transfer characteristics shown in Fig. 57.

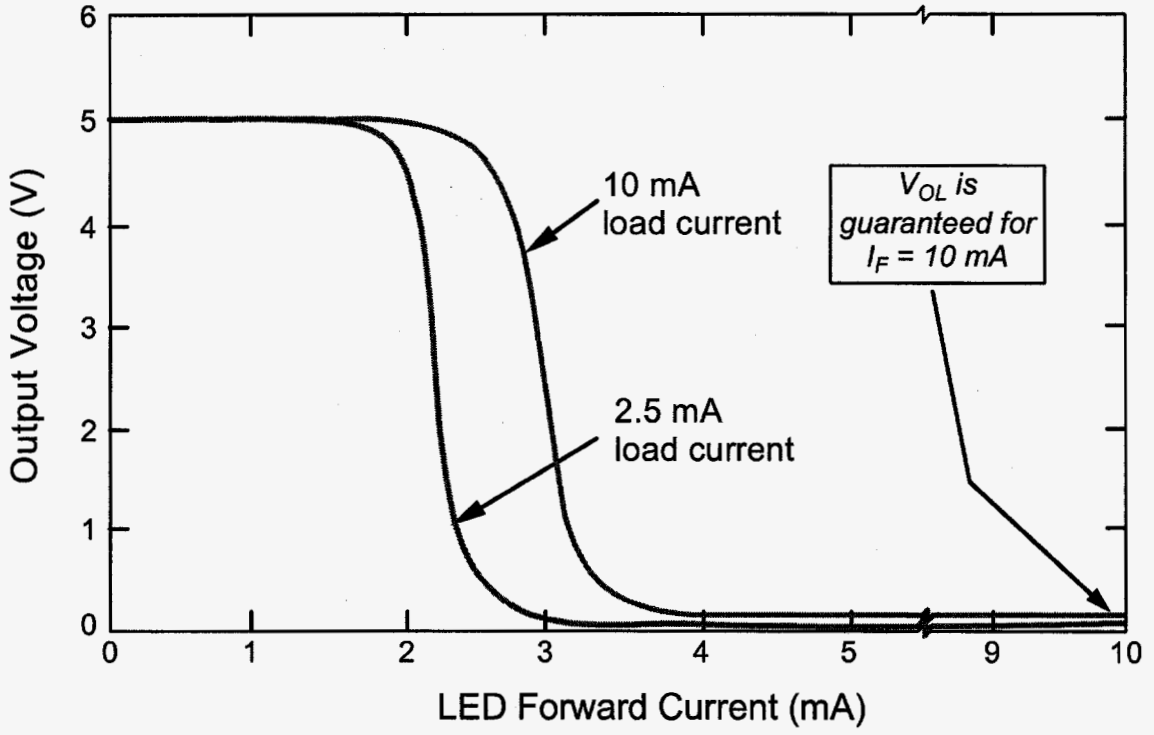

Fig. 57. Transfer characteristics of an optocoupler with an internal high-gain amplifier and digital output stage.

Table 6 lists some common types of optocouplers, including the input current, response time, and LED wavelength. In addition to permanent degradation of the LED and phototransistor or photodiode, we also have to be concerned about transients from heavy ions and protons for transistors with fast response times. However, transients are unimportant for simple phototransistor optocouplers such as the 4N49. The type of LED used within an optocoupler has a large impact on its sensitivity to displacement damage. Many optocoupler manufacturers do not specify the type of LED or the operating wavelength, and this is a major concern in selecting and qualifying optocouplers for space applications. If the type of LED is changed by the manufacturer, it may change the susceptibility of the optocoupler to displacement damage (see Fig. 30).

Table 6. Properties of Some Common Types of Optocouplers

Optocoupler Type	Circuitry	LED Wavelength	Input Current	Current Transfer Ratio	Response Time (ns)
4N49	Single transistor	870 nm	1 mA	2	
6N139	Darlington transistor	700 nm	0.5 mA	50	
6N134	High-speed amplifier	700 nm	10 mA	- - -	50 ns
5203	High-speed amplifier	850 nm	3 mA	- - -	20 ns

As long as a digital optocoupler is heavily overdriven, the effects of noise are minimized, provided the pulse width is compatible with bandwidth requirements. However, if we reduce the input current of the LED to the point where it is just able to function the output will be unstable, exhibiting noise characteristics that are similar to that of a high-gain optical receiver. Although this is not a mode that is allowed for normal optocouplers, degradation of the LED output within the optocoupler can result in conditions with marginal overdrive where the noise margin is very low.

2. Radiation Degradation

Optocouplers with amphoterically doped LEDs, such as the 4N49 optocoupler, are severely degraded by displacement damage. As shown in Fig. 58, the current transfer ratio falls to 0.4 - a factor of 2.5 reduction of the initial value - at a 50-MeV proton fluence of only 10^{10} p/cm^2. That is an extremely low fluence, corresponding to a total dose of about 1.6 krad(Si). Fluences of that magnitude can be produced by a single solar flare in space. Protons with lower energy will cause even higher degradation because NIEL increases with decreasing proton energy. Although we will not discuss electron displacement damage, displacement damage from electrons is also important for optocouplers that use this type of LED.

Separate measurements were made of the gain of the internal phototransistor during the proton tests, and those results are also shown in the figure. Generally, gain degradation is insignificant at the radiation levels where this type of LED degrades, showing how LED degradation dominates the radiation response. Although not shown in the figure, tests with cobalt-60 gamma rays cause the CTR to degrade by less than 20% at 50 krad(Si), underscoring the need to consider displacement damage effects for optocouplers.

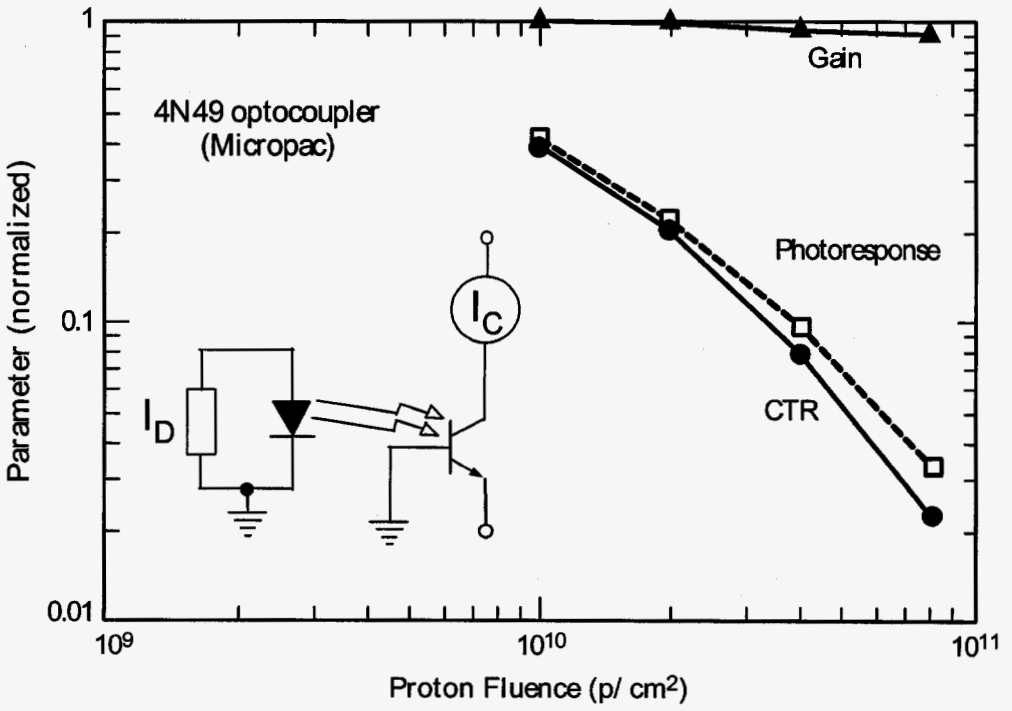

Fig. 59. Degradation of the current transfer ratio of the 4N49 optocoupler after irradiation with 50-MeV protons.

It is interesting to contrast the 4N49 with a more modern optocoupler, the 6N139. The minimum forward current of the 6N139 is 0.5 mA, only a factor of two below that of the 4N49. However, the 6N139 is far more resistant to radiation damage, as shown in Fig. 59 [Miya02]. The current transfer ratio is nearly unchanged at radiation levels where the 4N49 degrades severely. The 6N139 is about a factor of 50 more resistant to proton damage that the older 4N49. The main reason is the different LED technology, although more efficient optical coupling also plays a role. Another feature is evident in this figure. When we examine the effect of LED input current on CTR, we see that the peak CTR shifts to higher currents. The reason for this is the reduced light output from the LED, along with the current dependence of phototransistor gain. The CTR degrades more rapidly than one would expect from LED degradation alone because the lower light output of the LED "starves" the phototransistor, changing its operating mode to lower current where the effective gain is much lower.

Linear optocouplers are designed to take advantage of the current dependence of CTR on LED drive current, choosing an operating region that is well above the peak in the CTR-drive current relationship. This reduces the dependence of CTR on temperature (LED optical power decreases about 1% per degree Centigrade) and makes it possible to produce optocouplers with a narrow range of CTR. Radiation damage in these types of optocouplers is highly nonlinear, because small fluences shift the operating region to lower currents where the increased efficiency of the phototransistor compensates for the reduced light output of the LED. The degradation increases rapidly once the LED light output moves the operating region to the low-current side of the CTR-drive current relationship.

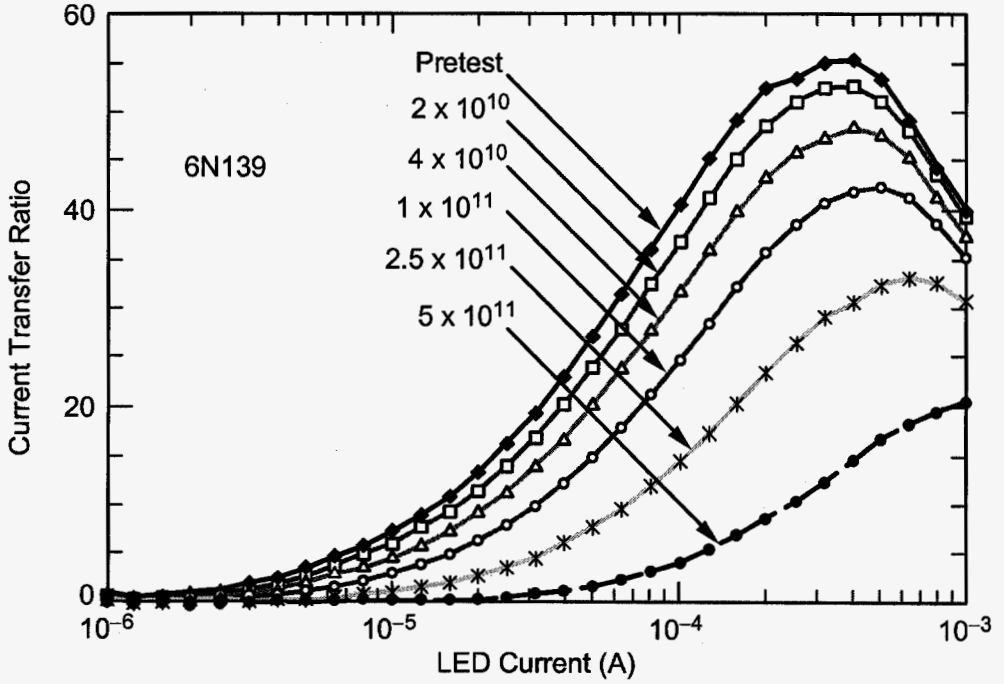

Fig. 59. Degradation of a more contemporary optocoupler with a double-heterojunction LED and far more efficient optical power coupling between the LED and phototransistor. The proton energy was 50 MeV [Miya02]

Additional work has been done by Germanicus, *et al.*, on degradation of optocouplers at several different proton energies [Germ02], assuming that damage in the LED is the dominant mechanism. They showed good agreement with NIEL values for energies from 21 to 100 MeV.

3. Transients from Protons and Heavy Ions

Low-speed optocouplers such as the 4N49 are essentially immune to transients from heavy ions or protons because of the slow response of the phototransistor. However, high-speed optocouplers such as the 6N134 are readily upset when they are exposed to heavy ions or protons. The input photodiode used in these devices has a circular geometry with a diameter of about 500 μm. This is far larger than the area of typical logic or analog devices that are sensitive to single-event upset effects. Consequently, direct ionization from protons – a phenomenon that is usually ruled out because the LET of protons is on the order of 10^{-2} MeV-cm^2/mg - plays a significant role in the response of these devices.

The earliest measurements of single-event upset effects considered upset from heavy ions. Those results showed that the threshold LET for upset was about 0.3 MeV-cm^2/mg, a low threshold LET, but not sufficiently low to be concerned about direct ionization from protons. Fig. 60 shows the cross section for upset from heavy ions in the 6N134 optocoupler. The cross section is significantly less than the area of the photodiode near threshold, and increases gradually as the LET increases. At first this is difficult to understand, because one would expect the cross section to quickly rise to the area of the photodiode. However, modeling results show that charge from ions striking the photodiode away from the center partially recombines before it can be collected. This is the reason for the gradual increase in cross section. Note that the cross section is greater than the diode area for LET values above 10 MeV-cm^2/mg. Two mechanisms are involved that contribute to the larger effective area: (1) charge deposited outside the diode area can be collected by diffusion, and (2) single-event transients in the amplifier. These mechanisms produce different pulse widths (amplifier transients produce transients with extended pulse width), allowing them to be distinguished from the basic nature of the output transient of the optocoupler.

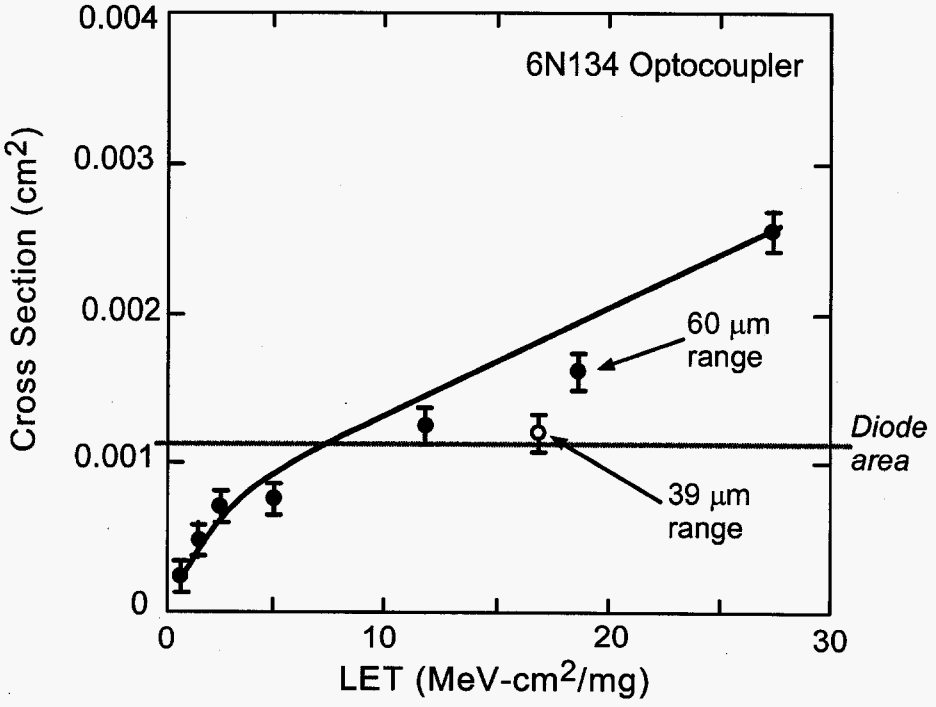

Fig. 60. Upset cross section of the 6N134 optocoupler from heavy ions.

The 6N134 optocoupler is also sensitive to upset from protons, which is not unexpected because of the very low threshold LET. However, when proton tests were done using incident angles above 80° the cross section was observed to increase by about a factor of six [LaBe97]. This result was difficult to explain, because one would normally assume that the cross section would approach the physical area of the diode. The relatively small increase in cross section along with the gradual nature of the change in cross section with angle seemed to rule out direct ionization from protons as the underlying mechanism. Furthermore, the effect of this increase on the upset rate was not very important because it required extreme angles before the cross section increased significantly.

A later study using protons with different energies showed that the cross section of the 6N134 increased by as much as three orders of magnitude when lower energy protons were used, as shown in Fig. 61 [John99]. The smooth increase in cross section with increasing angle of incidence was explained by a detailed model showing the effects of straggling on the charge collection, and that the angular dependence was due to the combined effects of direct ionization from the proton when it traveled through the large-diameter detector, and charge from the proton recoil when it interacted with a lattice atom before completely traversing the detector. Larger incident angles allow reactions with smaller amounts of recoil energy to cause the optocoupler to upset.

With lower energy protons, the cross section is much larger and begins to increase at lower incident angles. Calculations using the model developed for that effect showed that the expected error rate increased by a factor of about 4 in a typical earth orbit when the angular dependence was taken into account compared to the error rate calculated for a proton cross section that was independent of incident angle.

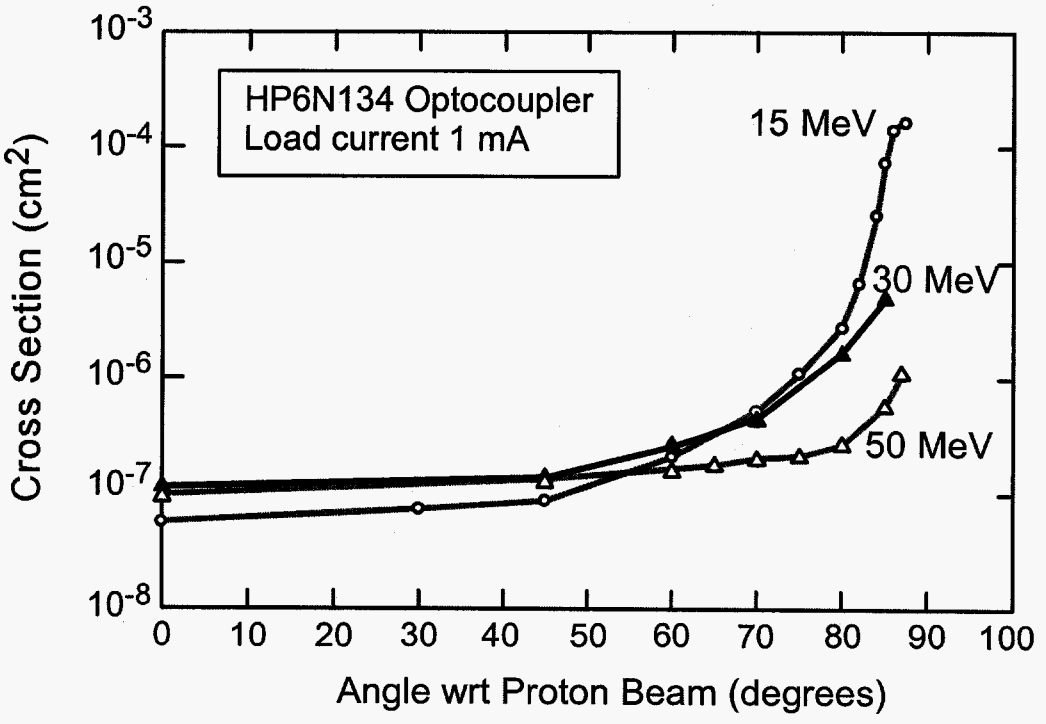

Fig. 61. Cross section for upsets in a 6N134 optocoupler for various incident angles during proton irradiation.

This example shows the extreme sensitivity of some types of optocouplers to transients from protons or ions with very low LET. The effect can be mitigated at the circuit level, provided that transients are taken into account during system design. However, system errors have occurred in some space system when the effect was not taken into account [LaBe97]. The large sensitivity to proton upsets increases its importance in earth-orbiting systems, even for low-altitude spacecraft because of the south Atlantic anomaly.

B. Optical Receivers

1. Operating Principles

The basic concept of an optical receiver is straightforward: an optical pulse is detected by an input amplifier and then used to generate pulses with a specific coding scheme. However, the presence of noise along with the detected pulse means that there is a finite probability for errors to occur during the detection process. The effect of noise is usually considered by means of a bit error rate, which is the fractional number of errors that occur in the receiver during a transmitted sequence of pulses. For acceptable performance, the bit error rate has to remain very low. For highly sensitive receivers, assuming a Gaussian distribution for noise, the noise and signal level are related as shown in the equation:

$$\mathrm{BER} = \frac{1}{2}\,\mathrm{erfc}\left[\frac{(\mathrm{SN})^{1/2}}{2\sqrt{2}}\right] \tag{15}$$

where BER is the bit error rate, SN is the signal-to-noise ratio, and erfc is the complementary error function. Fig. 62 shows how the bit error rate changes as the signal-to-noise ratio is reduced. When the SN drops below 20 dB, the bit error rate increases rapidly. A common specification for bit error rate is 10^{-9}, which requires a signal-to-noise ratio of 21.6 dB. We will use that criterion in discussing the performance of optical receivers.

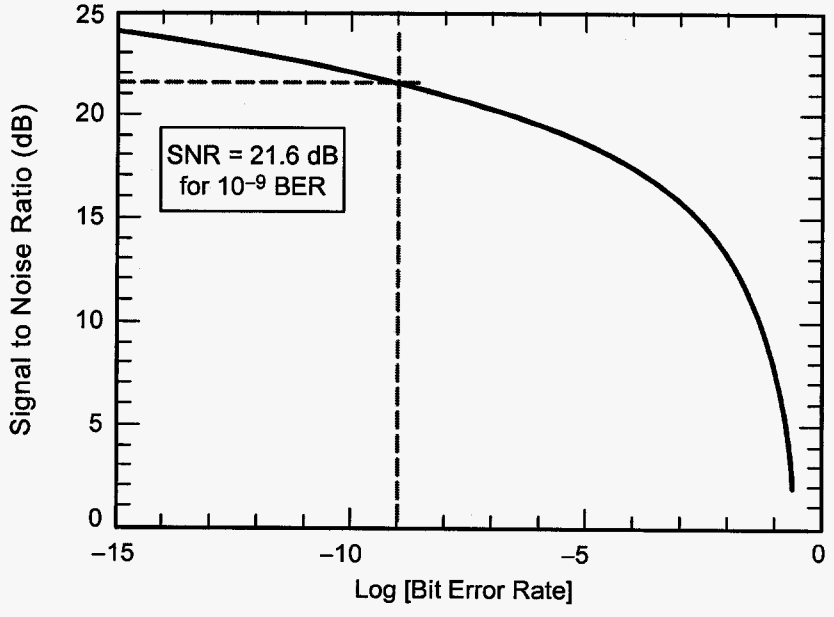

Fig. 62. Dependence of bit error rate on signal-to-noise ratio.

Special modulation techniques such as frequency shift keying, phase modulation, and coherent detection improve the theoretical limit for errors, but the improvements are relatively slight. Those methods are used in long-haul fiber optic systems (such as undersea cables), but are usually not required in systems used in space that use short cables, and generally have higher optical power margins.

Most optical receivers are designed to reject noise by means of several sophisticated circuit elements, integrating the signal during each clock cycle [Brai85]. Figure 63 shows this type of receiver, along with the two dominant noise sources, the detector and amplifier. A transimpedance amplifier is typically used that responds to the pulse of current through the detector, but keeps the voltage constant. Integrated receivers can be designed that reduce parasitic capacitance to improve performance at high data rates [Naka91].

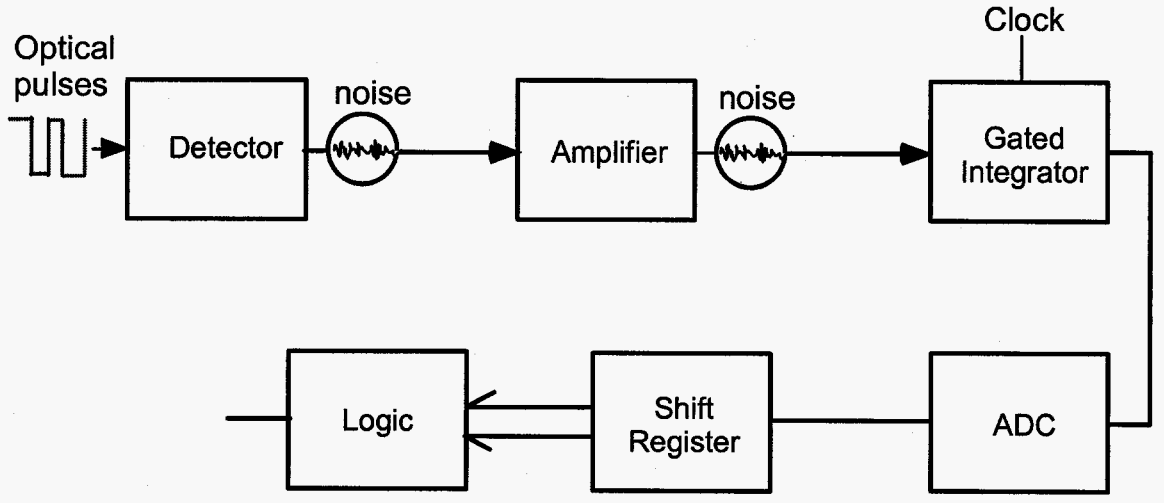

Fig. 63. Block diagram of an optical receiver where the optical signal is integrated during each bit period.

When optical receivers are near their detection limits, noise is clearly evident during each bit cycle. A standard way to examine this is by means of an *eye diagram*, which is the result of a continuous sampling of the signal over many bit periods. Fig. 64 shows an example. For high signal-to-noise ratios the bit pattern is very much like an ideal pulse train. As the signal-to-noise ratio is reduced, noise becomes evident during each pulse transition and the open regions between the upper and lower logic states "close" with a substantial amount of noise between levels (hence the term *eye diagram*).

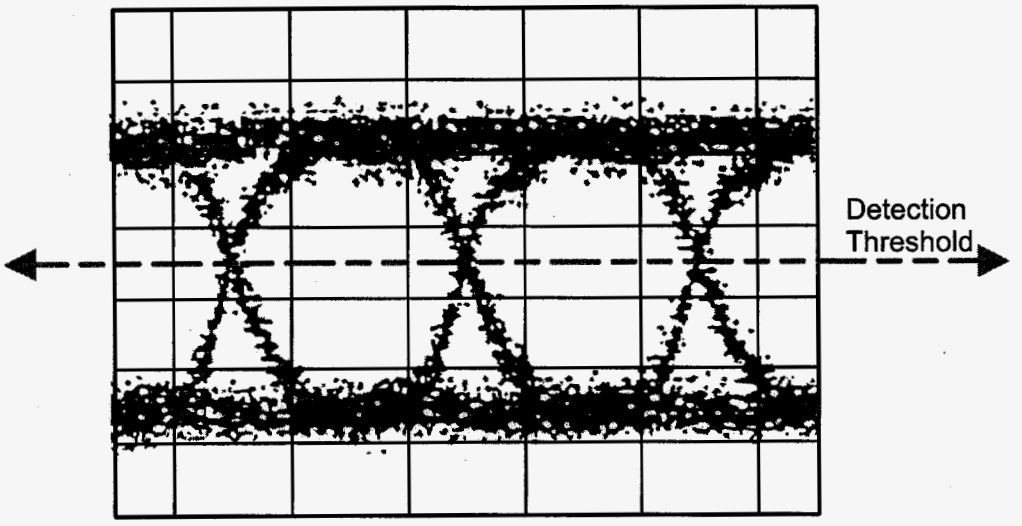

Fig.64. Eye diagram of a the pulses detected after the input amplifier of a sensitive optical receiver. The detection threshold is in the center of the mean pulse amplitude.

In order for an optical receiver to operate properly, the margin between the input optical power and the power detected by the receiver must be large enough to meet the bit rate requirement as well as to account for aging, fiber coupling losses, temperature, and other factors that may cause the internal margin to change over time. For example, the optical power output of LEDs and laser diodes decreases with time, particularly for components that are continually operated, gradually decreasing the BER.

We have seen that the signal-to-noise ratio must be on the order of 20 dB or more in order to meet typical bit error requirements. Fig. 65 shows how the link margin is related to the bit rate, the type of optical power source, and the type of detector. The link margin decreases with increasing bit rate because the integration period decreases as bit rate increases (there are fewer photons available during each pulse cycle). Thus, it is clearly more challenging to design receivers at high bit rates.

Several tradeoffs must be considered when designing an optical link. More optical power is available from lasers compared to LEDs, increasing the margin when a laser source is used, even though it is more difficult to use lasers because of the need for thermal control and closed-loop current drive circuits. Using an avalanche photodiode increases the margin in the receiver by about 6 dB, but adds more complexity. The overall system design must consider those factors, along with aging and wearout in these more advanced components. Recent work has demonstrated the feasibility of operating fiber optic links above 1-Gb/s using 890 nm LEDs [Akbu01], showing that it is possible to extend the bit-rate to very high frequencies without using laser diodes.

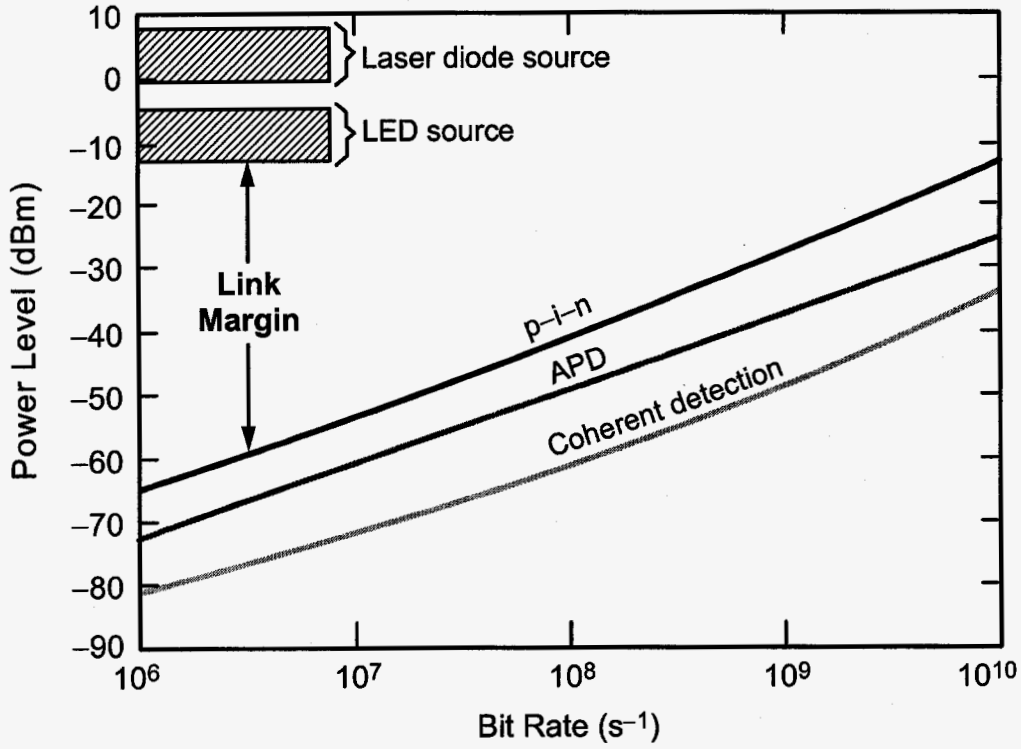

Fig. 65. Link margin for optical receivers. Note the decrease in link margin as the bit rate increases.

Optical power and receiver power in these types of receivers are usually described using the unit dBm. This is the power delivered to a specified load resistance, nearly always 50 ohms. With that definition, 0 dBm corresponds to 1 mW of power into 50 ohms; that corresponds to a voltage of 0.2236 volts (rms). The power changes by 10 dB for each factor of ten reduction, but is always referenced to the assumed load of 50 ohms.

Radiation Effects in Optical Receivers

The earlier example of transient upset in optocouplers demonstrates the importance of charge collected in the input photodiode in generating transients in optical amplifiers. Optocouplers operate with very high signal-to-noise ratios, but nevertheless are extremely sensitive to upset effects. The large area and extended charge collection depth of the silicon detectors used in those devices are the main factors in their high sensitivity. Receivers that are designed for radiation applications usually use direct-bandgap detectors with reduced charge collection depth in order to reduce the collection volume for radiation-induced charge.

Fig. 66 shows results from a test of a hardened optical receiver operating at a bit rate of 80-Mb/s during irradiation with 59-MeV protons [Facc02]. This receiver used a 1.3 μm laser source with an InGaAs p-i-n detector. The active depth of the detector was approximately 2 μm. The thin active layer reduces the collection volume for transients from the proton beam.

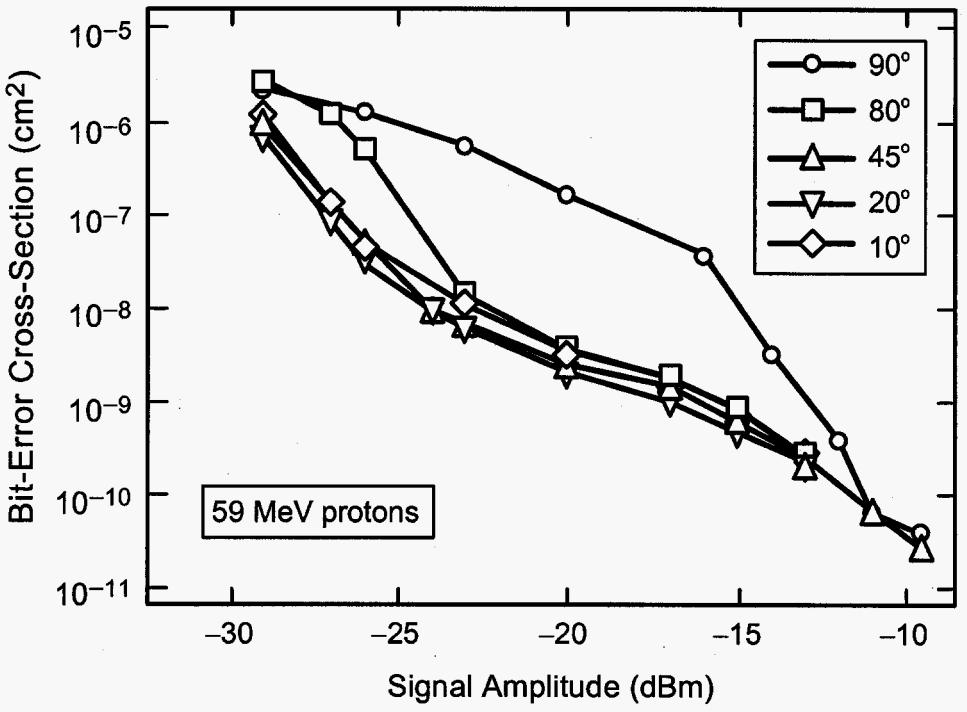

Fig. 66. Bit error cross section for an 80-Mb/s optical receiver irradiated with protons.

The proton beam flux rate was between 1 and 4 x 10^8 protons/(cm^2-s) during these tests, which is considerably higher than typical flux rates in a space environment. This receiver will be used as part of the Large Hadron Collider at CERN. When high optical power levels were used, the bit error rate remained below 10^{-9} even with extreme angles of incidence.

The cross section for bit errors increased to nearly 10^{-5} cm^2 when the input signal was reduce to –30 dBm, the minimum level required for a BER of 10^{-9} when there was no radiation present. Different angles of incidence were used during the tests. For angles of 45 ° and higher the error rate increased sharply with low optical power levels. This was attributed to direct ionization from protons. This is in general agreement with our expectation that receivers are relatively immune to upset from radiation-induced transients as long as the optical power level is well above the minimum level required without the presence of radiation.

This data was used to develop a model for the bit-error rate in the proposed application. The results of the modeling are shown in Fig. 67. They indicate that acceptable performance is expected provided the signal level remains above –25 dBm. This provides significant margin even when considering degradation of components within the receiver from increasing levels of proton irradiation.

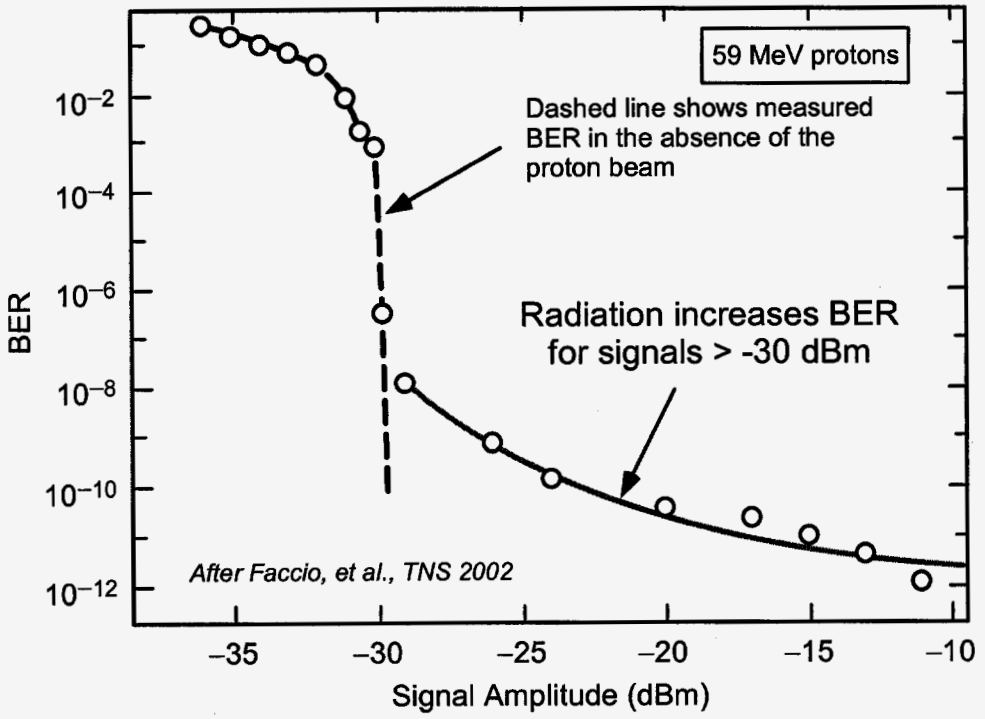

Fig. 67. Predicted error rate for 80-Mb/s receiver.

An additional optical link has developed for applications at the CERN detector that uses a silicon detector and a VCSEL light source operating at 840 nm. Radiation tests have been done on that optical link using 24-GeV protons and pions with energies above 350 GeV [Greg02]. That optical link has acceptable performance in the anticipated environment, even though it uses a detector with much greater charge collection depth.

An optical receiver operating at even higher bit rates was subjected to radiation tests by a different laboratory [Mars94]. That receiver could operate at bit rates up to 1-Gb/s, and also used a wavelength of 1300 nm. The input to the receiver was provided by a laser diode. The receiver used an InGaAs photodiode with a diameter of 80 μm and an active thickness of 3 μm. Radiation tests were done with 63-MeV protons and 18-MeV alpha particles. The optical power was changed during the tests to determine how the error rate depended on input power.

Fig. 68 shows the results of their tests for two specific angles of incidence. The error rate clearly increased when the bit rate was increased, consistent with the basic concept of link margin shown earlier in Fig. 66. When tested with protons, the error cross section decreased by several orders of magnitude when the optical power was increased. This was attributed to direct ionization from protons, which was sufficiently high at low optical power to contribute to the cross section, but not high enough when the optical power was increased. Results at other angles in their paper corroborated that interpretation. When the link was tested with alpha particles, the error cross section changed very little as the optical input power was changed. This flat dependence occurs because alpha particles induce charge by direct ionization, not by nuclear reaction products, and the charge in the detector from 18-MeV alpha particles was well above the threshold condition for the receiver. One would expect that the optical power level would have a larger effect on the cross section even with alpha particles if the LET were lower, near the minimum sensitivity. However, it would not decrease nearly as rapidly as for protons because direct ionization is still the dominant mechanism, unlike protons where indirect reactions also contribute to the cross section.

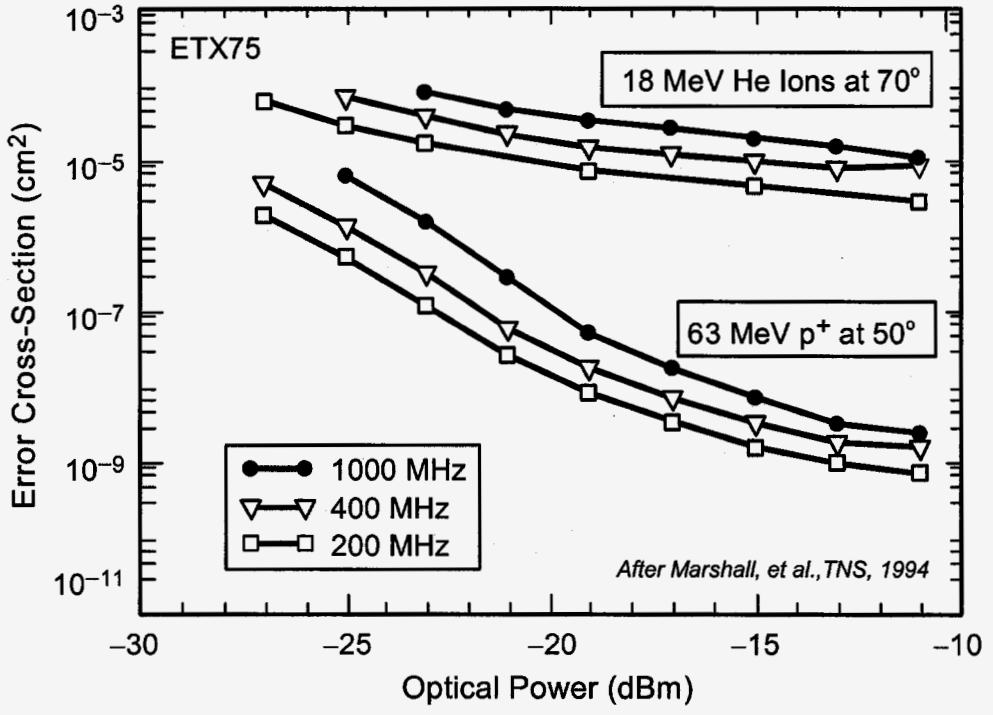

Fig. 68. Error cross section of a high-speed optical data bus operated at various clock rates [Mars94].

It is clear from these examples that errors produced by optical receivers operating at high bit rates are dominated by charge produced by the radiation source in the detector. The bit rate is far lower when the receiver operates with high optical power levels, where the signal during each pulse integration period is well above the minimum required signal level. Degradation of the light source, the detector or the coupling efficiency during extended space missions will reduce the link margin, increasing the error rate. Thus, it is important to make sure that the design considers degradation in link performance in order to maintain satisfactory operation.

Errors may also be caused by upsets in the amplifier, integrator, or other components used in high-performance receivers. In some cases those errors may be more important than single-bit errors from "noise" in the detector because they may persist for many clock cycles, producing strings of errors that may be more difficult to accommodate in system design.

VIII. Summary

This section of the 2004 NSREC Short Course has reviewed the operating principles of photonic sources, optical fibers and optical receivers, emphasizing the underlying physics as well as the physical structure of these devices along with the mechanisms that cause them to respond to radiation. In addition to understanding the operation of these devices, we have to be concerned with two very different effects in space: permanent damage from displacement and ionization damage, and transient effects from heavy ions and energetic protons.

Permanent Damage

In active devices – optical sources and detectors – permanent damage is generally dominated by displacement damage from protons and electrons, requiring tests with these types of particles instead of (or in addition to) cobalt-60 gamma rays. Displacement damage from protons and electrons depends on energy, and that dependence has to be taken into account in performing radiation tests and in interpreting test results for space applications. For III-V devices, there are discrepancies between theoretical and experimental results for proton energies above 50 MeV that can affect the interpretation of test results.

The sensitivity of light-emitting diodes to damage from protons varies over an extremely wide range. The most sensitive LEDs are severely degraded at a fluence of 10^{10} p/cm^2, which is well below the radiation requirement of many earth-orbiting space systems. Those types of devices are used in mainstream optocouplers, causing the optocouplers to degrade very severely at low radiation levels. Other types of LEDs use different fabrication techniques, and can withstand radiation levels that are two to three orders of magnitude higher than amphoterically doped LEDs. When more advanced LEDs are used, degradation in the LEDs is often negligible, and the main system concern then becomes degradation of optical detectors, which are also sensitive to displacement damage.

Optical fibers are affected by ionization damage, not by displacement damage effects, and consequently tests of optical fibers can be done using cobalt-60 gamma rays or pulsed X-rays. Most optical fibers have relatively low loss per unit length, so that radiation-induced absorption in optical fibers is usually important only for fiber lengths > 10 m, or for applications where the fiber is required to function at low temperature.

Transient Effects

We also have to be concerned with transient effects from protons and heavy ions. Most optoelectronic systems are very sensitive to transient effects, and will upset readily from protons (through indirect processes). The optical detector is the key element in these systems. Selecting detectors with small area and thin active regions improves radiation hardness. Thick detectors – such as those used in optocouplers- can be sensitive to direct ionization from protons as well as indirect particles through nuclear reactions, causing the results to depend strongly on particle energy and the incident angle used during testing, and causing high error rates in space applications.

Tests of optical receivers show many of the same characteristics exhibited by transient tests of optocouplers, but are more difficult to interpret. The key point is that the error rate in a radiation environment is directly related to the optical receiver bit rate and the optical power. Receivers that operate with high optical power – which implies high margin between minimum sensitivity and the actual operating point – can be designed that show only slight changes in BER when they are exposed to moderate flux levels, but the designs are more challenging at high bit rate. Tests

done with reduced input power show a large increase in BER compared to tests done with nominal operating power levels. By choosing detectors with small thicknesses it is possible to use optical receivers in the radiation environments that are encountered in many types of spacecraft with relatively small increases in bit error rate. Radiation-tolerant optical receivers have even been designed to withstand the more demanding radiation environment in the Large Hadron Collider detector at CERN.

Future Trends

We have limited this section of the course to older technologies where extensive radiation test results exist, and there is a relatively mature understanding of the mechanisms involved. However, photonic components continue to advance. For example, new designs have been demonstrated that incorporate moveable MEMS-based elements for tunable laser diodes [Vail97]. New applications have been proposed for optical interconnects that use arrays of VSCELs and detector/amplifiers [Olli02] that will use far more compact elements compared to the mainstream components discussed earlier, with reduced operating margins. Hopefully the material presented here will provide sufficient background and understanding to make first-order estimates of potential radiation issues for such technologies as well as providing the background that is needed to understand how radiation affects conventional photonic devices when they are used in spacecraft.

References

[Akbu01] M. Akbulut, *et al.*, "Digital Communications above 1-Gb/s Using 890-nm Surface-Emitting Light-Emitting Diodes," IEEE Phot. Tech. Lett., **13**(1), pp. 85-87 (2001).

[Barr95] A. L Barry, *et al.*, "The Energy Dependence of Lifetime Damage Constants in GaAs LEDs for 1-500 MeV Protons," IEEE Trans. Nucl. Sci., **42**(6), pp. 2104-2107 (1995).

[Bart97] J. L. Barth, Part II of the Short Course presented at the 1997 Nuclear and Space Radiation Effects Conference.

[Bart03] J. L. Barth, C. S. Dyer and E.G. Stassinopoulos, "Space, Atmospheric and Terrestrial Radiation Environments," IEEE Trans. Nucl. Sci., **50**(3), pp. 466-482(2003).

[Beck03] H. N. Becker, T. F. Miyahira and A.H. Johnston, "The Influence of Structural Characteristics on the Response of Silicon Avalanche Photodiodes to Proton Irradiation," accepted for publication in IEEE Trans.Nucl. Sci., **50**(6), pp. 1974-1981 (2003).

[Brai85] M. Brain and T.-P. Lee, "Optical Receivers for Lightwave Communication Systems," IEEE J. Lightwave Tech.., **3**(6), pp. 1281-1300 (1985).

[Choi04] H. W. Choi, C. W. Jeon and M. D. Dawson, "InGaN Micro-ring Light-Emitting Diodes," IEEE Phot. Tech. Lett., **16**(1), pp. 33-35 (2004).

[Choq97] K. D. Choquette and H. Q. Hou, "Vertical-Cavity Surface Emitting Lasers: Moving from Research to Manufacturing," Proc. of the IEEE, **85**(11), pp. 1730-1739 (1997).

[Chua95] S. L. Chuang, Physics of Optoelectronic Devices, Wiley Interscience: New York, 1995.

[Cold95] L. W. Coldren and F. W. Corzine, Diode Lasers and Photonic Integrated Circuits, New York: Wiley, 1995.

[Cole00] J. J. Coleman, "Strained-Layer InGaAs Quantum-Well Heterostructure Lasers," IEEE J. Sel. Topics in Quant. Elect., **6**(6), pp.1008-1013 (2000).

[Comp67] D. M. J. Compton and R. A Cesena, "Mechanisms of Radiation Effects on Lasers," IEEE Trans. Nucl. Sci., **14**(6), pp. 55-61 (1967).

[Devi83] N. Devine and H. B. Garrett, "Charged Particle Distributions in Jupiter's Magnetosphere," J. Geo. Phys. Res., **88**(A9), pp.6889-6903 (1983).

[Diec01] E. Diechsel, *et al.*, "High Power Laser Diodes with Dry-Etched Mirror Facets and Integrated Monitor Photodiodes," IEEE J. on Selected Topics in Quant. Elect., **7**(2), pp.106-110 (2001).

[Dodd03] P. E. Dodd and L. W. Massengill, "Basic Mechanisms and Modeling of Single-Event Upset in Digital Microelectronics," IEEE Trans. Nucl. Sci., **50**(3), pp. 583-602 (2003).

[Evan93] B. D. Evans, H. E. Hager and B. W. Hughlock, "5.5 MeV Proton Irradiation of a Strained Quantum Well Laser Diode and a Multiple Quantum-Well Broadband LED," IEEE Trans. Nucl. Sci. **40**(6), pp. 1645-1654 (1993).

[Facc01] F. Faccio, *et al.*, "Single-Event Upset Tests of an 80-Mb/s Optical Receiver," IEEE Trans. Nucl. Sci., **48**(5), pp. 1700-1707 (2001).

[Fehs02] R. Fehs, *et al.*, "A Quantitative Study of Radiative, Auger, and Defect Related Recombination Processes in 1.3-μm GaInNAs-Based Quantum-Well Lasers," IEEE J. Sel. Top. In Quant. Elect., **8**(4), pp. 801-810 (2002).

[Frieb88] E. J. Friebele, *et al.*, "Interlaboratory Comparison of Radiation-Induced Attenuation in Optical Fibers. Part I: Steady-State Exposures," IEEE J. Lightwave Tech., **6**(2), pp. 165-171 (1988).

[Germ02] R. Germanicus, *et al.*, "Analysis of the Proton-Induced Permanent Degradation in an Optocoupler," IEEE Trans. Nucl. Sci. **49**(3), pp. 1421-1425 (2002).

[Gilb82] R. M. Gilbert, "Photobleaching of Radiation-Induced Color Centers in a Germania-Doped Fiber," IEEE Trans. Nucl. Sci., **29**(6), pp.1484-1488 (1982).

[Gill00] K. Gill, *et al.*, "Radiation Damage and Annealing in 1310 nm InGaAsP/InP Lasers," 2000 IEEE Radiation Effects Data Workshop, pp.153-157.

[Gira03] S. Girard, *et al.*, "Pulsed X-Ray and γ-Ray Irradiation Effects on Polarization-Maintaining Optical Fibers," presented at the 2003 RADECS Conference, Noordwijk, The Netherlands, Sept. 15-19, 2003.

[Grig03] I.-M. Grigor, "Radiation-Tolerant Optical Links for the ATLAS Inner Detector," IEEE Trans. Nucl. Sci., **49**(3), pp. 1114-1116 (2003).

[Iga00] K. Iga, "Surface-Emitting Laser – Its Birth and Generation of New Optoelectronics Field," IEEE J. Selected Topics in Quant. Elect., **6**(6), pp. 1201-1215 (2000).

[John98] A. H. Johnston, *et al.*, "Single-Event Upset in Optocouplers," IEEE Trans. Nucl. Sci., **45**(6), pp. 2867-2875 (1998).

[John99] A. H. Johnston, *et al.*, "Angular and Energy Dependence of Proton Upset in Optocouplers," IEEE Trans. Nucl. Sci., **46**(6), pp. 1660-1665 (1999).

[John00] A. H. Johnston and T. F.Miyahira, "Characterization of Proton Damage in Light-Emitting Diodes," ," IEEE Trans. Nucl. Sci., **47**(6), pp. 2500-2507 (2000).

[John01] A. H. Johnston, T. F. Miyahira and B. G. Rax, "Proton Damage in Advanced Laser Diodes," IEEE Trans. Nucl. Sci., **48**(6), pp. 1764-1772 (2001).

[John02] A. H.. Johnston and T.F. Miyahira, "Energy Dependence of Proton Damage in Optical Emitters," IEEE Trans. Nucl. Sci., **49**(6), pp. 1426-1431 (2002).

[John03] A. H. Johnston, "Radiation Effects in Light-Emitting and Laser Diodes," IEEE Trans. Nucl. Sci., **50**(3), pp. 689-703 (2003).

[LaBe97] K. LaBel, *et al.*, "Proton-Induced Transients in Optocouplers: In-Flight Anomalies, Ground Irradiation Tests, Mitigation and Implications," IEEE Trans. Nucl. Sci., **44**(6), pp. 1895-1902 (1997).

[Lede00] N. N. Ledenstov, *et al.*, "Quantum-Dot Heterostructure Lasers," IEEE J. Sel. Topics in Quant. Elect., **6**(3), pp. 439-451 (2000).

[Liu92] Y. Liu, *et al.*, "A Planar InP/InGaAs Avalanche Photodiode with Floating Guard Ring and Double Diffused Junction," IEEE J. Lightwave Tech., **10**(2), pp.182-193(1992).

[Loo81] R. Loo, R. C. Knechtli and G. S. Kamath, "Enhanced Annealing of GaAs Solar Cell Damage," in Proc. of the 15th IEEE Photovoltaic Specialties Conference, vol. 33, 1981.

[Mars94] P. W. Marshall, C. J. Dale, M. A. Carts and K. A. LaBel, "Particle-Induced Bit Errors in High Performance Fiber Optic Data Links for Satellite Management," IEEE Trans. Nucl. Sci., **41**(6), pp. 1958-1965(1994).

[Mazu02] J. Mazur, Part II of the Short Course presented at the 2002 Nuclear and Space Radiation Effects Conference.

[Miya02] T. F. Miyahira and A. H. Johnston, "Trends in Optocoupler Radiation Degradation," IEEE Trans. Nucl. Sci., **49**(6), pp. 3009-3015 (2002).

[Naka91] K. Nakagawa and K. Iwashita, "High-Speed Optical Transmission Systems Using Advanced Monolithic IC Technologies," IEEE J. on Sel. Areas in Communications, **6**(5), pp. 683-688 (1991).

[Olli02] E. Ollier, "Optical MEMS Devices Based on Moving Waveguides," IEEE J. Sel. Topics in Quant. Elect., **8**(1), pp.155-162 (2002).

[Pani76] M. B. Panish, "Heterostructure Injection Lasers," Proc. of the IEEE, **64**(10), pp. 1512-1540 (1976).

[Park00] G. Park, *et al.*, "Low-Threshold Oxide-Confined 1.3-μm Quantum-Dot Laser," Phot. Tech. Lett., **13**(3), pp. 230-232 (2000).

[Pank76] J. I. Pankove, Optical Processes in Semiconductors, Prentice-Hall, Englewood Cliffs, NJ and Dover, New York (1976)

[Rax96] B. G. Rax, *et al.*, "Total Dose Effects and Hardness Assurance for Optocouplers," IEEE Trans. Nucl. Sci., **43**(6), pp. 3145-3150 (1996).

[Raze00] M. Razeghi, "Optoelectronic Devices Based on III-V Compound Semiconductors Which Have Made a Major Scientific and Technological Impact in the Past 20 Years," IEEE J. on Selected Topics in Quant. Elect., **6**(6), pp. 1344-1354 (2000).

[Ree00] R. A. Reed, *et al.*, "Energy Dependence of Proton Damage in AlGaAs Light-Emitting Diodes," IEEE Trans. Nucl. Sci., **47**(6), pp. 2492-2499 (2000).

[Rose82] B. H. Rose and C. E. Barnes, "Proton Damage Effects on Light Emitting Diodes," J. Appl. Phys., **53**(3), pp. 1772-1780 (1982).

[Rose95] T. S. Rose, M. S. Hopkins and R. A. Fields, "Characterization and Control of Gamma and Proton Radiation Effects on the Performance of Nd:YAG and Nd:YLF Lasers," IEEE J. Quant. Elect., **31**(9), pp. 1593-1602 (1995).

[Rupp66] H. Rupprecht, *et al.*, Appl. Phys. Lett., **9**, pp. 221 (1966).

[Schö97] H. Schöne, *et al.*, "AlGaAs Vertical-Cavity Surface-Emitting Laser Responses to 4.5-MeV Proton Irradiation," IEEE Phot. Tech. Lett., **9**(12), pp. 1552-1554, 1997.

[Selm01] S. R. Selmic, *et al.*, "Design and Characterization of AlGaInAs-InP Multiple-Quantum-Well Lasers," IEEE J. on Selected Topics in Quant. Elect., **7**(2), pp. 340-349 (2001).

[Sext03] F. W. Sexton, "Destructive Single-Event Effects in Semiconductor Devices and IC's," IEEE Trans. Nucl. Sci., **50**(3), pp. 603-621 (2003).

[Srou88] J. R. Srour and J.M. McGarrity, "Radiation Effects on Microelectronics in Space," Proc. IEEE, **76**, pp. 1433-1469, Nov. 1988.

[Sou03] J. R. Srour, C. J. Marshall and P. W. Marshall, "Review of Displacement Damage Effects in Silicon Devices," IEEE Trans. Nucl. Sci., **50**(3), pp. 653-670 (2003).

[Summ87] G. P. Summers, *et al.*, "Correlation of Particle-Induced Displacement Damage in Silicon," IEEE Trans. Nucl. Sci., **34**(6). pp. 1134-1141 (1987).

[Summ93] G. P. Summers, *et al.*, "Damage Correlations in Semiconductors Exposed to Gamma, Electron and Proton Irradiation," IEEE Trans. Nucl. Sci., **40**(6). pp. 1372-1379 (1993).

[Swan87] E. A. Swanson, E. R. Arnau and F. D.Walther, "Measurements of Natural Radiation Effects in a Low-Noise Avalanche Photodiode," IEEE Trans. Nucl. Sci., **34**(6), pp. 1658-1661 (1987).

[Sun03] D. Sun, *et al.*, "Sub-mA Threshold 1.5 μm VCSELs with Epitaxial and Dielectric DBR Mirrors," Phot. Tech. Lett., **15**(12), pp.1677-1679 (2003).

[Sige81] G. H. Sigel, *et al.*, "An Analysis of Photobleaching Techniques for the Radiation Hardening of Fiber Optic Links," IEEE Tran. Nucl. Sci., **28**(6), pp. 4095-4101 (1981).

[Swif03] G. M. Swift, *et al.*, "Annealing Displacement Damage in GaAs: Another Galilio Success Story," IEEE Trans. Nucl. Sci., **50**(6), pp. 1991-1997 (2003).

[Tay901] E. W. Taylor, *et al.*, "Interlaboratory Comparison of Radiation-Induced Attenuation in Optical Fibers. Part II: Steady-State Exposures," IEEE J. Lightwave Tech., **8**(6), pp. 967-976, 1990.

[Tay902] E. W. Taylor, *et al.*, "Interlaboratory Comparison of Radiation-Induced Attenuation in Optical Fibers. Part III: Transient Exposures," IEEE J. Lightwave Tech., **8**(6), pp. 977-989, 1990.

[Vail97] E. C. Vail, *et al.*, "High Performance and Novel Effects of Micromechanical Tunable Vertical-Cavity Lasers," IEEE Select. Topics Quantum Electron., **3**(2), pp. 691-697 (1997).

[Vurg97] I. Vurgaftman and J. R. Meyer, "Effects of Bandgap, Lifetime, and Other Nonuniformities on Diode Laser Thresholds and Slope Efficiencies," IEEE J. Sel. Top.in Quant. Elect., **3**(2), pp. 475-484 (1997).

[Walt01] R. J. Walters, *et al.*, "Correlation of Proton Radiation Damage in InGaAs-GaAs Quantum-Well Light-Emitting Diodes," IEEE Trans. Nucl. Sci., **48**(6), pp. 1773-1775 (2001).

[Weat03] T. R. Weatherford and W. T. Anderson, Jr., "Historical Perspective on III-V Devices," IEEE Trans. Nucl. Sci., **50**(3), pp. 704-710 (2003).

[West88] R H. West, "A Local View of Radiation Effects in Fiber Optics," IEEE J. Lightwave Tech., **6**(2), pp. 155-164 (1988).

[Witt96] V. Wittpahl, *et al.*, "A Degradation Model for the Light Output of LEDs Based on Cathodoluminescence Signals and Junction Ideality Factor," Proc. 1996 International. Reliability Physics Conf., pp.188-194.

[Vand97] D. A. Vanderwater, *et al.*, "High-Brightness AlGaInP Light Emitting Diodes," Proc. IEEE, **85**(11), pp. 1752-1764 (1997).